

Oil & Natural Gas Technology

DOE Award No.: DE-FC26-03NT15466

Final Report (April 17, 2003 - October 16, 2008)

Modeling the Transport and Chemical Evolution of Onshore and Offshore Emissions and Their Impact on Local and Regional Air Quality Using a Variable-Grid-Resolution Air Quality Model

Submitted by:

Adel Hanna (Principal Investigator)
Institute for the Environment
University of North Carolina at Chapel Hill
Bank of America Plaza, CB# 6116
137 E. Franklin Street
Chapel Hill, NC 27599-6116

Prepared for:

United States Department of Energy
National Energy Technology Laboratory

January 14, 2009



Office of Fossil Energy



Disclaimer

This report was prepared as an account of work sponsored by an agency of the United States Government. Neither the United States Government nor any agency thereof, nor any of their employees, makes any warranty, express or implied, or assumes any legal liability or responsibility for the accuracy, completeness, or usefulness of any information, apparatus, product, or process disclosed, or represents that its use would not infringe privately owned rights. Reference herein to any specific commercial product, process, or service by trade name, trademark, manufacturer, or otherwise does not necessarily constitute or imply its endorsement, recommendation, or favoring by the United States Government or any agency thereof. The views and opinions of authors expressed herein do not necessarily state or reflect those of the United States Government or any agency thereof.

Abstract

The overall objective of this research project was to develop an innovative modeling technique to adequately model the offshore/onshore transport of pollutants. The variable-grid modeling approach that was developed alleviates many of the shortcomings of the traditionally used nested regular-grid modeling approach, in particular related to biases near boundaries and the excessive computational requirements when using nested grids. The Gulf of Mexico region contiguous to the Houston-Galveston area and southern Louisiana was chosen as a test bed for the variable-grid modeling approach. In addition to the onshore high pollution emissions from various sources in those areas, emissions from on-shore and off-shore oil and gas exploration and production are additional sources of air pollution. We identified case studies for which to perform meteorological and air quality model simulations. Our approach included developing and evaluating the meteorological, emissions, and chemistry-transport modeling components for the variable-grid applications, with special focus on the geographic areas where the finest grid resolution was used. We evaluated the performance of two atmospheric boundary layer (ABL) schemes, and identified the best-performing scheme for simulating mesoscale circulations for different grid resolutions. Use of a newly developed surface data assimilation scheme resulted in improved meteorological model simulations. We also successfully ingested satellite-derived sea surface temperatures (SSTs) into the meteorological model simulations, leading to further improvements in simulated wind, temperature, and moisture fields. These improved meteorological fields were important for variable-grid simulations, especially related to capturing the land-sea breeze circulations that are critical for modeling offshore/onshore transport of pollutants in the Gulf region. We developed SMOKE-VGR, the variable-grid version of the SMOKE emissions processing model, and tested and evaluated this new system. We completed the development of our variable-grid-resolution air quality model (MAQSIP-VGR) and performed various diagnostic tests related to an enhanced cloud parameterization scheme. We also developed an important tool for variable-grid graphics using Google Earth. We ran the MAQSIP-VGR for the Houston-Galveston and southern Louisiana domains for an August 23 to September 2, 2002, episode.

Results of the modeling simulations highlighted the usefulness of the variable-grid modeling approach when simulating complex terrain processes related to land and sea close to an urban area. Our results showed that realistic SST patterns based on remote sensing are critical to capturing the land-sea breeze, in particular the inland intrusion of the reversed mesoscale circulation that is critical for simulating air pollution over urban areas near coastal regions. Besides capturing the correct horizontal gradient between land and sea surface temperatures, it is important to use an adequate ABL scheme in order to quantify correctly the vertical profiles of various parameters. The ABL scheme should capture the dynamics of the marine boundary layer, which is not often considered in a typical simulation over land. Our results further showed the effect of using satellite-derived SSTs on the horizontal and vertical extent of the modeled pollution pattern, and the increase in hourly ozone concentrations associated with changes in ABL characteristics resulting from the enhanced mesoscale circulation in the lower troposphere.

Contents

Disclaimer	ii
Abstract.....	iii
Figures.....	v
1. Project Objectives	1
2. Approach, Results, and Discussion.....	1
2.1 Task 1: Develop Modeling Domains and Case Studies.....	2
2.2 Task 2: Improve the Representation of Boundary Layer Processes	3
2.3 Task 3: Assimilate Surface Observations to Improve MM5 Simulations	16
2.3.1. Assimilation of Land-based Surface Observations using the FASDAS	16
2.3.2 Ingestion of Satellite-Measured Sea Surface Temperatures into the MM5	28
2.4 Task 6: Enhance Representation of Cloud Processes in the MAQSIP-VGR	44
2.5 Task 4: Simulate Mesoscale Circulations Using the MM5	47
2.6 Task 5: Develop Emission Estimates.....	49
2.7 Tasks 7and 8: Perform Simulations and Evaluation of the MAQSIP-VGR over the Houston-Galveston Domain and Northeast Gulf (southern Louisiana Gulf) Domain.....	51
2.8 Additional Tasks	55
3. Conclusions.....	55
3.1 Summary of Results.....	55
3.2 Innovative Features of the Research Program	56
4. Publications	57
References.....	58

Figures

Figure 1. Simulation domains selected for the MM5 simulations. Domains D01 and D02 used 36- and 12-km grids, respectively, while domains D03 and D04 used 4-km grids located over the Houston-Galveston region and over southern Louisiana.	3
Figure 2a. Vertical variation of observed and simulated temperature and dew point temperature soundings for North Platte, NB, at 0000 UTC on August 26, 2000.	5
Figure 2b. Vertical variation of observed and simulated temperature and dew point temperature soundings for Lake Charles, LA, at 1200 UTC on August 26, 2000.	5
Figure 2c. Vertical variation of observed and simulated temperature and dew point temperature soundings for Greensboro, NC, at 0000 UTC on August 26, 2000.	6
Figure 2d. Vertical variation of observed and simulated temperature and dew point temperature soundings for Greensboro, NC, at 1200 UTC on August 26, 2000.	6
Figure 3. MM5 simulated horizontal wind vectors at 2100 UTC August 24, 2000, from (a) “Mrf” and (b) “Eta” simulations using the 36-km grids.	7
Figure 4. Accumulated precipitation (inches) for a period of 24 h ending at 1200 UTC 24 August 2000 from the (a) CPC analysis, (b) “Mrf”, and (c) “Eta” cases.	9
Figure 5. Accumulated precipitation (inches) for a period of 24 h ending at 1200 UTC 28 August 2000 from the (a) CPC analysis, (b) “Mrf”, and (c) “Eta” cases.	10
Figure 6a. Temporal variation of near-surface air temperature averaged over all of the measurements and corresponding modeled values, starting at 1200 UTC 23 August 2000 for the “Mrf” and “Eta” cases for 4-km grids.	11
Figure 6b. Temporal variation of bias in the averaged near-surface air temperature for the “Mrf” and “Eta” cases, starting at 1200 UTC 23 August 2000.	11
Figure 7a. Temporal variation of bias in the averaged near-surface water vapor mixing ratio for the “Mrf” and “Eta” cases, starting at 1200 UTC 23 August 2000.	12
Figure 7b. Temporal variation of root mean square error in the averaged near-surface water vapor mixing ratio for the “Mrf” and “Eta” cases, starting at 1200 UTC 23 August 2000.	12
Figure 8a. Temporal variation of root mean square errors in the averaged near-surface horizontal wind speed for the “Mrf” and “Eta” cases, starting at 1200 UTC 23 August 2000.	13
Figure 8b. Temporal variation of root mean square errors in the averaged near-surface horizontal wind direction for the “Mrf” and “Eta” cases, starting at 1200 UTC 23 August 2000.	13
Figure 9. Accumulated precipitation for the (a) “Obs”, (b) “Mrf” and (c) “Eta” cases, ending at 1200 UTC 24 August 2000.	14

Figure 10. Accumulated precipitation for the “Obs”, “Mrf” and “Eta” cases, ending at 1200 UTC 28 August 2000.....	15
Figure 11. Temporal variability in the number of available surface observations used in developing statistical indices for the domain using 36-km grid resolution. Zero on the x-axis corresponds to 1200 UTC 23 August 2000.....	17
Figure 12. Temporal variation of near-surface air temperature averaged over all of the measurements and corresponding modeled values, starting at 1200 UTC 23 August 2000 for the domain D01 using the 36-km grid resolution.....	18
Figure 13. Temporal variation of bias in the averaged near-surface air temperature for the “Base” and “Fasdas” cases, starting at 1200 UTC 23 August 2000 (for 36-km grid resolution).	18
Figure 14. Temporal variation of bias in the averaged near-surface water vapor mixing ratio for the “Base” and “Fasdas” cases, starting at 1200 UTC 23 August 2000.....	19
Figure 15. Vertical variation in temperature and dew point temperature from observations and the “Base” and “Fasdas” cases at 0000 UTC 28 August 2000 for Del Rio, TX.....	20
Figure 16. Vertical variation in temperature and dew point temperature from observations and the “Base” and “Fasdas” cases at 0000 UTC 24 August 2000 for Pittsburgh, PA.	20
Figure 17. Vertical variation in temperature and dew point temperature from observations and the “Base” and “Fasdas” cases at 0000 UTC 25 August 2000 for Lake Charles, LA.	21
Figure 18. Vertical variation in temperature and dew point temperature from observations and the “Base” and “Fasdas” cases at 0000 UTC 26 August 2000 for North Platte, NB.....	21
Figure 19. Accumulated precipitation (inches) for a period of 24 h ending at 1200 UTC 24 August 2000 from the (a) CPC analysis, (b) “Base”, and (c) “Fasdas” cases.	23
Figure 20. Accumulated precipitation (inches) for a period of 24 h ending at 1200 UTC 28 August 2000 from the (a) CPC analysis, (b) “Base”, and (c) “Fasdas” cases.	24
Figure 21a. Temporal variation of near-surface air temperature averaged over all of the measurements and corresponding modeled values, starting at 1200 UTC 23 August 2000 for the “Base” and “Fasdas” cases for 4-km grids.....	25
Figure 21b. Temporal variation of near-surface air temperature RMSEs for the “Base” and “Fasdas” cases using 4-km grids starting at 1200 UTC 23 August 2000	25
Figure 22a. Temporal variation of averaged near-surface water vapor mixing ratio for the “Base” and “Fasdas” cases, starting at 1200 UTC 23 August 2000.	26
Figure 22b. Temporal variation of near-surface water vapor mixing ratio RMSEs for the “Base” and “Fasdas” cases using 4-km grids starting at 1200 UTC 23 August 2000	26
Figure 23a. Temporal variation of near-surface horizontal wind speed RMSEs for the “Base” and “Fasdas” cases using 4-km grids starting at 1200 UTC 23 August 2000	27
Figure 23b. Temporal variation of near-surface horizontal wind direction RMSEs for the “Base” and “Fasdas” cases using 4-km grids starting at 1200 UTC 23 August 2000	27
Figure 24a. Accumulated precipitation for the “Obs”, “Base” and “Fasdas” cases, ending at 1200 UTC 24 August 2000 for the 4-km grids.	29

Figure 24b. Accumulated precipitation for the “Obs”, “Base” and “Fasdas” cases, ending at 1200 UTC 28 August 2000 for the 4-km grids.....	30
Figure 25. Spatial distribution of sea surface temperatures in domain D03 obtained from (a) the traditional NCEP analysis and (b) NOAA’s satellite-derived measurements, at 1200 UTC 23 August 2000. Note the difference in the scale ranges.....	32
Figure 26. Portion of Gulf of Mexico considered (highlighted grid cells) in developing area-averaged meteorological parameters for analysis and intercomparison.	33
Figure 27. Area-averaged (a) surface latent heat fluxes and (b) depth of the ABL, over the Figure 26 subregion of the Gulf of Mexico. Black: “Base”; Red: “Sat”	34
Figure 28a. Radar imagery of reflectivity showing intensity of precipitation at 2100 UTC 24 August 2000, obtained from a study by Neilsen-Gammon (2002).....	35
Figures 28b, 28c. Modeled shortwave radiation reaching the surface (W/m^2) at 2100 UTC 24 August 2000 for the (b) “Base” and (c) “Sat” cases.	36
Figures 29. Modeled total precipitation (cm/h) for an hour ending at 2100 UTC 24 August 2000 for the (a) “Base” and (b) “Sat” cases.....	37
Figure 30. Horizontal distribution of water vapor mixing ratio (kg/kg) and its vector fluxes (m/s kg/kg) at 0100 UTC 25 August 2000 for the (a) “Base” and (b) “Sat” cases.....	38
Figure 31a. Temporal variation of near-surface air temperature averaged over all of the measurements and corresponding modeled values, starting at 1200 UTC 23 August 2000 for the “Base” and “Sat” cases for the 4-km grids.....	39
Figure 31b. Temporal variation of near-surface air temperature RMSEs for the “Base” and “Sat” cases using the 4-km grids starting at 1200 UTC 23 August 2000	39
Figure 32a. Temporal variation of averaged near-surface water vapor mixing ratio for the “Base” and “Base” cases, starting at 1200 UTC 23 August 2000.	40
Figure 32b. Temporal variation of near-surface air mixing ratio RMSEs for the “Base” and “Sat” cases using the 4-km grids starting at 1200 UTC 23 August 2000.	40
Figure 33. Vertical variation of Temperature, dew point temperature, and horizontal wind vectors for “Obs”, “Base”, and “Sat” at (a) 0000 UTC and (b) 1200 UTC 26 August 2000 for a coastal location in southwest Louisiana.	41
Figure 34a. Accumulated precipitation for the “Obs”, “Base” and “Sat” cases, ending at 1200 UTC 24 August 2000 for the 4-km grids.....	42
Figure 34b. Accumulated precipitation for the “Obs”, “Base” and “Sat” cases, ending at 1200 UTC 28 August 2000 for the 4-km grids.....	43
Figure 35. Example results from testing the 1-D cloud module for a case in which an initially specified concentration profile was subjected to cloud mixing. (a) Variation in O_3 vertical profiles at different times during the simulation; (b) change in column total O_3 mass relative to the initial mass.	46
Figure 36. The modeling domain for the August 2000 episode simulations (a) the 36-km grid resolution and (b) variable grid resolution overlaying the 36-km grid resolution; the Houston-Galveston 4-km domain is at the core of the blue shades.....	47
Figure 37. Flow diagram of the variable-grid modeling components.	48

Figure 38. Variable grid surface air temperature simulated by the MM5 model for August 24, 2000 at 0000 EDT	49
Figure 39. Emissions of point-source NO: (a) SMOKE-VGR one-hour variable-grid emissions; and (b) SMOKE 24-hour emissions (regular 36-km grid resolution)).....	53
Figure 40. SMOKE-VGR one-hour variable-grid point source emissions for (a) CO and (b) primary sulfate	53
Figure 41. CO emissions (mol/yr) during 23 August 2000, for (a) the full domain and (b) the zoomed-in Houston area domain. Google Earth was used to create the variable-grid mesh on the domain.	54
Figure 42. PM-coarse emissions during 23 August 2000, for full domain with (a) zoomed-in Houston-Galveston area domain and (b) zoomed in southern Louisiana domain.....	54

1. Project Objectives

This research project had two primary objectives:

- (1) To further develop and refine the Multiscale Air Quality Simulation Platform – Variable Grid Resolution (MAQSIP-VGR) model, an advanced variable-grid-resolution air quality model, to provide detailed, accurate representation of the dynamical and chemical processes governing the fate of anthropogenic emissions in coastal environments.
- (2) To improve current understanding of the potential impact of on-shore and off-shore oil and gas exploration and production (E&P) emissions on ozone (O₃) and particulate matter (PM) nonattainment in the Gulf of Mexico and surrounding states.

2. Approach, Results, and Discussion

The following eight tasks were proposed to reach the goals and objectives of this project (above). In this section we provide details of the research approach and the analysis conducted under the following eight tasks:

- Task 1: Develop Modeling Domains and Case Studies
- Task 2: Improve the Representation of Boundary Layer Processes
- Task 3: Assimilate Surface Observations to Improve Mesoscale Model Version 5 (MM5) Simulations
 - Land-Use Observations
 - Satellite-Based Observations
- Task 4: Simulate Mesoscale Circulations Using the MM5
- Task 5: Develop Emission Estimates
- Task 6: Enhance Representation of Cloud Processes in the MAQSIP-VGR
- Task 7: Perform Simulations and Evaluation of the MAQSIP-VGR over the Houston-Galveston Domain
- Task 8: Perform Simulations and Evaluation of the MAQSIP-VGR over the Northeast Gulf (southern Louisiana Gulf) Domain

In addition to the above tasks, we added a technology transfer component to the project to enable broader use of the approach in community air quality models such as the U.S. Environmental Protection Agency (EPA) Community Multiscale Air Quality (CMAQ) model.

Tasks 2, 3, and 4 address the meteorological developments and analyses (using the MM5), while Tasks 6, 7, and 8 focus on case study analyses of the variable-grid meteorological inputs (using the MM5), the emissions inputs (using the Sparse Matrix Operator Kernel Emissions [SMOKE] system), and pollutant species simulations (using the MAQSIP-VGR). MAQSIP-VGR is based on the Multiscale Air Quality Simulation Platform (MAQSIP) model (Mathur et al., 2005)

Section 3 of this report presents conclusions derived from this project, and Section 4 gives a list of conference/workshop presentations and journal articles that were completed during the course of the project.

2.1 Task 1: Develop Modeling Domains and Case Studies

As a starting point for our research, we developed four domains for use in performing numerical simulations with a meteorological model, the Mesoscale Model Version 5 (MM5) (Grell et al., 1994), to generate meteorological inputs to the MAQSIP-VGR. These meteorological modeling domains (Figure 1) were configured with different regular-grid horizontal resolutions: 36, 12, and 4 km. The 36-km-resolution grid (domain D01) covered a region extending westward from the Atlantic Ocean to the Rockies; a grid at this coarse resolution allowed meteorological modeling simulations that were computationally inexpensive, and whose results could be used primarily to provide lateral boundary conditions to the nested grids. The 12-km grid (domain D02) covered portions of southern and southeastern states.

The 4-km grids (domains D03 and D04) covered domains that were chosen for performing air quality modeling studies intended to address air pollution issues of interest to this project. To specifically study the effects of onshore and offshore emissions on the coastal environments, we developed these two 4-km-resolution domains, one over the Houston-Galveston region and the other over southern Louisiana. Those modeling domains were basically used to test and examine the modeling processes (as described in Tasks 2, 3, and 6) in order to develop a modeling system adequate for the variable-grid applications that were needed to study offshore and onshore pollutant transport.

Selection of the time periods simulated for the case studies was based on analysis of measurement data and the availability of offshore emissions activity data. We also considered other current and prior modeling efforts (e.g., the Gulf Coast ozone study), with the intent of simulating similar time periods to allow us to cross-compare and evaluate our modeling results against others available for the region. The time period we selected for our numerical simulation case study over the Houston-Galveston and southern Louisiana regions was August 23 to September 2, 2000. These dates were chosen because a severe air pollution episode occurred over the region at that time. MAQSIP-VGR simulations were performed to study the effects of various onshore and offshore emissions on the air quality of the coastal environments (Tasks 7 and 8). We used 28 vertical layers to represent atmospheric processes in the vertical, consistent with the literature (e.g., Neilson-Gammon [2002]).

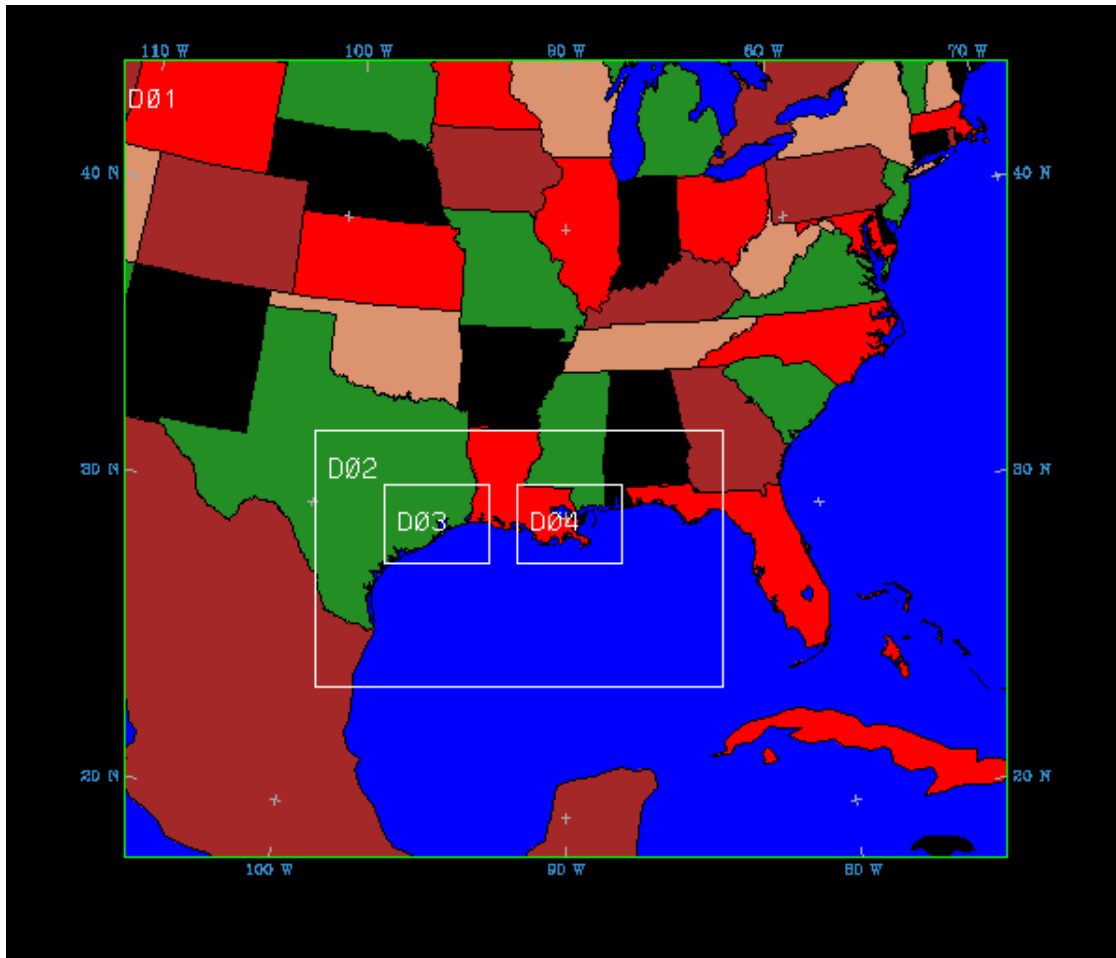


Figure 1. Simulation domains selected for the MM5 simulations. Domains D01 and D02 used 36- and 12-km grids, respectively, while domains D03 and D04 used 4-km grids located over the Houston-Galveston region and over southern Louisiana.

2.2 Task 2: Improve the Representation of Boundary Layer Processes

Emissions of oxides of nitrogen (NO_x), volatile organic compounds (VOC,) and sulfur dioxide (SO_2) from point and other (ships, helicopters) sources released over the Outer Continental Shelf regions can be transported by land and sea breezes, leading to increased pollutant concentrations in coastal and inland regions surrounding the Gulf of Mexico. Because marine boundary layer processes are controlled mostly by weak forcing mainly due to shear production and in part by weak buoyancy production of turbulence, it is critical to study the benefits of using a turbulent kinetic energy-based scheme (TKE scheme) in the MM5 compared to a traditional eddy-diffusivity-based first-order atmospheric boundary layer (ABL) scheme. We performed MM5 simulations using a TKE-based scheme and an eddy-diffusivity-based scheme and evaluated them rigorously regarding their ability to realistically simulate marine and coastal circulations.

Although land-sea breeze processes may not be well resolved at the 36-km grid resolution, it is necessary to perform coarse-resolution MM5 simulations to provide lateral boundary conditions to the nested-grid domains delineated in Task 1. At this resolution, we evaluated MM5 simulations that used either an eddy-diffusivity-based ABL scheme or a TKE-based ABL scheme. Results obtained from using the eddy-diffusivity-based scheme are referred to below as “Mrf”; those from using the TKE scheme are “Eta.”

We analyzed various statistical measures (e.g., root mean square error [RMSE], bias) for several important surface meteorological parameters that were simulated by the MM5, because of their potential influence on the results from the air quality simulations. We also completed analysis of upper-air soundings simulated by the MM5. Figures 2a through 2d show the observed temperature and dew point temperature soundings (referred to as “Obs”) and the modeled soundings obtained from the “Mrf” and “Eta” cases, for three sites on August 26, 2000; these plots are about three days into the simulations. For the North Platte, Nebraska, site at 0000 UTC (Fig. 2a), the “Mrf” simulations show cooler temperature profiles (~1-3 K) than both the observations and the “Eta” simulations. For Lake Charles, Louisiana, at 1200 UTC (Fig. 2b), modeling errors are very small with both “Mrf” and “Eta” and are comparable to each other. For Greensboro, North Carolina, at 0000 (Fig. 2c) and 1200 UTC (Fig. 2d), there are negligible (~±0.5 K) errors in the simulated temperatures for “Mrf” and “Eta” when compared to observed soundings. Analysis of several other soundings at various observational times revealed that at 0000 UTC the “Eta” simulations were slightly better than the “Mrf” ones, while at 1200 UTC the “Mrf” and “Eta” temperature simulations were similar. For water vapor mixing ratio, “Eta” simulations seemed to be slightly higher than the measurements (~1 g/kg), while “Mrf” simulations showed slightly lower values (~-0.5 g/kg) than the observations (figures not shown). Wind profiles show some large errors in the directional component for the coastal regions (e.g., Fig. 2b) in both the “Mrf” and “Eta” simulations, particularly in the ABL, while aloft wind speed and direction are very close to the observations for both “Mrf” and “Eta”. As an example, we show the horizontal wind vectors simulated by the “Mrf” and “Eta” (Figs. 3a and 3b), which reveal differences in the wind direction and speed over the coastal regions of the Gulf of Mexico.

Legends for Figures 2a through 2d:

Legend for Plotted Lines

	Obs T		Obs T _d
	Eta T		Eta T _d
	Mrf T		Mrf T _d

Legend for Wind Barbs

Yellow – “Obs”
Green – “Mrf”
Magenta – “Eta”

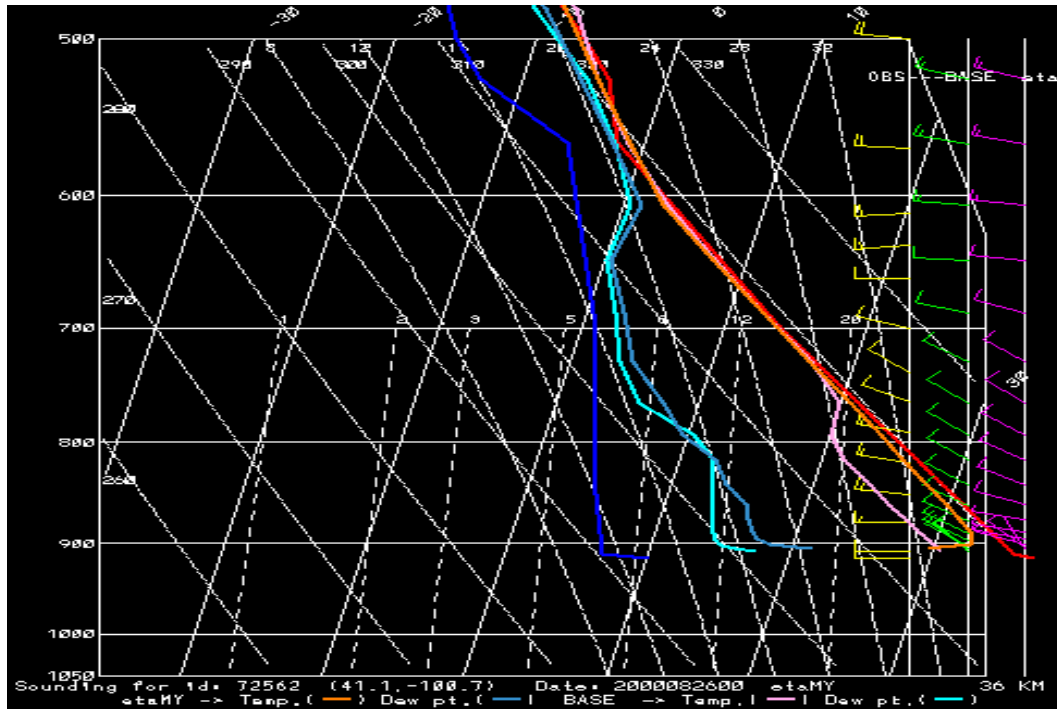


Figure 2a. Vertical variation of observed and simulated temperature and dew point temperature soundings for North Platte, NB, at 0000 UTC on August 26, 2000.

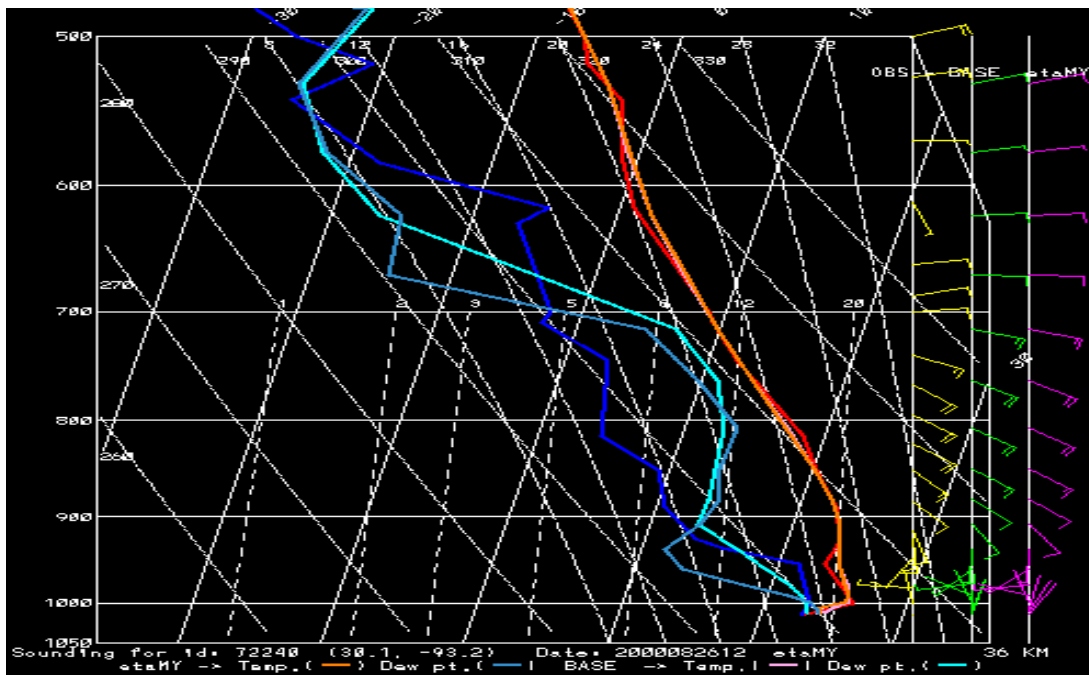


Figure 2b. Vertical variation of observed and simulated temperature and dew point temperature soundings for Lake Charles, LA, at 1200 UTC on August 26, 2000.

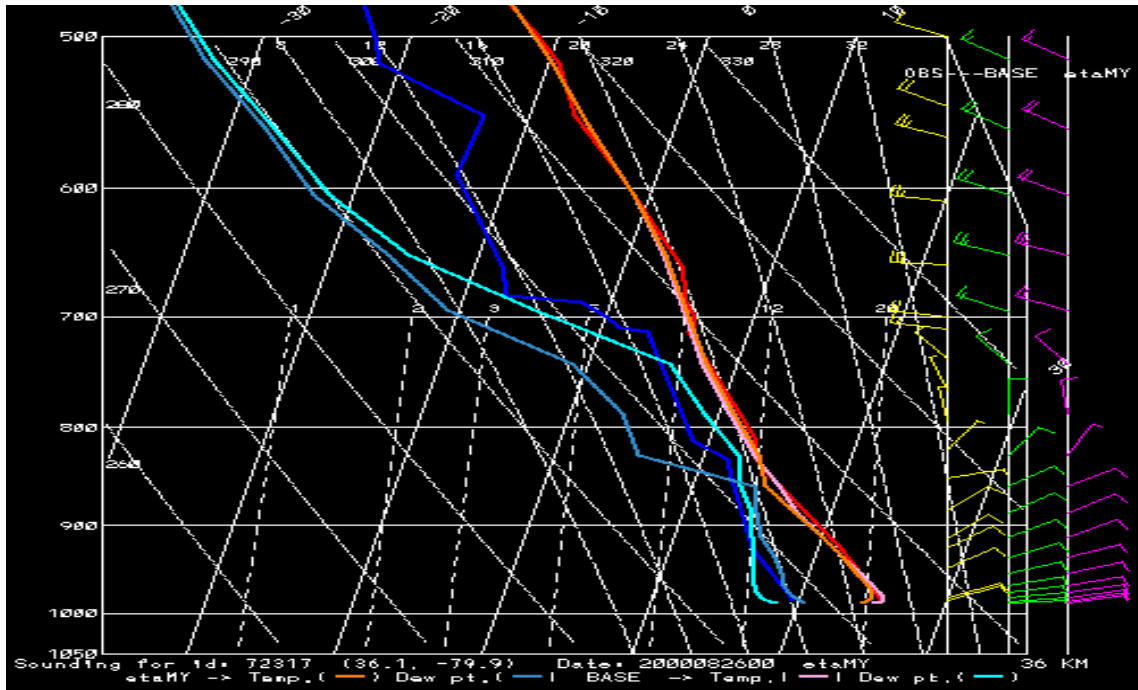


Figure 2c. Vertical variation of observed and simulated temperature and dew point temperature soundings for Greensboro, NC, at 0000 UTC on August 26, 2000.

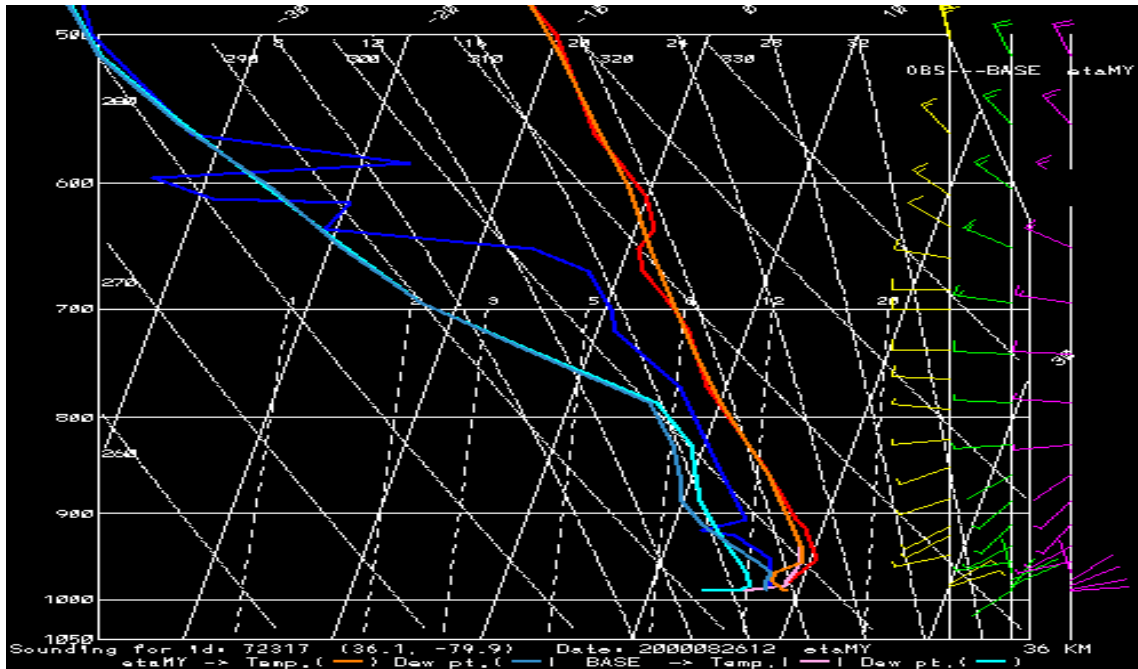


Figure 2d. Vertical variation of observed and simulated temperature and dew point temperature soundings for Greensboro, NC, at 1200 UTC on August 26, 2000.

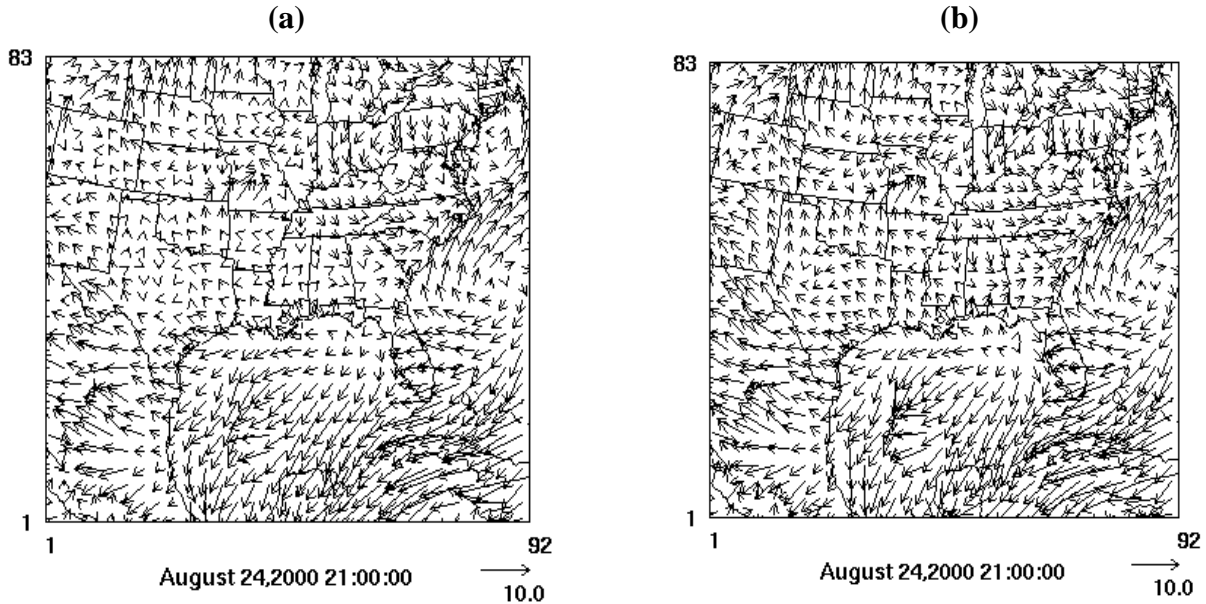


Figure 3. MM5 simulated horizontal wind vectors at 2100 UTC August 24, 2000, from (a) “Mrf” and (b) “Eta” simulations using the 36-km grids.

For the 36-km grid resolution simulations, we developed precipitation analysis diagrams for comparison with those developed by the Climate Prediction Center (referred to as CPC) (see <http://www.cpc.noaa.gov/>). The CPC dataset is derived from three sources: daily co-op stations from the National Climatic Data Center, the CPC dataset including data from the River Forecast Centers, and daily accumulations from an hourly precipitation dataset. There are about 13,000 station reports each day. The data were quality controlled to eliminate duplicates and overlapping stations, and standard deviation and buddy checks were applied. They were then gridded into $0.25^\circ \times 0.25^\circ$ using a Cressman Scheme. Note that precipitation amounts and distributions over oceanic regions may not be reliable due to a lack of data and interpolation artifacts.

Further, we completed 12- and 4-km grid resolution simulations for the “Mrf” and “Eta” cases, and developed statistics for evaluating the results obtained. We also obtained GOES-based remotely sensed data, and during the project’s second year these data were used to evaluate cloud fractions and insolation simulated by the MM5 using the best modeling configuration. In all figures below showing time series, the observations are referred to as “Obs” and the model results obtained using the two ABL schemes are referred to as “Mrf” and “Eta”. In the quantity “(M–O)”, which is used in preparing many statistics such as bias, “M” represents the modeled value and “O” represents the observed/measured value of a variable. Thus, if (M–O) is positive, the model is overpredicting that variable, and if (M–O) is negative the model is underpredicting.

Figures 4a, 4b, and 4c show accumulated precipitation data analyzed by the CPC and values obtained from “Mrf”, and “Eta”, respectively, for a period of 24 h ending at 1200 UTC 24 August 2000. In general, simulated precipitation is qualitatively very similar in “Mrf” and “Eta”. Over the region of specific interest to this project (i.e., eastern Texas), “Eta” leads to more

precipitation than in “Obs” (i.e., CPC) and in “Mrf”. The overall precipitation patterns in “Mrf” are marginally better than those in “Eta”. Figures 5a, 5b, and 5c are analogous figures for a period of 24 h ending at 1200 UTC 28 August 2000. Again, over the eastern Texas region the “Eta” case overpredicts the precipitation when compared to “Obs” and “Mrf”, even though the spatial distribution and rate are very similar.

Since the 12-km grid resolution simulations were primarily used to provide lateral boundary conditions to the 4-km grid resolution domains, and our focus was on model simulations using the high-resolution grids, we present here evaluation results for the 4-km grids for “Mrf” and “Eta”. Figure 6a shows the temporal variation of near-surface temperature (K) for “Obs”, “Mrf”, and “Eta”. During this five-day period, observations indicated a warming trend. In general, both “Mrf” and “Eta” simulate this trend well, with the exception of the last day of simulation. “Mrf” and “Eta” both have a maximum cooler bias during the daytime maximum and nighttime minimum temperature occurrence period. Figure 6b shows the temporal variation of bias in near-surface temperature for “Mrf” and “Eta”. In a general sense, “Mrf” has a lesser temperature bias (by about 1-2 K) compared to “Eta”. The large positive bias present at about 36 h of simulation in both the cases is due to the model’s inability to simulate a thunderstorm that was observed during that time. This led to an unrealistic heating due to the absence of modeled clouds at that time. Barring this incident, “Mrf” seemed to be a better choice, at least for temperature simulations.

Figure 7a shows the temporal variation of bias for the near-surface water vapor mixing ratio (g/kg). For “Mrf”, there exists a significant dry bias, particularly during the second and fourth days of simulation, as compared to “Eta”, which has a moist bias during that time. Similar results are found in the RMSEs shown in Figure 7b. To discover the main reasons for the presence of large RMSEs in “Mrf”, we intercompared the model-simulated precipitation amounts and spatial distribution with those from the CPC precipitation analysis shown in later figures. Figures 8a and 8b indicate the temporal variation of RMSE for near-surface wind speed and its direction. In the “Eta” case, the RMSEs are smaller than in the “Mrf” case. However, errors in the wind direction are smaller in “Mrf” than in “Eta”. Figure 9a shows the accumulated total precipitation from CPC for a period of 24 h ending at 1200 UTC 24 August 2000. Figures 9b and 9c show modeled accumulated total precipitation for the “Mrf” and “Eta” cases, respectively, for the same period as in the CPC analysis. It can be seen that “Eta” leads to overprediction of precipitation as compared to “Obs” (i.e., CPC) and “Mrf”. This leads to spurious cloud cover affecting the photolysis rates, which play an important role in ozone formation during the daytime. A similar result was also found for the precipitation during the rest of the simulation days; as an additional analysis, we present the accumulated precipitation ending at 1200 UTC 28 August 2000 in Figures 10a, 10b, and 10c for the 4-km grids. Again, there is a strong indication of spurious precipitation in “Eta” while “Obs” and “Mrf” indicate near-clear sky conditions.

In general, the temperature and wind speed simulations in “Eta” compared well with observations, while the mixing ratio and wind directions simulated by “Mrf” compared well with observations. However, precipitation was overestimated in “Eta” while slightly underestimated in “Mrf”. For these reasons, we strongly believed that the “Mrf” simulations, in general, were usable to drive the air quality model. We therefore chose to utilize the “Mrf” simulations as meteorological inputs to drive the MAQSIP-VGR.

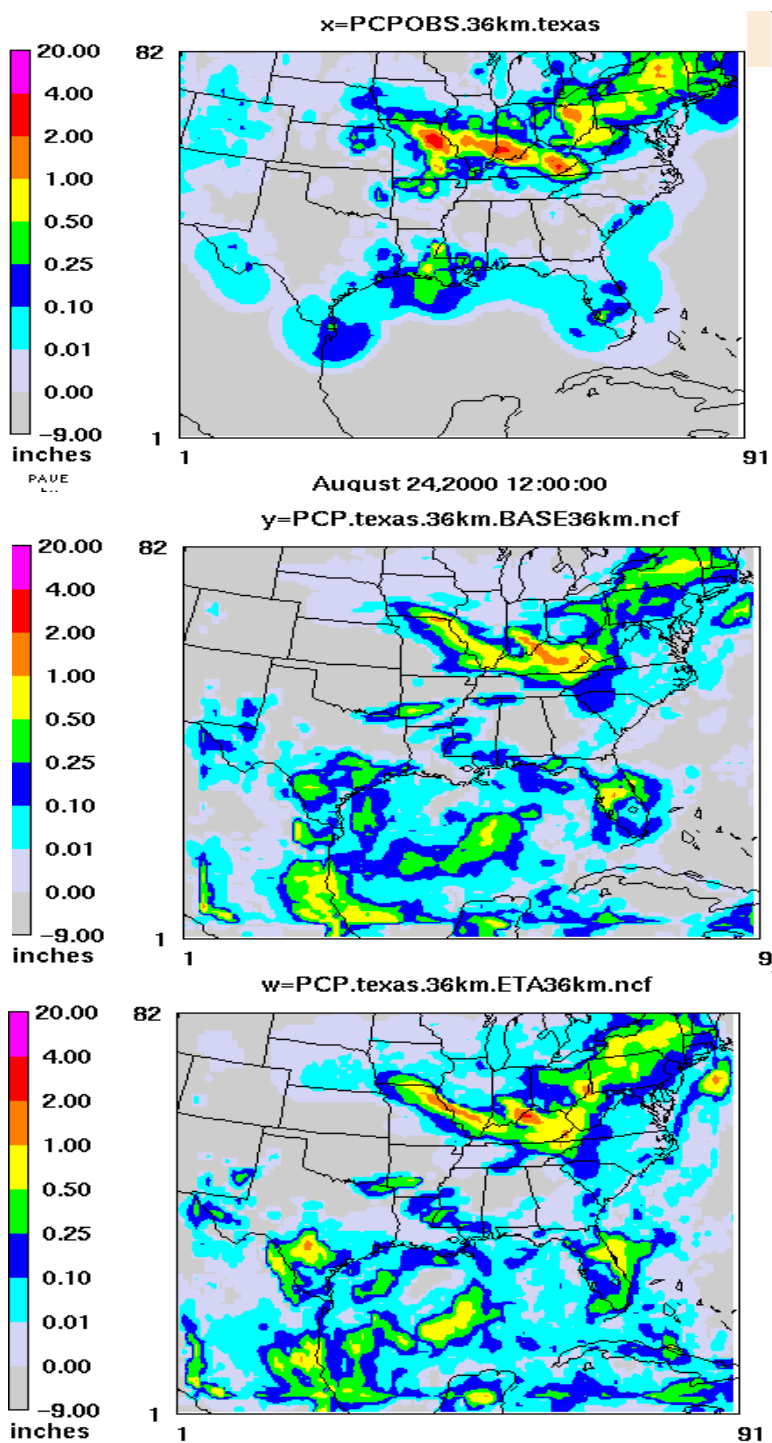


Figure 4. Accumulated precipitation (inches) for a period of 24 h ending at 1200 UTC 24 August 2000 from the (a) CPC analysis, (b) "Mrf", and (c) "Eta" cases.

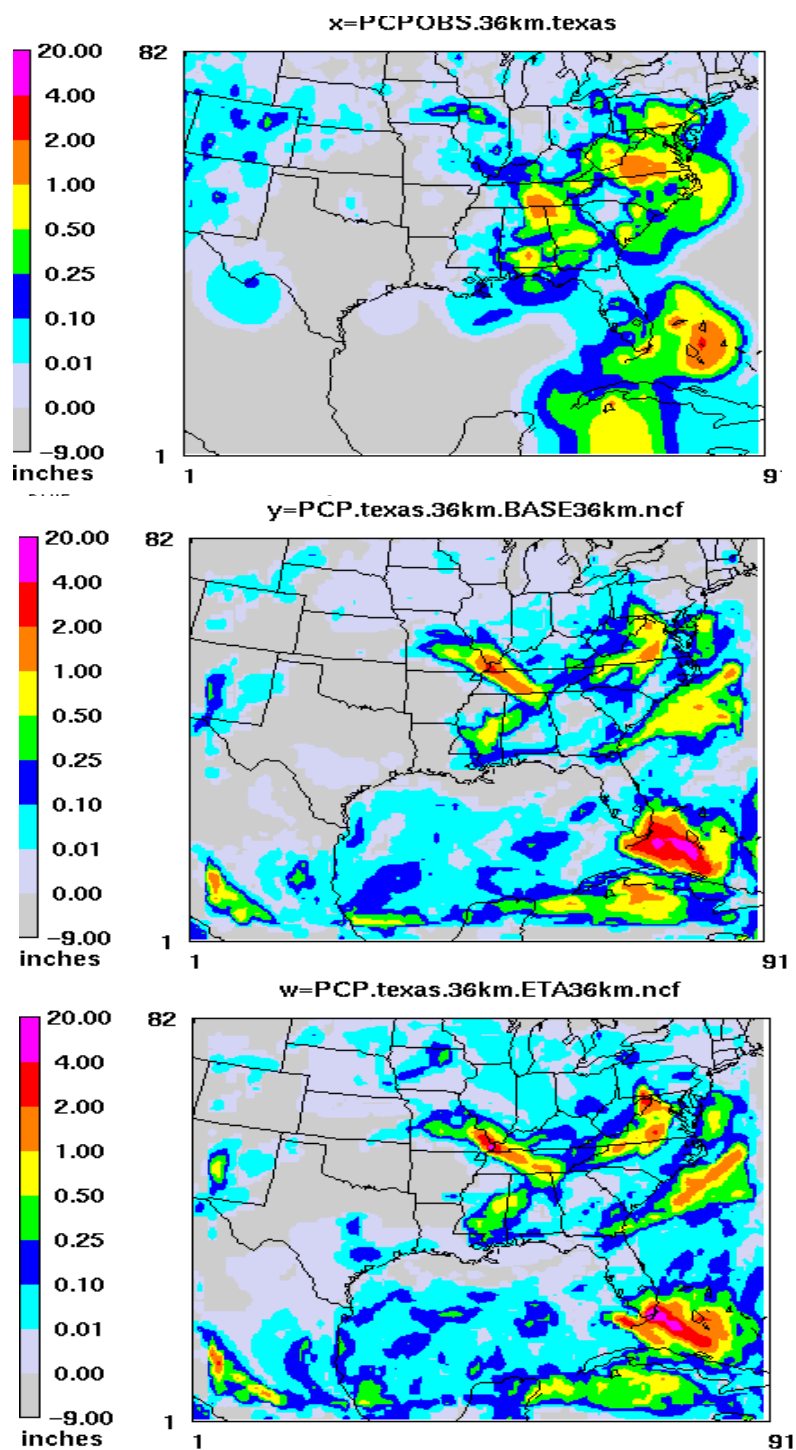


Figure 5. Accumulated precipitation (inches) for a period of 24 h ending at 1200 UTC 28 August 2000 from the (a) CPC analysis, (b) "Mrf", and (c) "Eta" cases.

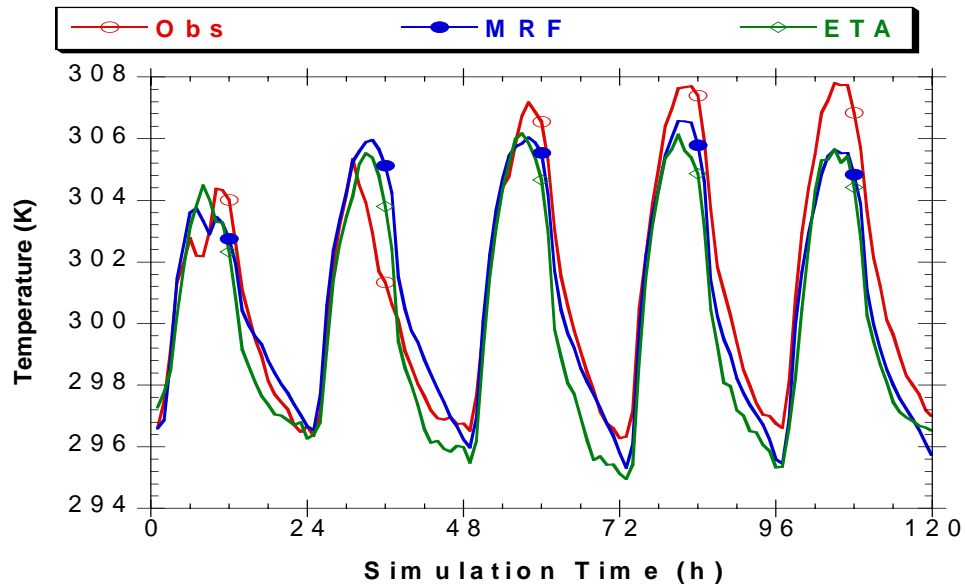


Figure 6a. Temporal variation of near-surface air temperature averaged over all of the measurements and corresponding modeled values, starting at 1200 UTC 23 August 2000 for the “Mrf” and “Eta” cases for 4-km grids.

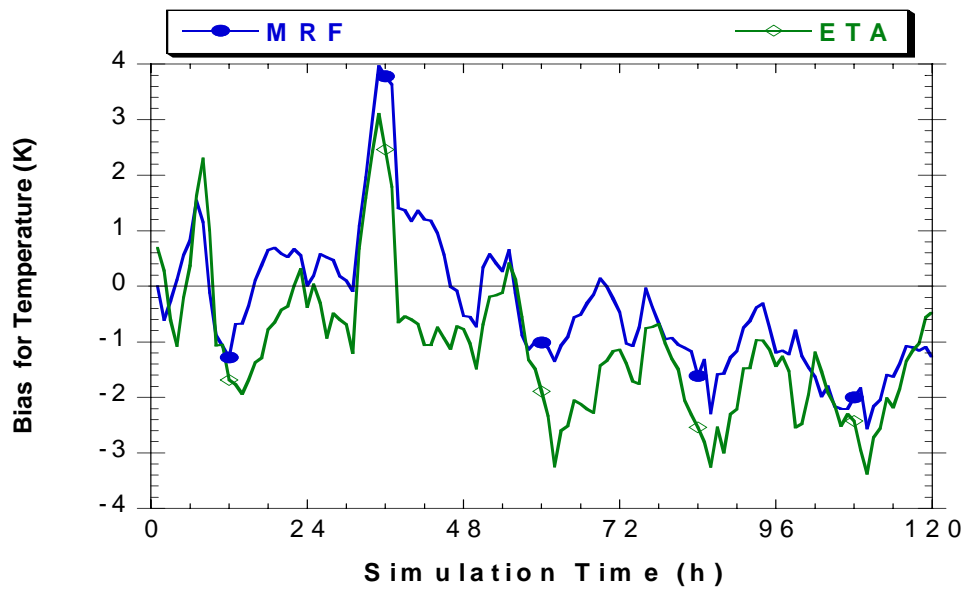


Figure 6b. Temporal variation of bias in the averaged near-surface air temperature for the “Mrf” and “Eta” cases, starting at 1200 UTC 23 August 2000.

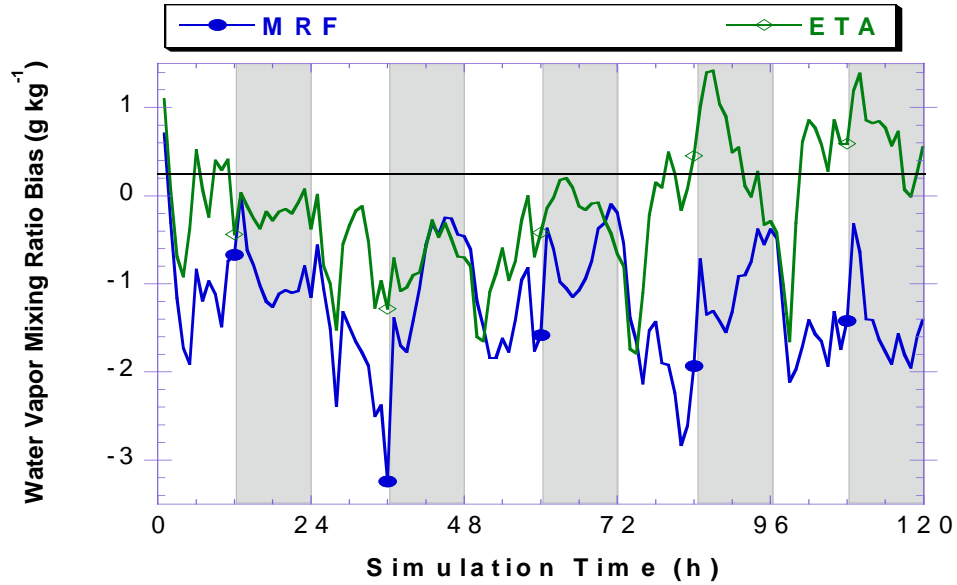


Figure 7a. Temporal variation of bias in the averaged near-surface water vapor mixing ratio for the “Mrf” and “Eta” cases, starting at 1200 UTC 23 August 2000.

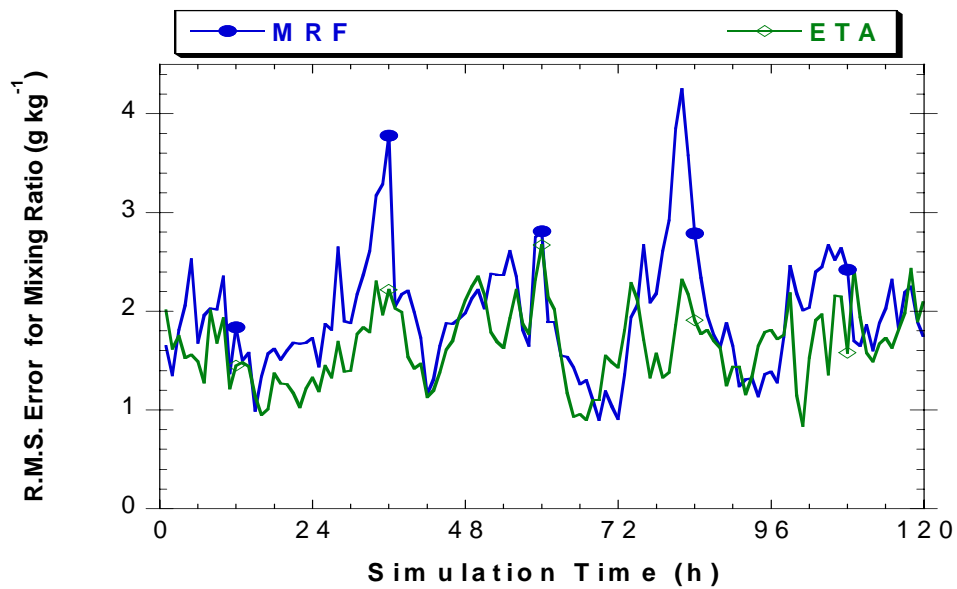


Figure 7b. Temporal variation of root mean square error in the averaged near-surface water vapor mixing ratio for the “Mrf” and “Eta” cases, starting at 1200 UTC 23 August 2000.

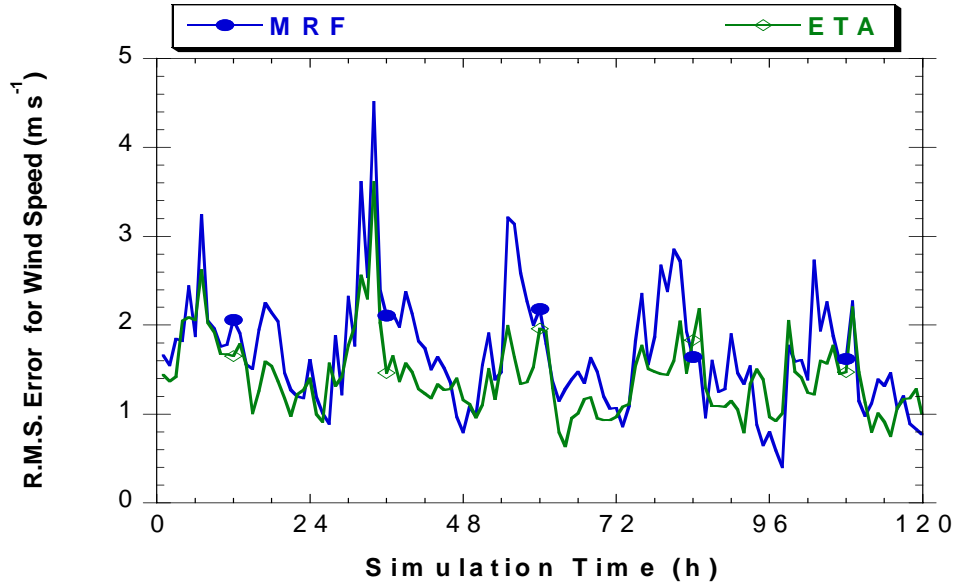


Figure 8a. Temporal variation of root mean square errors in the averaged near-surface horizontal wind speed for the “Mrf” and “Eta” cases, starting at 1200 UTC 23 August 2000.

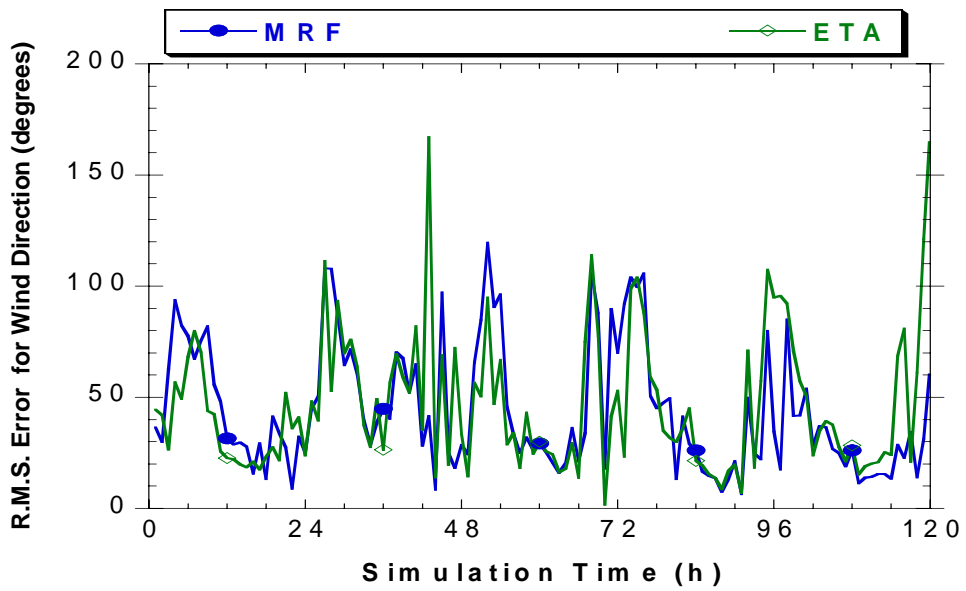


Figure 8b. Temporal variation of root mean square errors in the averaged near-surface horizontal wind direction for the “Mrf” and “Eta” cases, starting at 1200 UTC 23 August 2000.

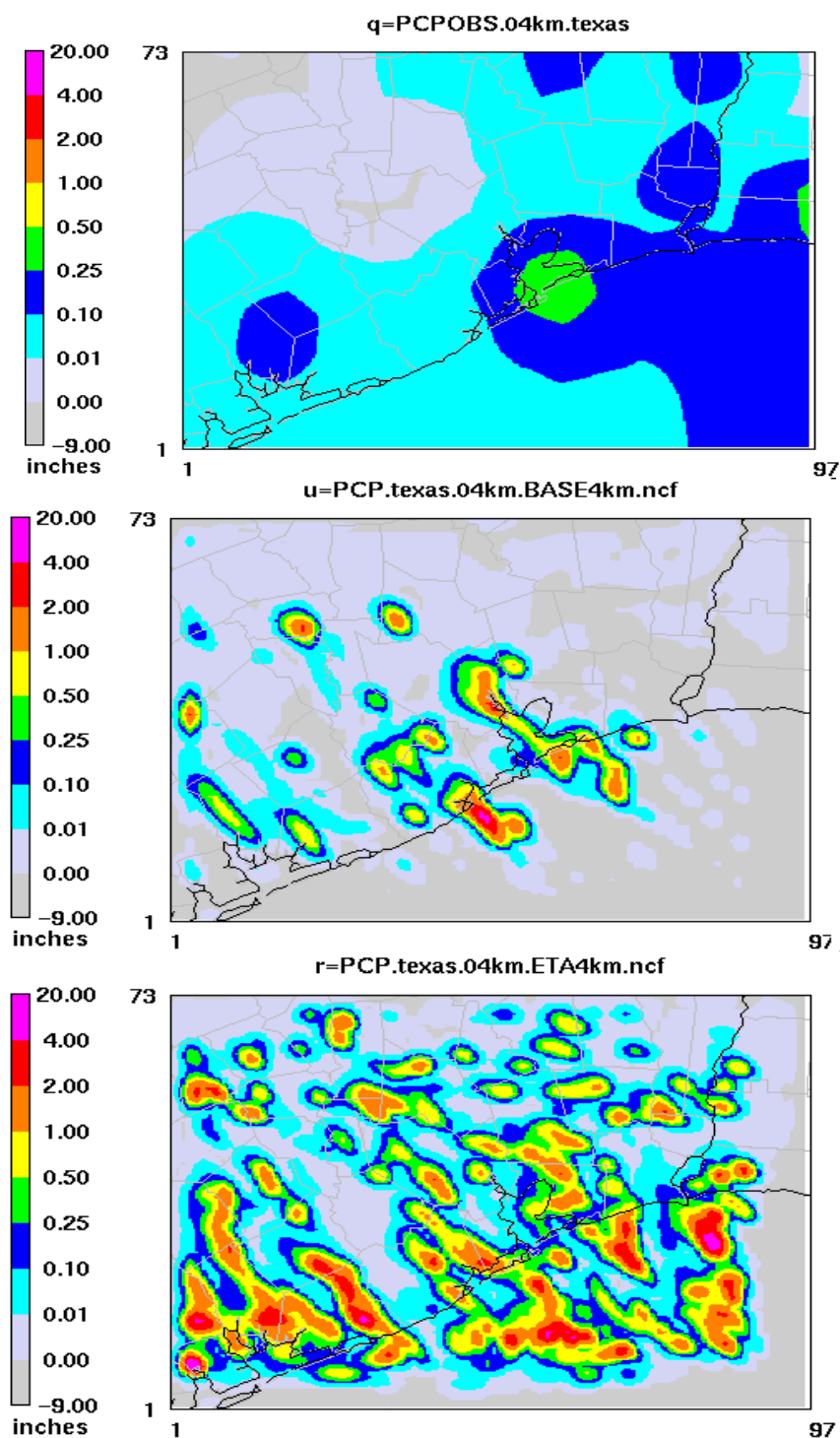


Figure 9. Accumulated precipitation for the (a) "Obs", (b) "Mrf" and (c) "Eta" cases, ending at 1200 UTC 24 August 2000.

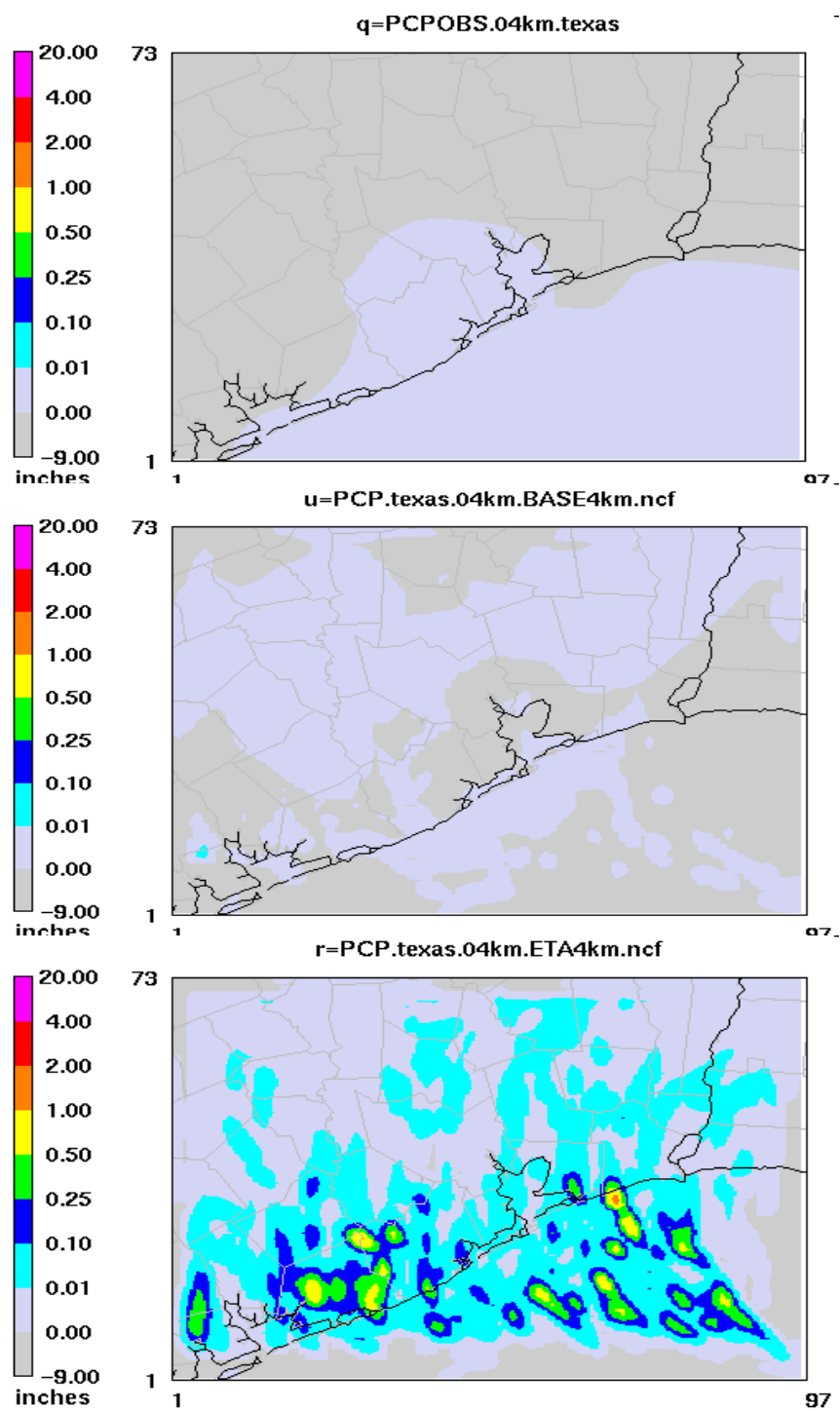


Figure 10. Accumulated precipitation for the “Obs”, “Mrf” and “Eta” cases, ending at 1200 UTC 28 August 2000.

2.3 Task 3: Assimilate Surface Observations to Improve MM5 Simulations

Two types of surface observations were available for use in the MM5 simulations and evaluations: traditionally available observations from routine land-based measurements (at 2 m and 10 m above ground level [AGL]), and remotely sensed satellite-based observations

2.3.1. Assimilation of Land-based Surface Observations using the FASDAS

Since uncertainty in the specification of vegetation and soil parameters and other modeling assumptions and discretizations leads to modeling errors, particularly near the surface, we used the Flux-Adjusting Surface Data Assimilation System (FASDAS) developed and tested by Alapaty et al. (2001a,b,c) to reduce these errors. We implemented the FASDAS into the MM5 using a sophisticated land surface model (Chen and Dudhia, 2001) and the Medium-Range Forecast (MRF) boundary layer scheme. In the FASDAS continuous surface data assimilation technique, abundant land-based surface measurements of temperature and relative humidity (dew point temperature) are used to nudge a 1-D model's lowest-layer air temperature and moisture along with the ground/skin temperature. To do this, surface-layer temperature and water vapor mixing ratio are directly assimilated by using the analyzed surface data, while ground/skin temperature and soil moisture are indirectly assimilated, thereby maintaining greater consistency between the soil temperature and moisture fields and the surface-layer mass-field variables. The FASDAS then uses the differences between the observations and model predictions to estimate adjustments to the surface fluxes of sensible and latent heat. These adjustment fluxes are then applied in calculating a new estimate of the soil/ground temperature and soil moisture for each soil layer using the Chen and Dudhia land-surface model, thereby affecting the predicted surface fluxes in the subsequent time step. This indirect data assimilation was applied simultaneously with the direct assimilation of surface data in the model's lowest layer, thereby maintaining greater consistency between the ground temperature and the surface layer mass-field variables. Using this technique was critical for minimizing errors in the ground temperature and temperature gradients across coastal regions for realistic simulation of land-sea breeze circulations.

After successful implementation of the FASDAS into the MM5, we performed a test simulation for the same 36-km grid employed in Section 2.2 using the FASDAS to compare with the "Mrf" simulations described in Section 2.2. One reason for using the MRF scheme as the default ABL scheme in the MM5 simulations is the fact that it is the most widely used boundary layer scheme.

We then performed a comprehensive analysis and evaluation of the results obtained using the FASDAS technique in the MM5. The MM5 simulations using the MRF scheme, which in Section 2.2 were referred to as "Mrf", are referred to here as "Base" because they were used as a benchmark to evaluate the MM5 results obtained using the FASDAS. We first present results obtained using the 36-km grids, followed by results from the 4-km grids.

Figure 11 shows the number of hourly surface observations used as a function of time to develop several statistical indices to evaluate MM5 model simulations both with and without using the FASDAS. Each of observational sites is paired with the corresponding grid cell in the modeled domain for preparing statistics. Simulated temperature, mixing ratio, and winds for these representative grid cells were then interpolated from the model's lowest-level altitude to the respective measurement heights to facilitate direct intercomparison. In many of the figures the

observations are referred to as “Obs”; the model results obtained using the MRF scheme, which did not assimilate any surface data, are “Base”; and the simulations that used MRF along with the FASDAS are “Fasdas.” The quantity $(M-O)$ is used in preparing many statistics, where M represents the modeled value and O represents the observed/measured value of a variable. Thus, if $(M-O)$ is positive, the model is overpredicting that variable, and if $(M-O)$ is negative the model is underpredicting.

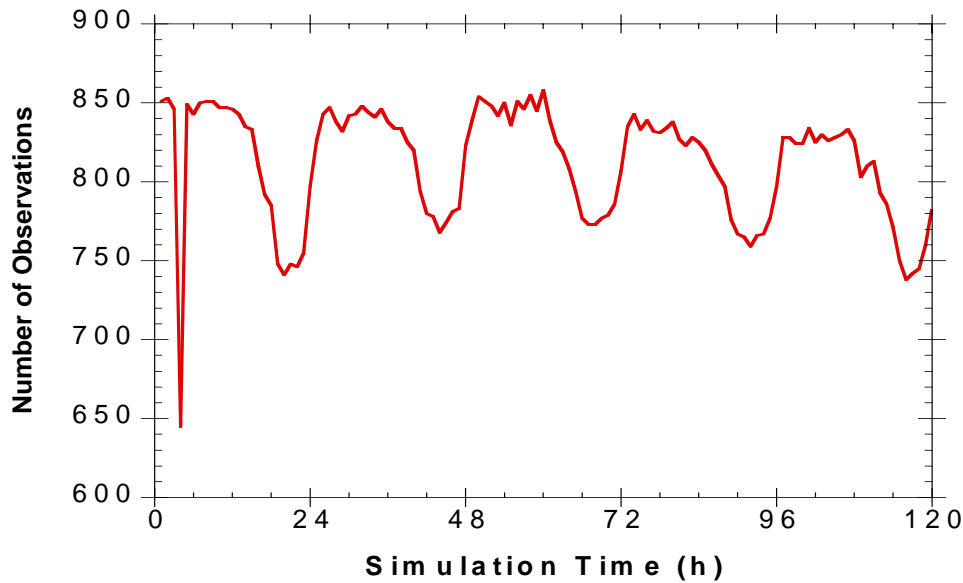


Figure 11. Temporal variability in the number of available surface observations used in developing statistical indices for the domain using 36-km grid resolution. Zero on the x-axis corresponds to 1200 UTC 23 August 2000.

Figure 12 shows the temporal variation of near-surface temperature (K). It is clear that the application of the FASDAS led to improved temperature simulations compared to the “Base” simulations. Improvement is also evident in the temporal variation of bias for near-surface temperature (K) (Figure 13). This result has favorable implications for air quality modeling because it could lead to improved representation of biogenic emission estimates over vegetated regions. Figure 14 shows the temporal variation of bias for near-surface water vapor mixing ratio (g/kg). When interpreting this figure, it is important to understand that the observations are available at 2 m AGL while the modeled values for water vapor mixing ratio were available at ~18 m AGL. Since there is no robust method for interpolating mixing ratio to the observational height of 2 m, we have used modeled values for the lowest model layer. Hence, the positive bias present in the “Fasdas” results at night may not necessarily indicate overprediction, since dew formation that may exist near the surface can lead to drier layers near the surface versus aloft. In general, model simulations for the “Fasdas” case compare favorably with observations, indicating overall improvements in the simulations compared with “Base.” This result could also have a positive impact on air quality model simulations through improved representation of H_2O_2 concentrations.

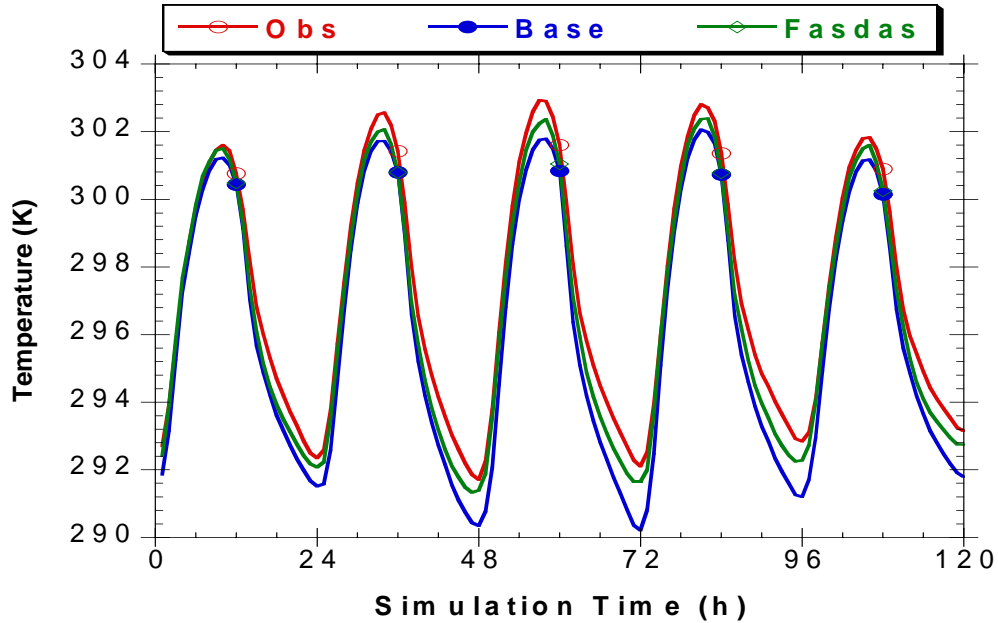


Figure 12. Temporal variation of near-surface air temperature averaged over all of the measurements and corresponding modeled values, starting at 1200 UTC 23 August 2000 for the domain D01 using the 36-km grid resolution.

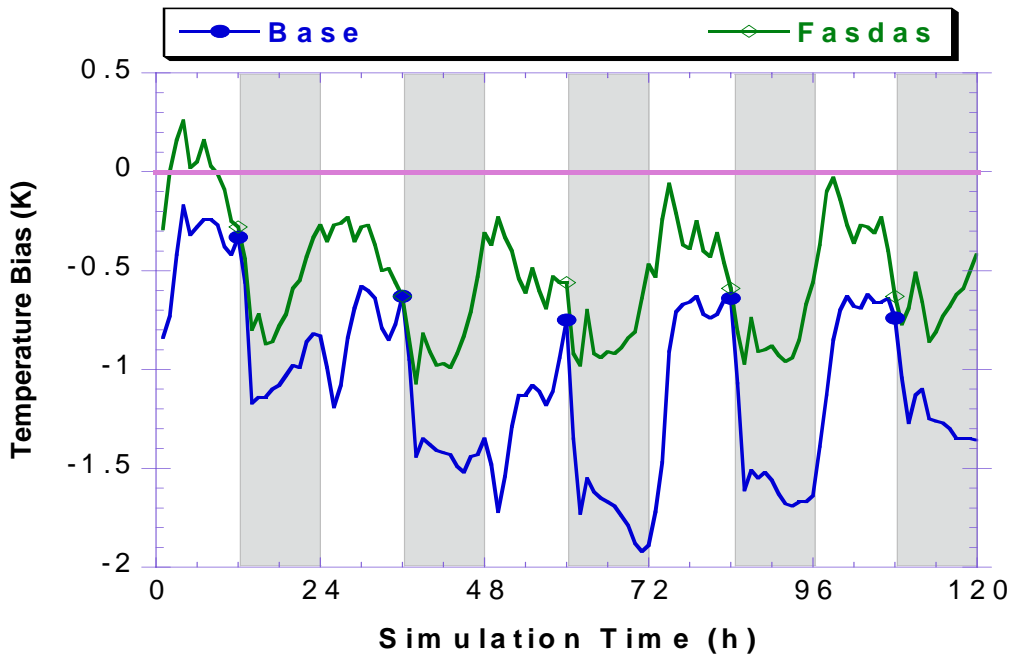


Figure 13. Temporal variation of bias in the averaged near-surface air temperature for the “Base” and “Fasd as” cases, starting at 1200 UTC 23 August 2000 (for 36-km grid resolution).

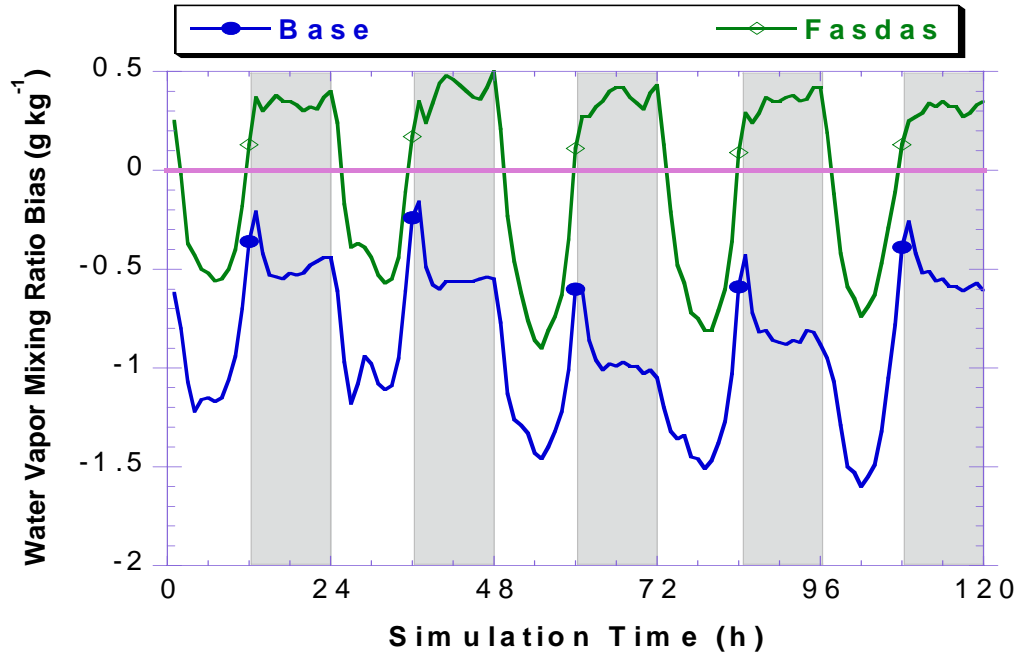


Figure 14. Temporal variation of bias in the averaged near-surface water vapor mixing ratio for the “Base” and “Fasdas” cases, starting at 1200 UTC 23 August 2000.

Figures 15 through 18, for four different geographic locations and dates, show the vertical variation in observed temperatures and dew point temperatures together with the corresponding modeled profiles obtained from the “Base” and “Fasdas” cases. Generally, there is improvement in the simulation of vertical soundings when FASDAS is used. Also, the differences between “Base” and “Fasdas” for wind speed and direction are negligible. In this case study, the FASDAS technique reduced errors in the modeled temperature and water vapor mixing ratio in the lowest layers and aloft. Thus, for 36-km grids, use of FASDAS led to improved simulations.

Legends for Figure 15 through 18:

Legend for Plotted Lines

—	Obs	T	—	Obs	T _d
—	Fasdas	T	—	Fasdas	T _d
—	Base	T	—	Base	T _d

Legend for Wind Barbs

- Yellow – “Obs”
- Green – “Base”
- Magenta – “Fasdas”

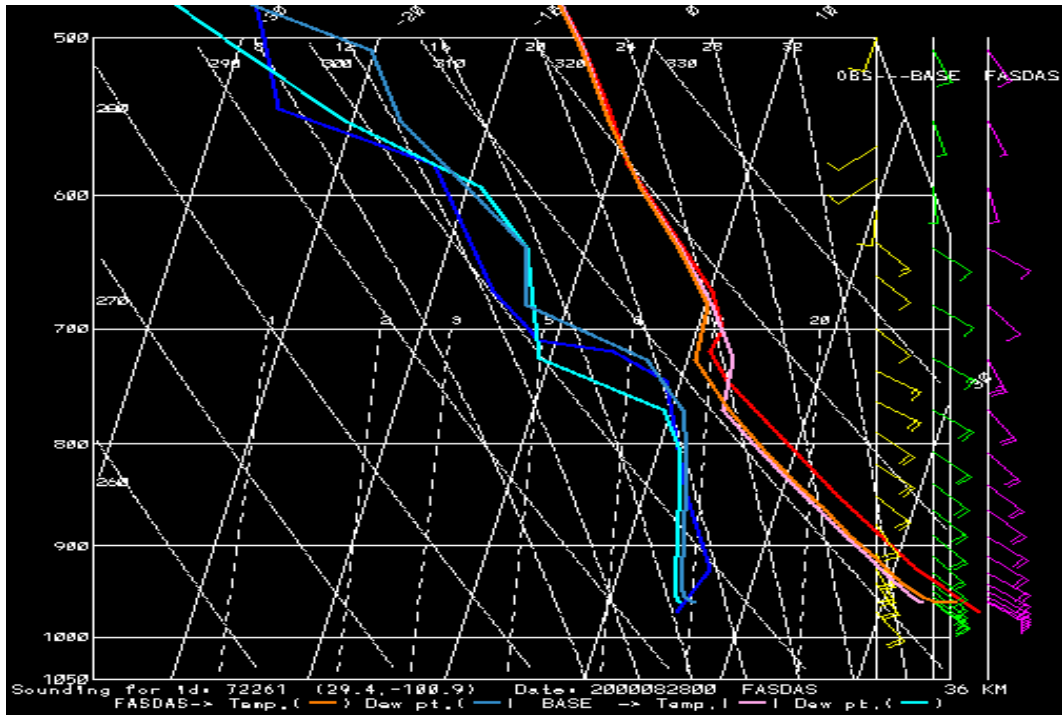


Figure 15. Vertical variation in temperature and dew point temperature from observations and the “Base” and “Fasd’as” cases at 0000 UTC 28 August 2000 for Del Rio, TX.

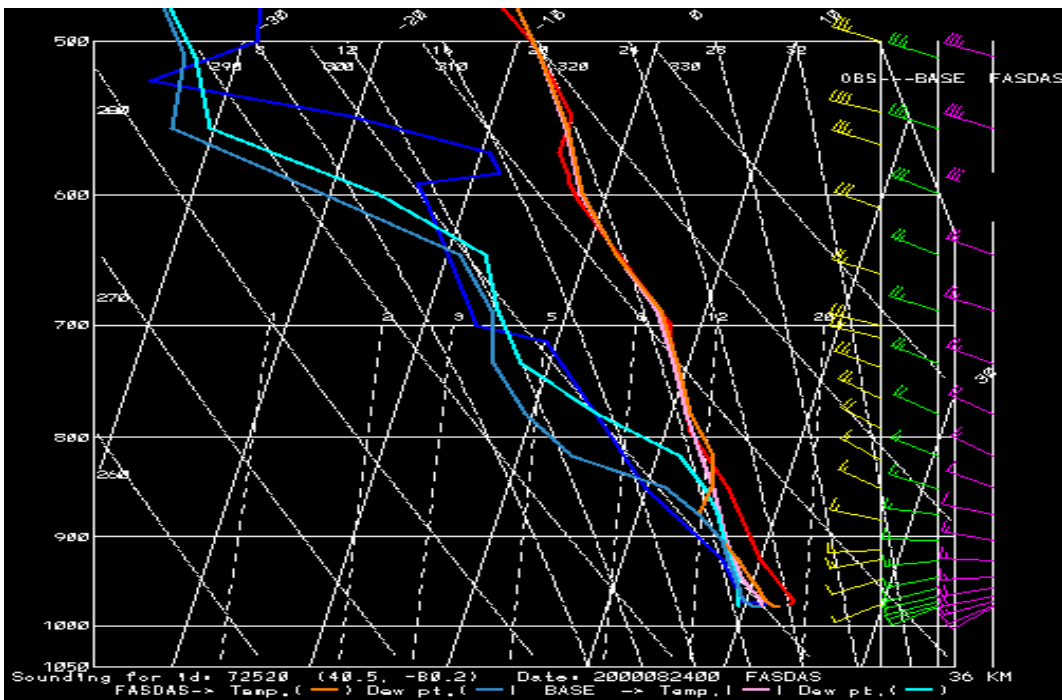


Figure 16. Vertical variation in temperature and dew point temperature from observations and the “Base” and “Fasd’as” cases at 0000 UTC 24 August 2000 for Pittsburgh, PA.

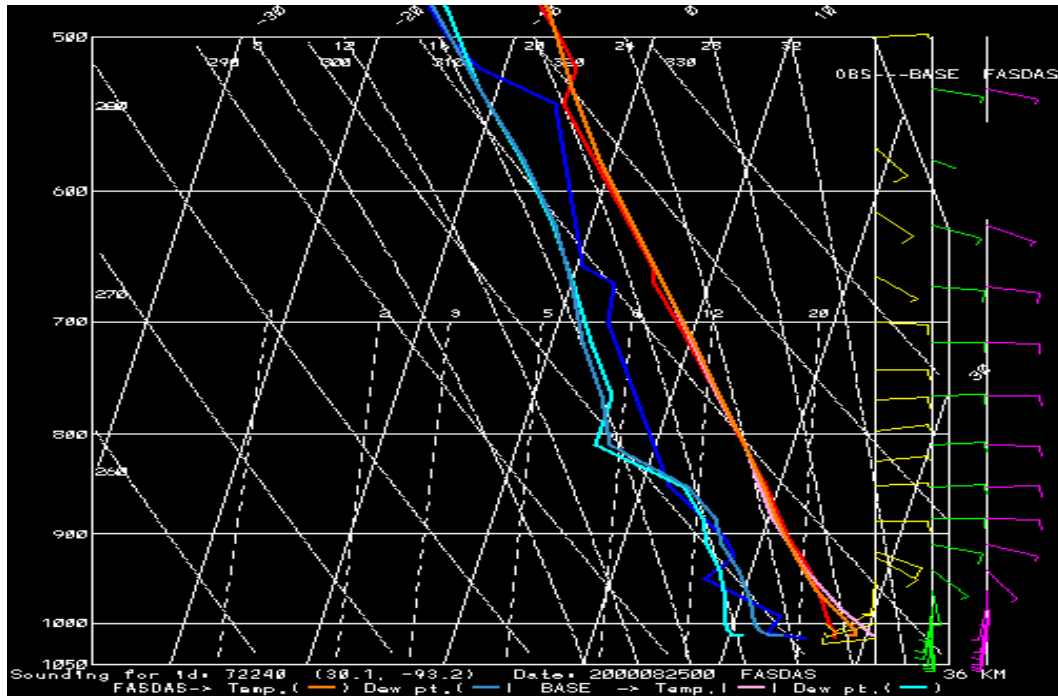


Figure 17. Vertical variation in temperature and dew point temperature from observations and the “Base” and “Fasdass” cases at 0000 UTC 25 August 2000 for Lake Charles, LA.

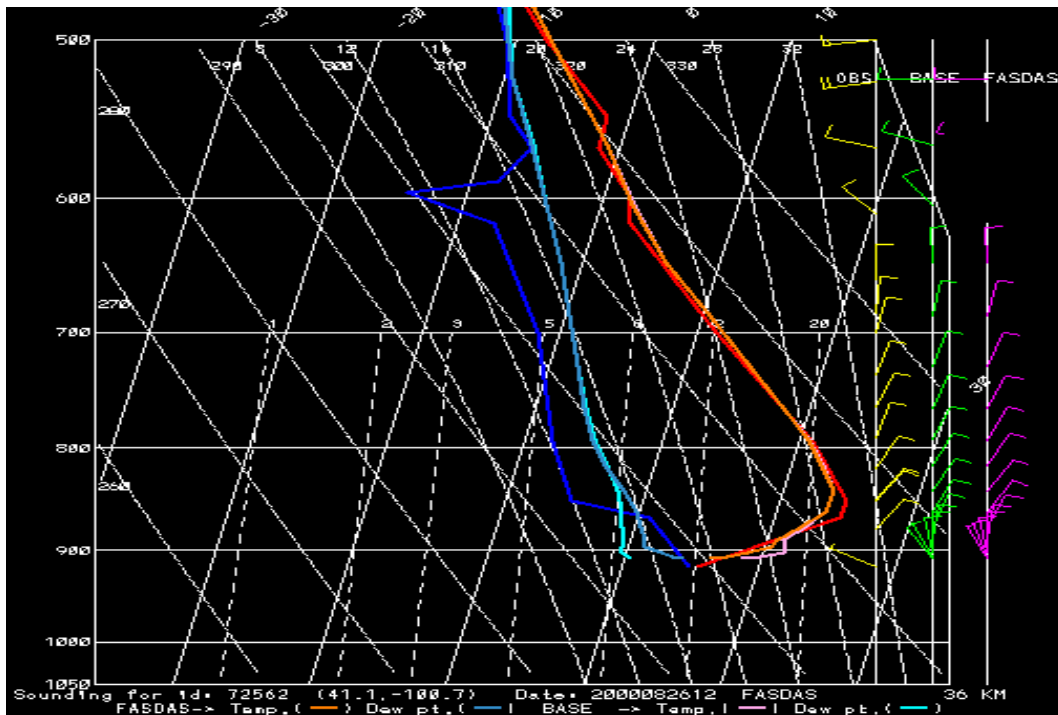


Figure 18. Vertical variation in temperature and dew point temperature from observations and the “Base” and “Fasdass” cases at 0000 UTC 26 August 2000 for North Platte, NB.

We acquired the CPC analyses for precipitation and compared them with the model simulations for the 36-km grids. Figures 19a, 19b, and 19c show the accumulated precipitation ending at 1200 UTC 24 August 2000 for “Obs”, “Base”, and “Fasdas”. The spatial distribution of precipitation in “Base” and “Fasdas” in general is very similar, with higher totals in “Fasdas”. Over eastern Texas, both cases (“Base” and “Fasdas”) overpredicted the precipitation estimates compared to observations. Analyzed and simulated precipitation totals for another 24 h, ending at 1200 UTC 28 August 2000, are shown in Figures 20a, 20b, and 20c. Observations indicated no traceable precipitation over southern and eastern Texas, while “Base” indicated trace amounts of precipitation covering southern Texas. In “Fasdas”, while no precipitation was simulated in the region immediately surrounding the Houston-Galveston area, south and north of it there exists an accumulated precipitation of about 0.1” that is not supported by observations. Analysis of precipitation distribution and magnitudes for the other days of simulation indicated mixed results; “Base” and “Fasdas” showed marked similarities and differences when compared to observed precipitation over different regions.

We now present a statistical evaluation of 4-km grid model simulations for “Base” and “Fasdas”. There are about 15 surface measurements available in the 4-km domain, and one upper-air sounding. These measurements, along with the CPC precipitation analysis, are used to evaluate the “Base” and “Fasdas” cases.

Figure 21a shows the temporal variation in the ~2 m AGL air temperature from “Obs”, “Base”, and “Fasdas” for the 4-km grid simulations. Both “Base” and “Fasdas” indicate similar magnitudes and temporal variation, with a small improvement in “Fasdas”. Prediction of cooler temperatures by both of them is caused mainly by reduced insolation due to cloud cover (not shown). Similar results can be found in the RMSE distribution shown in Figure 21b, which indicates slightly improved performance by “Fasdas”.

The temporal variation in the averaged near-surface water vapor mixing ratio for “Obs”, “Base”, and “Fasdas” is shown in Figure 22a and the RMSEs for these two cases are shown in Figure 22b. There is a marginal improvement in “Fasdas” compared to “Base”. Figures 23a and 23b give the RMSEs in the simulated horizontal wind speed and its direction for the near-surface winds. There is a marginal improvement in “Base” compared to “Fasdas” for the wind speed, while there is not much difference in the wind direction simulations.

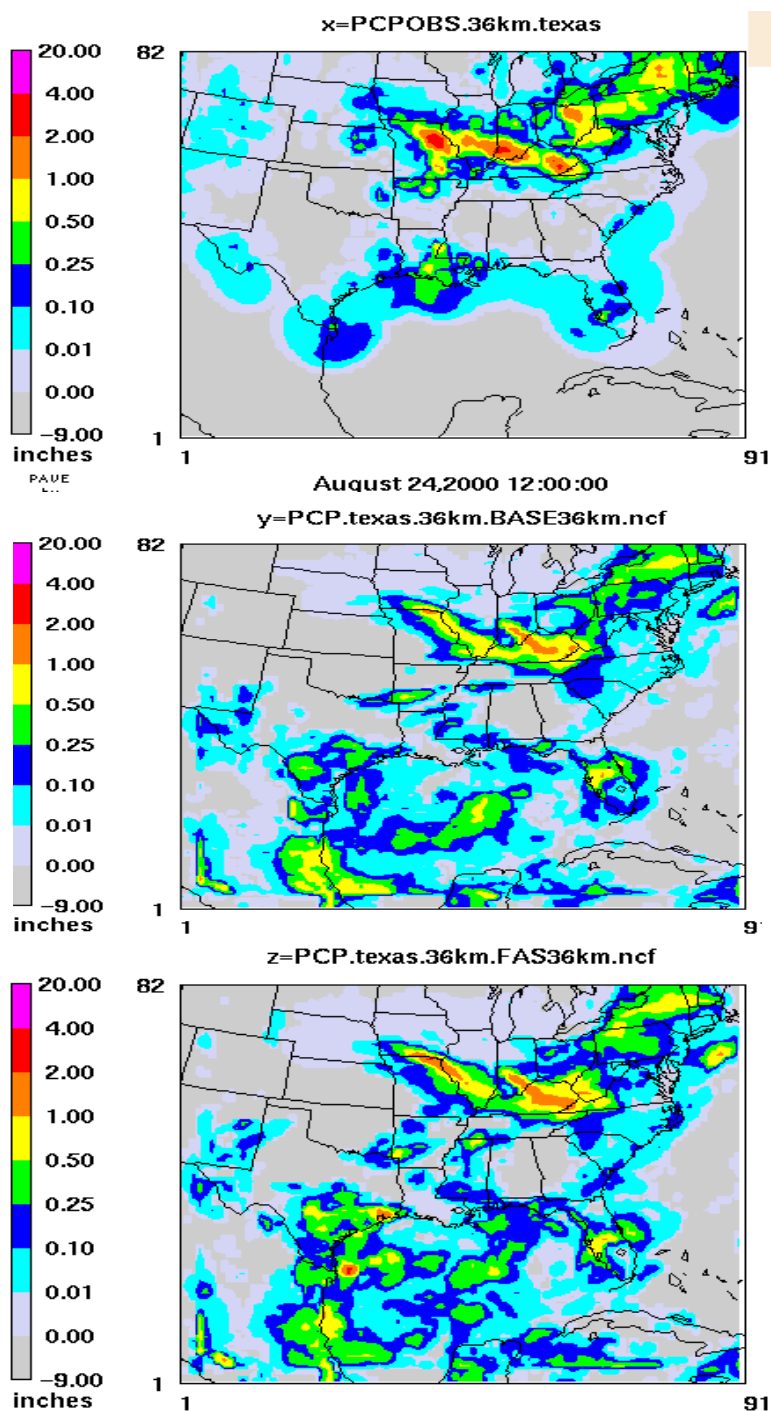


Figure 19. Accumulated precipitation (inches) for a period of 24 h ending at 1200 UTC 24 August 2000 from the (a) CPC analysis, (b) "Base", and (c) "Fasdas" cases.

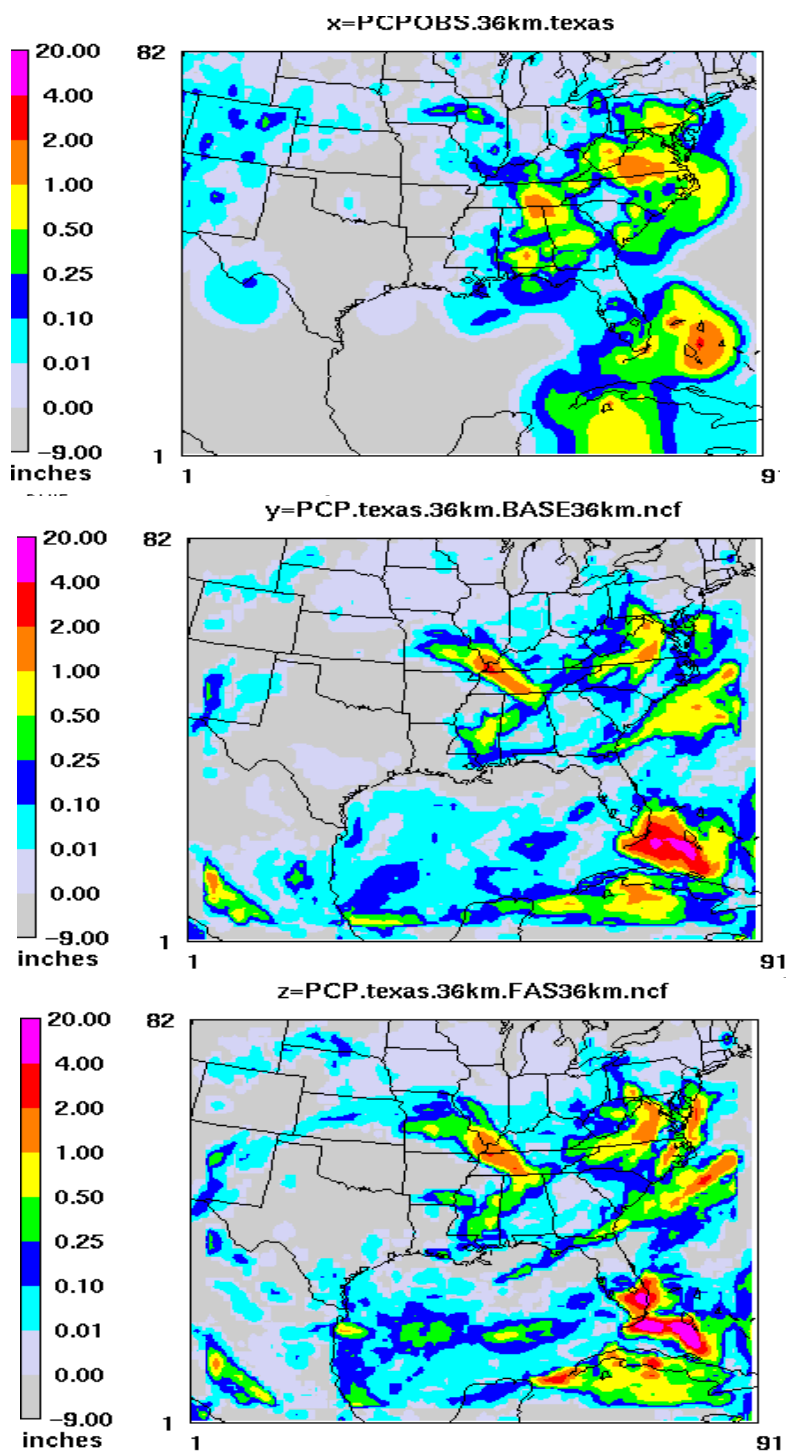


Figure 20. Accumulated precipitation (inches) for a period of 24 h ending at 1200 UTC 28 August 2000 from the (a) CPC analysis, (b) "Base", and (c) "Fasdas" cases.

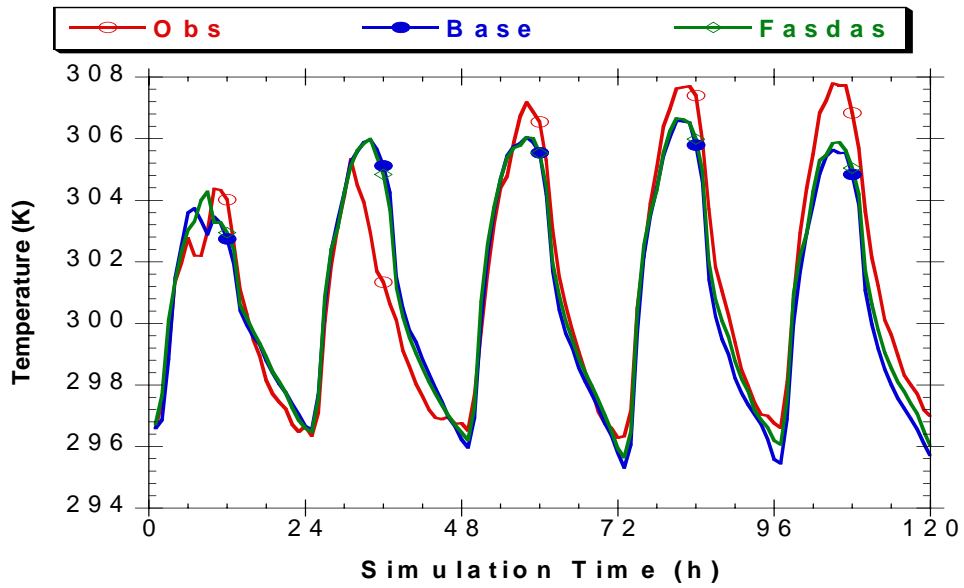


Figure 21a. Temporal variation of near-surface air temperature averaged over all of the measurements and corresponding modeled values, starting at 1200 UTC 23 August 2000 for the “Base” and “Fasd as” cases for 4-km grids.

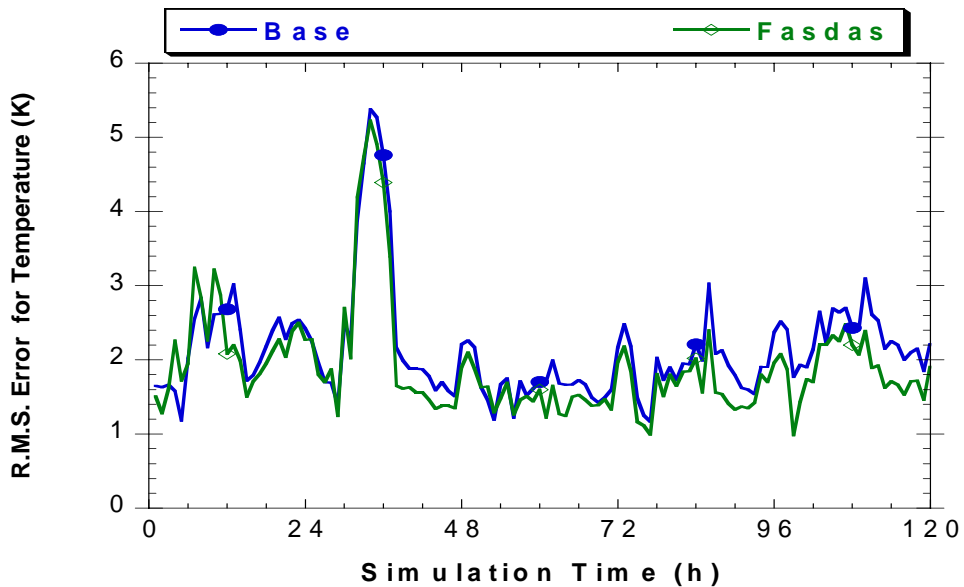


Figure 21b. Temporal variation of near-surface air temperature RMSEs for the “Base” and “Fasd as” cases using 4-km grids starting at 1200 UTC 23 August 2000 .

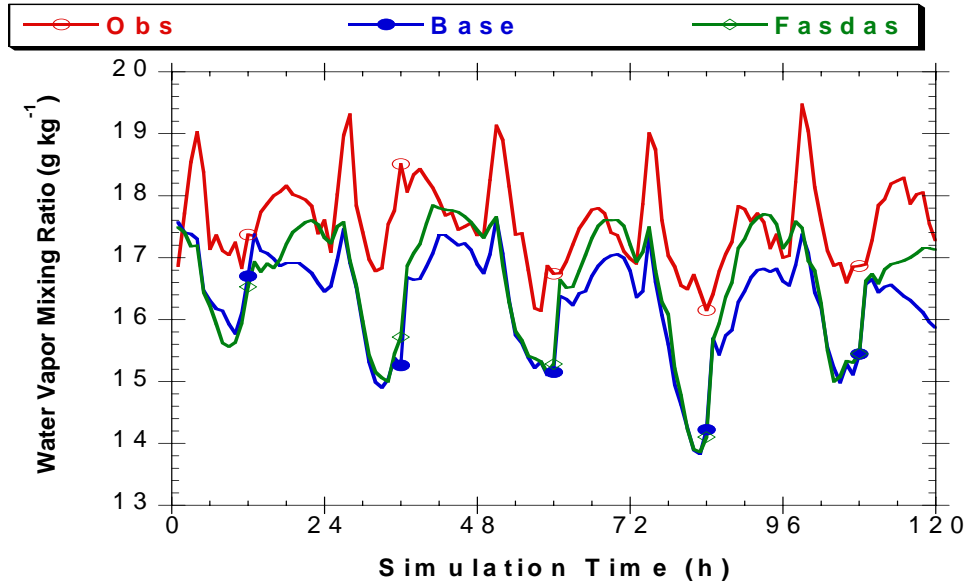


Figure 22a. Temporal variation of averaged near-surface water vapor mixing ratio for the “Base” and “Fasdas” cases, starting at 1200 UTC 23 August 2000.

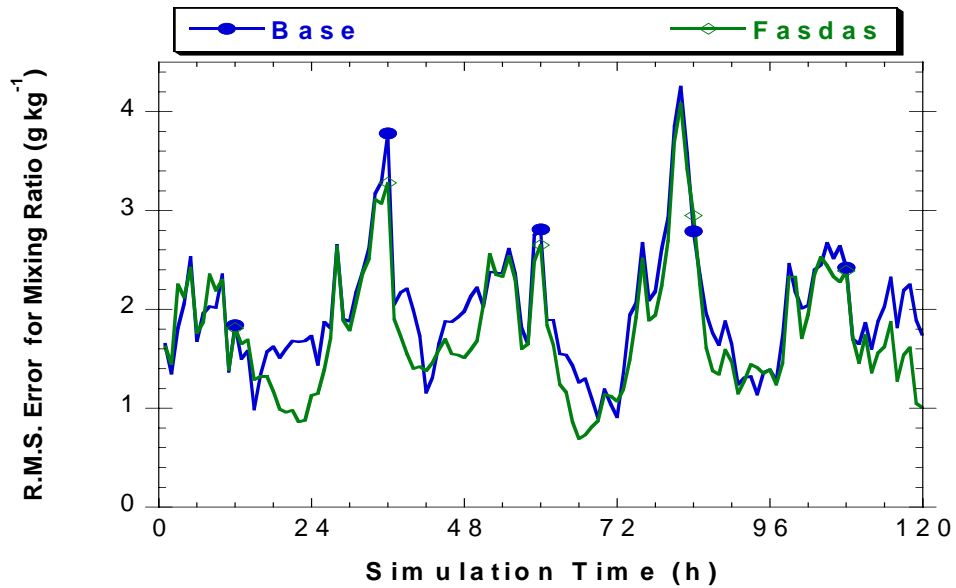


Figure 22b. Temporal variation of near-surface water vapor mixing ratio RMSEs for the “Base” and “Fasdas” cases using 4-km grids starting at 1200 UTC 23 August 2000.

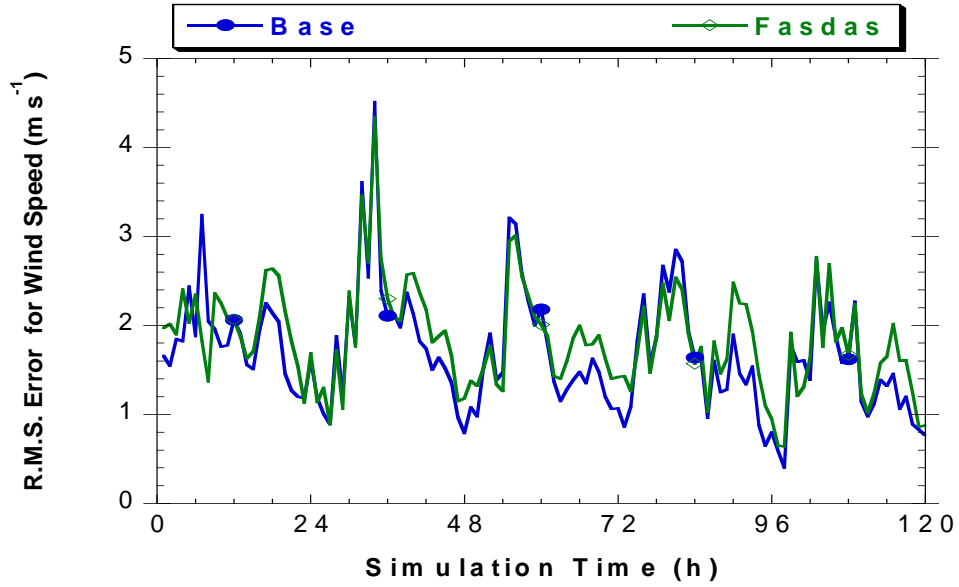


Figure 23a. Temporal variation of near-surface horizontal wind speed RMSEs for the “Base” and “Fasd as” cases using 4-km grids starting at 1200 UTC 23 August 2000 .

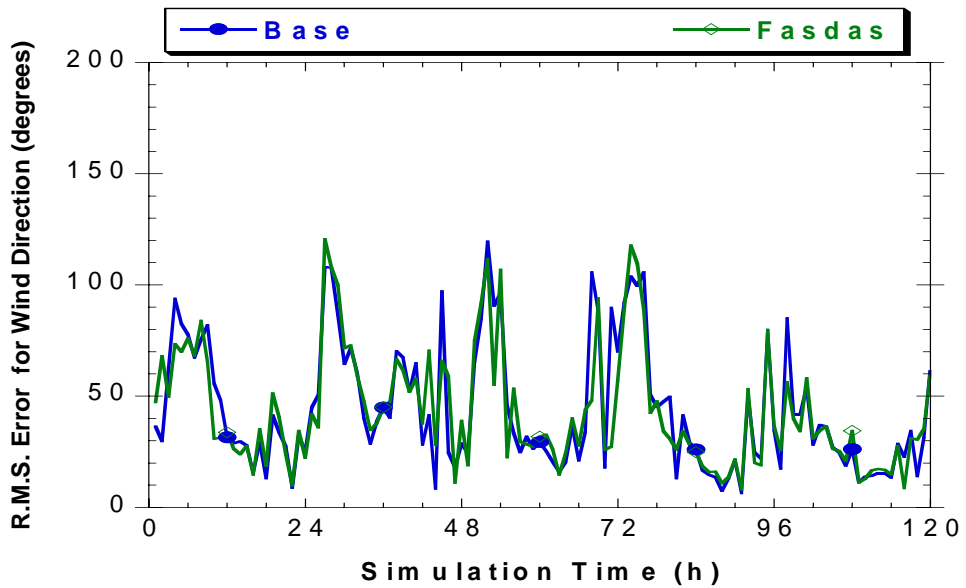


Figure 23b. Temporal variation of near-surface horizontal wind direction RMSEs for the “Base” and “Fasd as” cases using 4-km grids starting at 1200 UTC 23 August 2000 .

Figures 24a and 24b show the accumulated precipitation in “Obs”, “Base”, and “Fasdas” ending at 1200 UTC 24 August respectively. There are some minor differences between “Base” and “Fasdas” in the simulated precipitation, with higher magnitudes in “Fasdas”. Precipitation simulations for the period ending 1200 UTC 28 August also indicate insignificant differences between “Base” and “Fasdas”. In general, these simulations qualitatively compare well with the CPC analysis (“Obs”).

We further examined the single sounding present in the simulation domain and compared it with the measured soundings for several periods of model simulation. These analyses indicated that the “Base” and “Fasdas” soundings for temperature, moisture, and winds showed virtually no differences between them. The main reason for these results is that there are no surface measurements available in the neighborhood of the sounding measurements, hence no improvements were found over this region.

Note that only about 10 surface measurements are available for use by the FASDAS to correct the modeling errors, out of about 7,000 grid points. Thus, very minor improvements are expected in “Fasdas” for the 4-km grids, as opposed to the 36-km grids, where about 800 surface measurements are used in “Fasdas”.

In general, for the 4-km grids, there were minor improvements in “Fasdas” compared to “Base” and compared to that in the 36-km grids. Hence, we utilized “Fasdas” in creating final meteorological fields in the final modeling configuration.

2.3.2 Ingestion of Satellite-Measured Sea Surface Temperatures into the MM5

To successfully simulate land-sea breeze circulations, improved predictions of the ground/soil temperature alone are not sufficient. One also needs to improve the representation of temperature gradients across the water-land continuum, resulting in more accurate representation of sea surface temperatures (SSTs). Warm waters in the Gulf of Mexico are a major mesoscale feature influencing local weather through land-sea breezes and precipitation events, particularly during warmer time periods. To realistically simulate meteorological and air quality features over the coastal environments, it is important to represent SSTs over the Gulf of Mexico as accurately as possible.

In the traditional approach for performing meteorological simulations, one normally uses the coarse-resolution SSTs available from the Eta Data Analysis System (EDAS) of the National Center for Environmental Prediction (NCEP) at 40-km resolution in prescribing SSTs over water-covered grid cells in a mesoscale model. However, this leads to a bulk representation of SSTs that could lead to some modeling errors, particularly over the coastal regions such as the Houston-Galveston region. For our purposes, we therefore acquired satellite measurements from NOAA at very high spatial (1 km) and temporal (1 h) resolutions (<http://www.mslabs.noaa.gov/cwatch/>) over the Gulf of Mexico region. These satellite observations were ingested into the MM5 inputs in place of analyzed SSTs obtained at 40-km resolution.

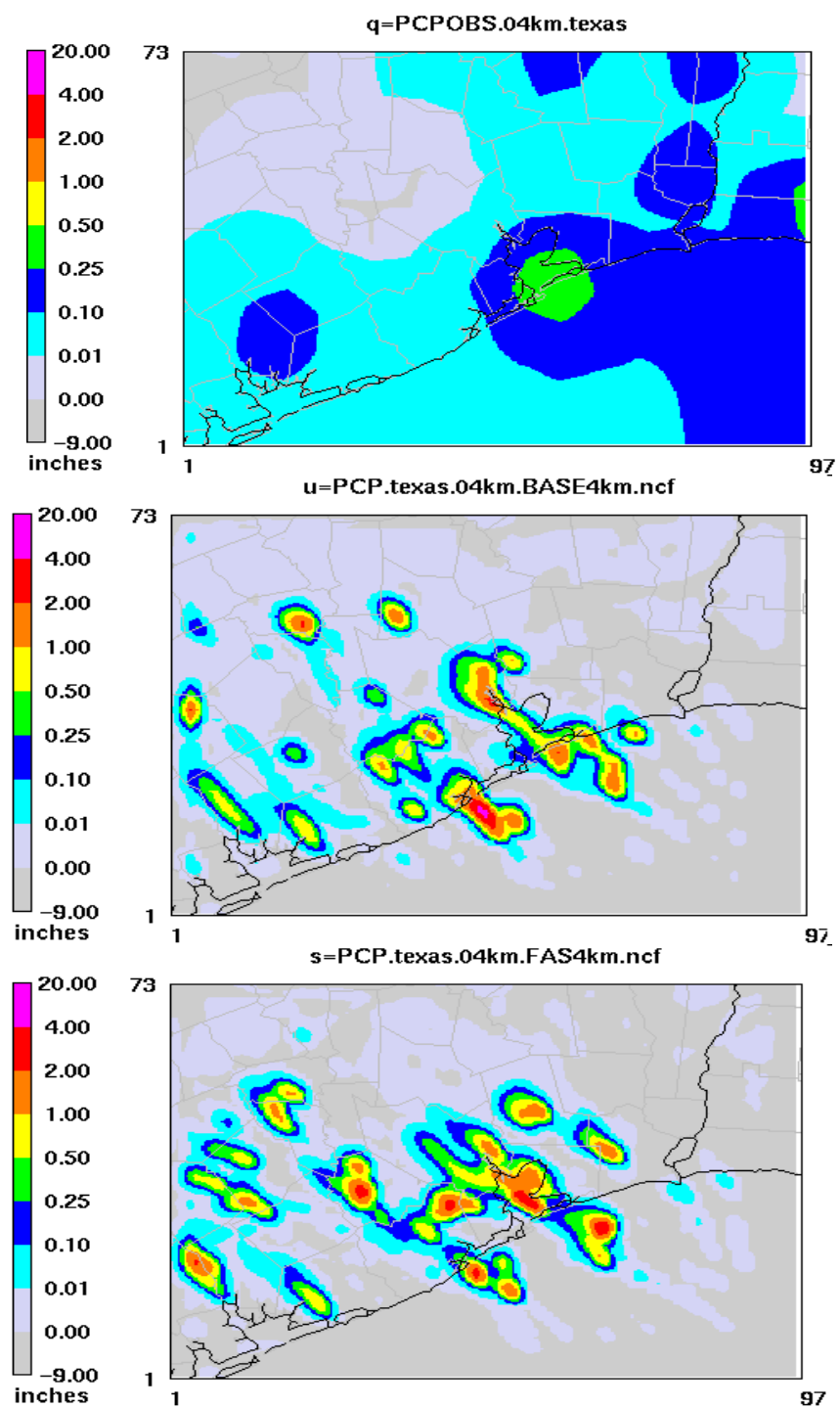


Figure 24a. Accumulated precipitation for the “Obs”, “Base” and “Fasdas” cases, ending at 1200 UTC 24 August 2000 for the 4-km grids.

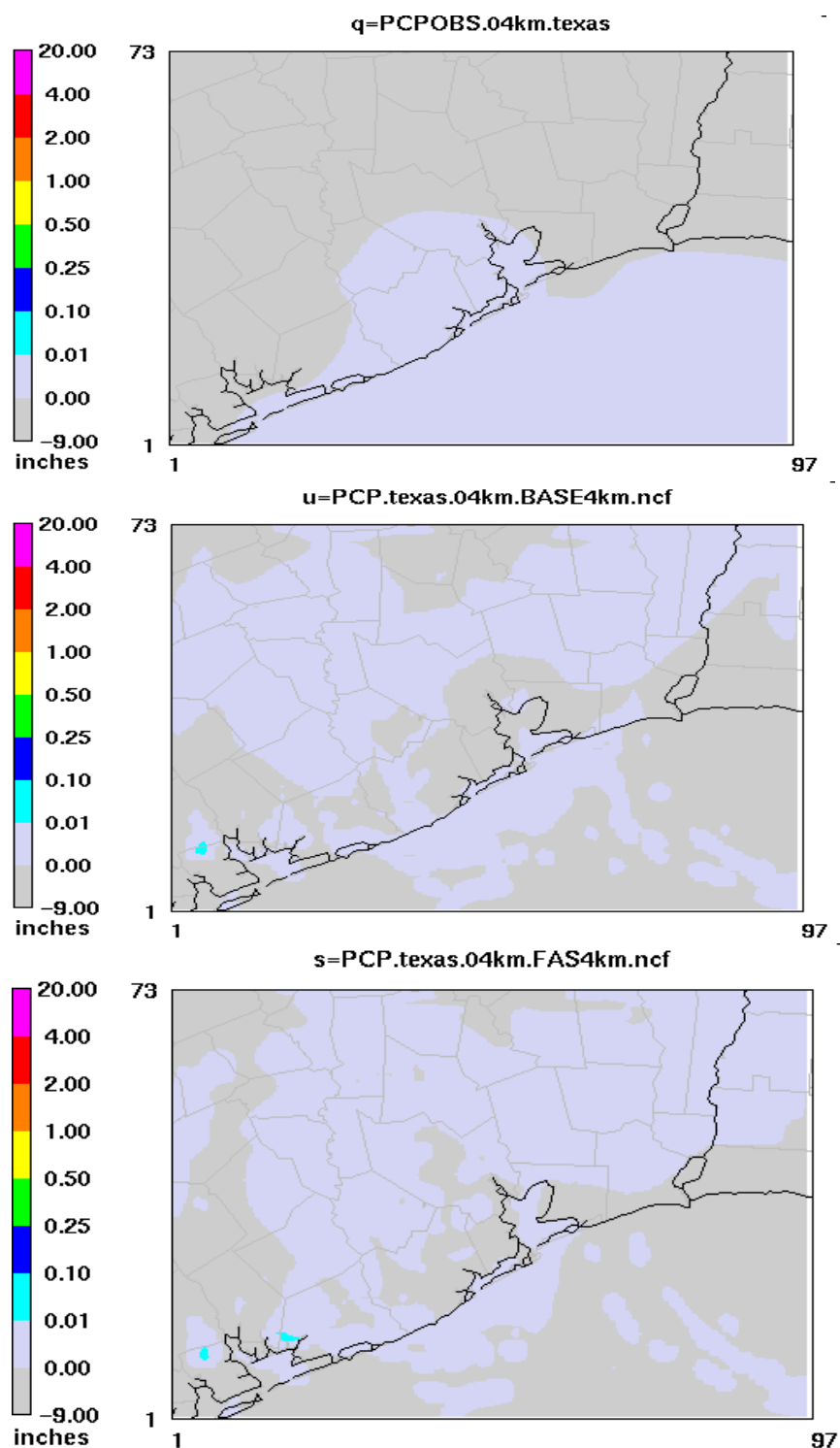


Figure 24b. Accumulated precipitation for the “Obs”, “Base” and “Fasdas” cases, ending at 1200 UTC 28 August 2000 for the 4-km grids.

We acquired remotely sensed SSTs at 4x4-km resolution archived by NOAA for a small region east of the Houston-Galveston area. We then performed some QA/QC procedures to weed out any missing or bad data (cloud pixels) and ingested the remotely sensed SST data into the MM5 preprocessing system for further processing and use in developing initial and lateral boundary meteorological fields for use by the MM5. Since we were able to acquire only partial data for the period of interest, the MM5 model simulations performed for the 36- and 12-km grids used only the traditional SST data (coarse NCEP data). For the 4-km grid (Domain D03 in Figure 1) we performed two MM5 simulations, one using the traditional SST data and the other using the NOAA satellite-derived SSTs. We believe that we may have been the first researchers to ingest satellite-derived SSTs into the MM5 for use in an air quality modeling research.

Figure 25a shows the spatial distribution of SSTs obtained from processing the traditional NCEP analysis, while Figure 25b shows the SST distribution obtained using NOAA's satellite measurements. There is a large difference in the magnitudes and spatial distributions of SST gradients for the period considered in this study. These two differing SST datasets were used to perform the MM5 simulations for the 4-km domain D03 to investigate how using different SSTs affects the model simulations. Some analysis results are presented here. Results obtained from using the analyzed SSTs and satellite-derived SSTs are referred to in the text as "Base" and "Sat," respectively.

Since large differences in the SSTs were present, we used an eastern subregion of the Houston-Galveston domain (highlighted in the Figure 26) for analyzing average properties of different variables simulated by the MM5. The main reason to consider this subregion is that during the daytime easterly winds dominate the general flow pattern where winds from the Gulf seep into the Houston-Galveston region. Thus, use of differing SSTs should affect the mesoscale dynamics and circulation pattern. Figure 27a shows the temporal variation in the area-averaged surface latent heat flux for the subregion for the "Base" and "Sat" cases. The latent heat fluxes are about 100% higher in the "Sat" case than in "Base." Figure 27b shows the temporal variation in the area-averaged depth of the boundary layer. Warmer sea surface temperatures resulted in an increased ABL depth for the "Sat" case. This result will have a moderate to large effect on the modeled concentrations of various gas species because of differences in the depths of the ABL through which these species are diluted by turbulent mixing.

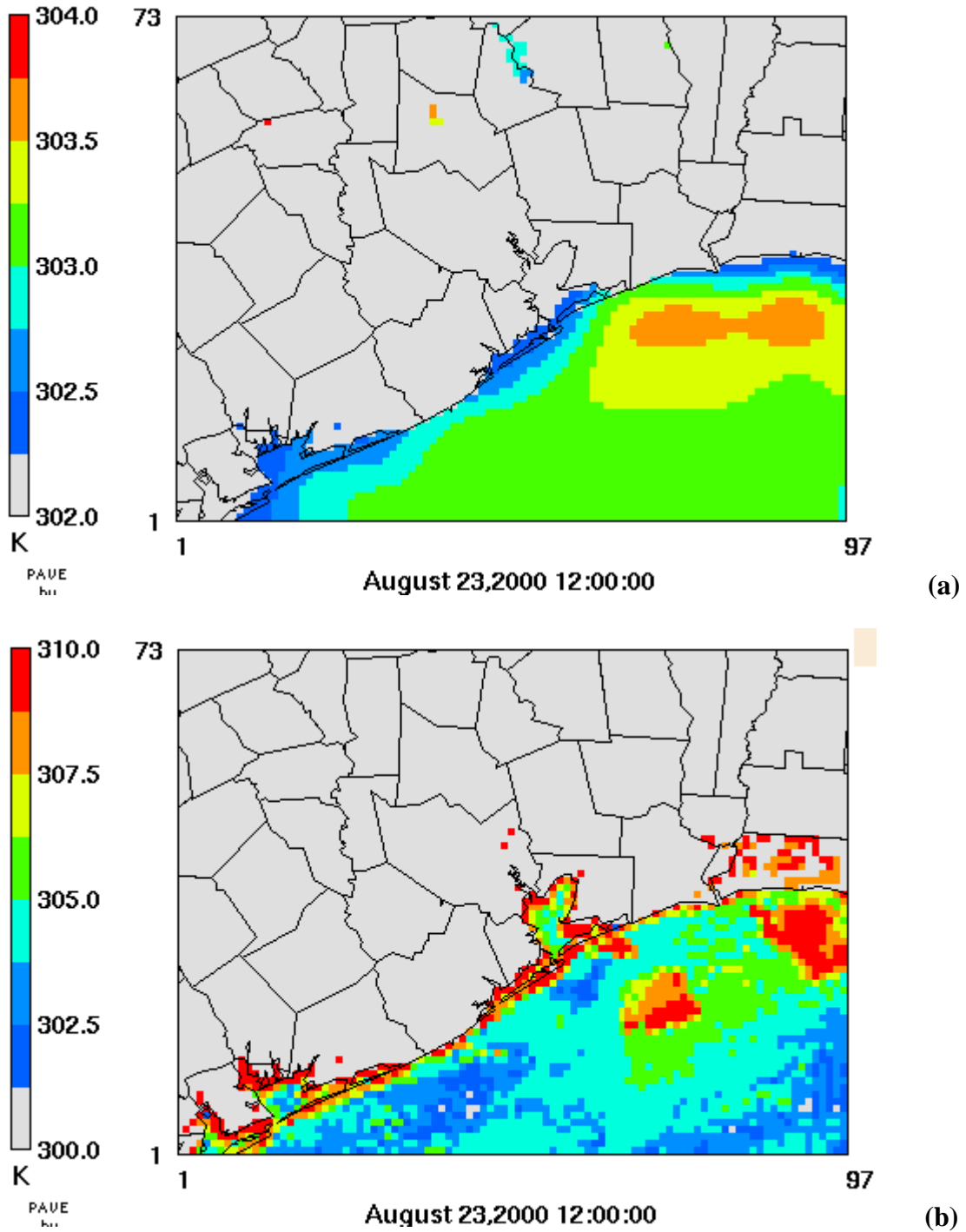


Figure 25. Spatial distribution of sea surface temperatures in domain D03 obtained from (a) the traditional NCEP analysis and (b) NOAA's satellite-derived measurements, at 1200 UTC 23 August 2000. Note the difference in the scale ranges.

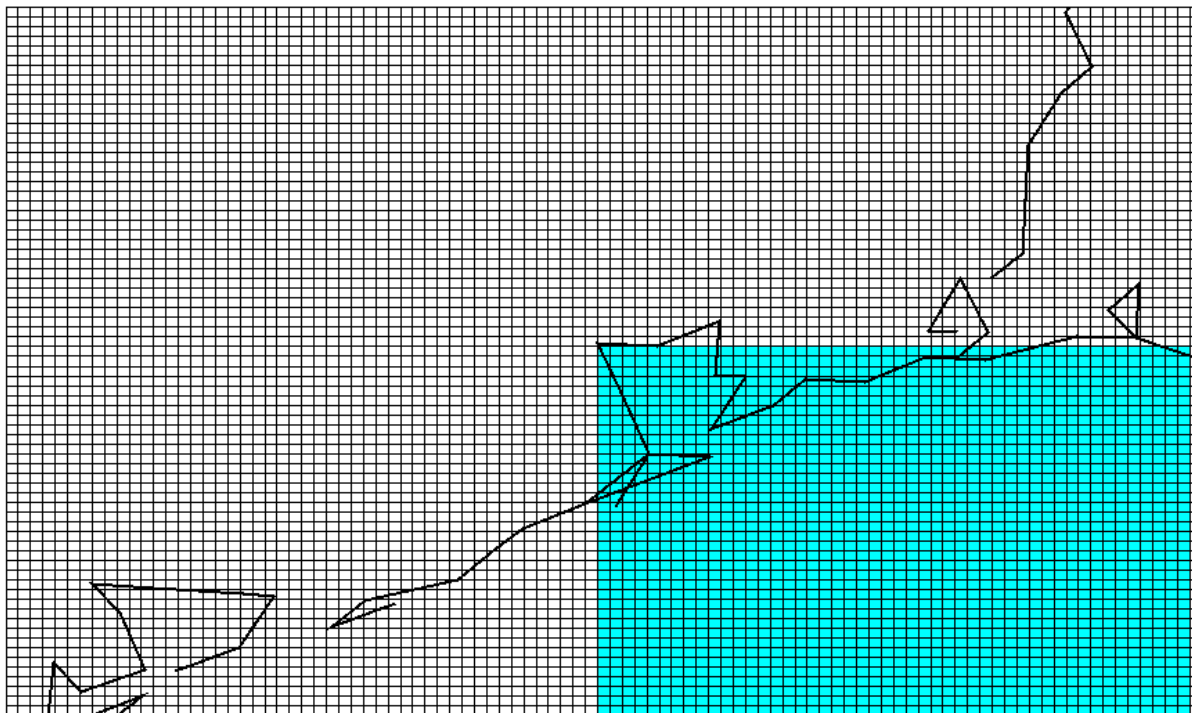
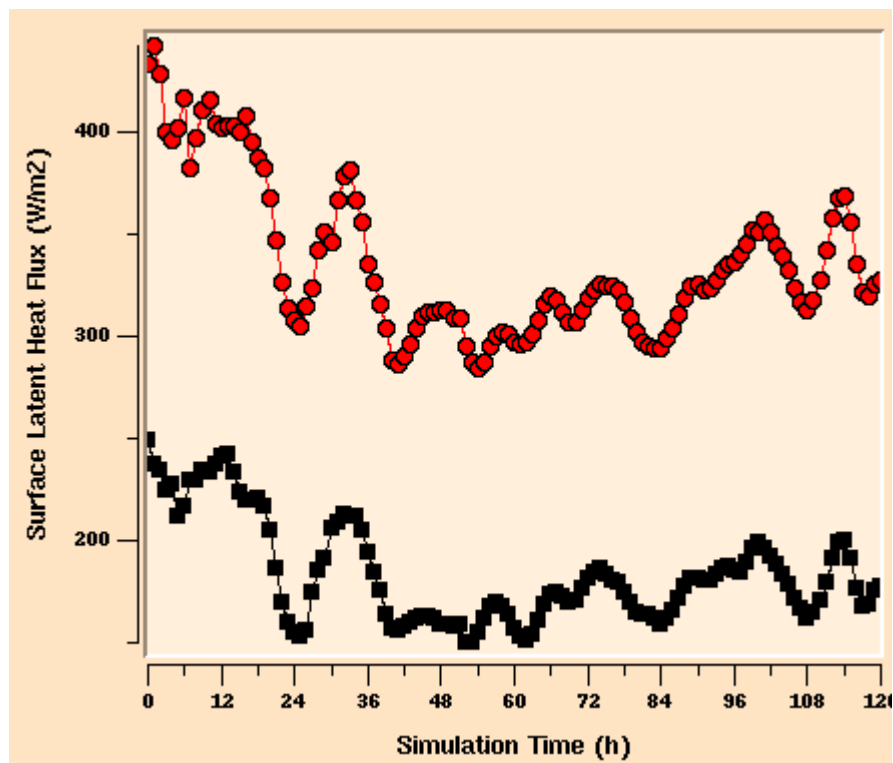
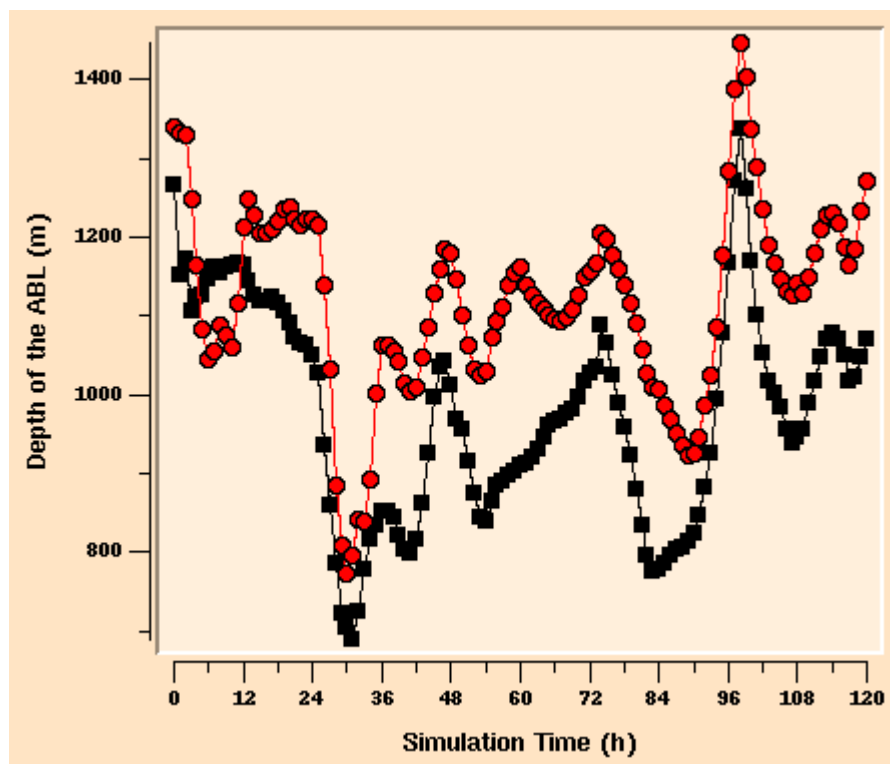


Figure 26. Portion of Gulf of Mexico considered (highlighted grid cells) in developing area-averaged meteorological parameters for analysis and intercomparison.



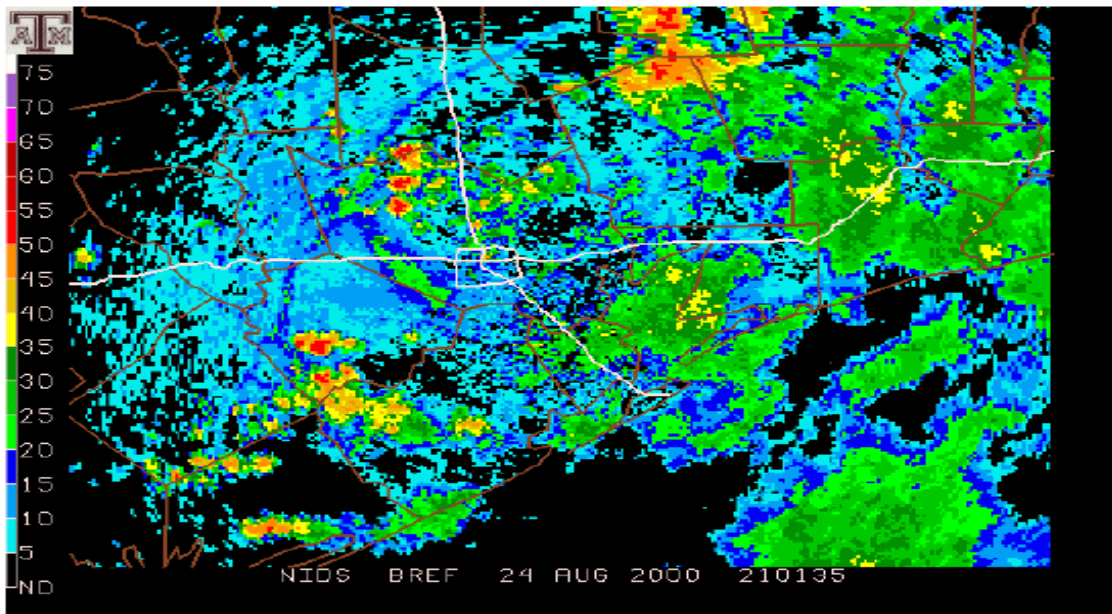
(a)



(b)

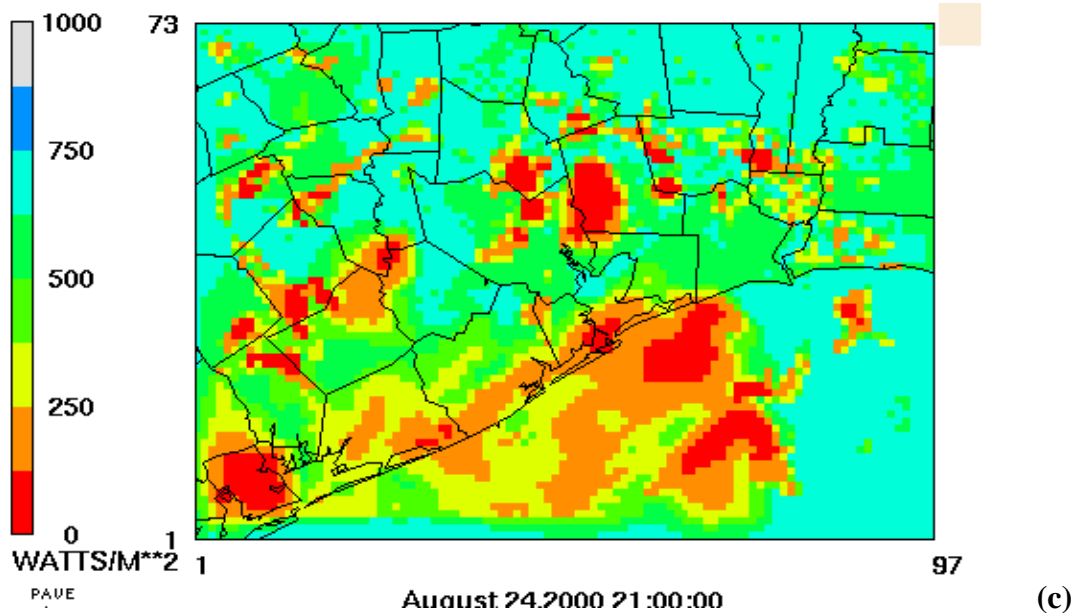
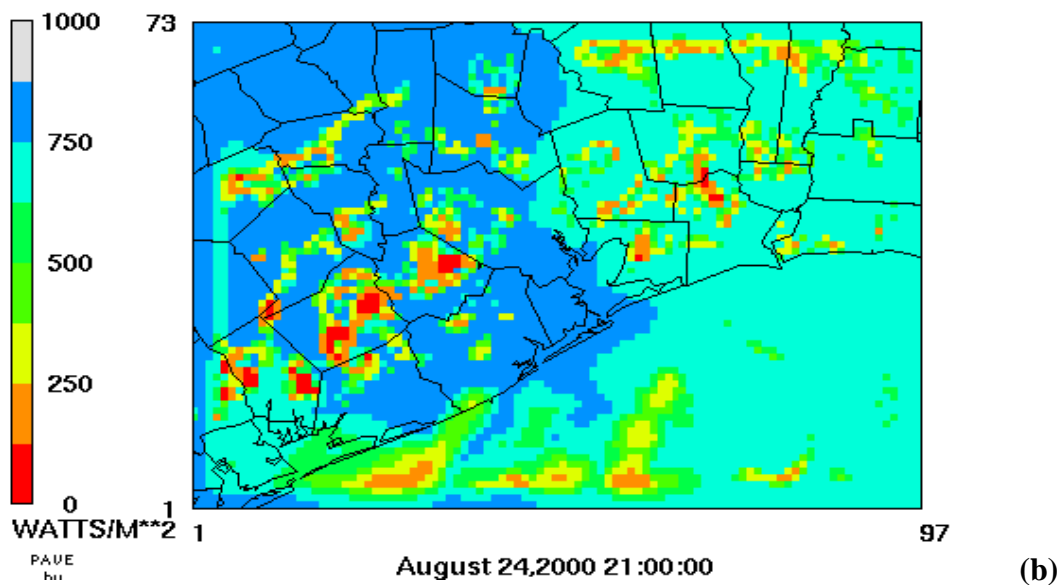
Figure 27. Area-averaged (a) surface latent heat fluxes and (b) depth of the ABL, over the Figure 26 subregion of the Gulf of Mexico. Black: "Base"; Red: "Sat"

Figure 28a shows radar imagery at 2100 UTC 24 August 2000 obtained from the study of Neilson-Gammon (2002); it indicates regions of light (cool colors) and heavy (hot colors) precipitation. Because we used a 4-km resolution, convection and associated precipitation may be sufficiently resolved by the explicit cloud scheme used in the MM5 simulations. We compared the shortwave radiation reaching the ground in the “Base” and “Sat” cases (Figs. 28b and 28c). Once clouds form, they may not lead to precipitation in the model. However, it affects the amount of shortwave radiation reaching the surface. Thus, shortwave radiation reaching the surface can be used as a surrogate for cloud activity. Closer examination of Figs. 28a, 28b, and 28c shows greater similarity between the radar measurements and the “Sat” case, while “Base” has highly underpredicted cloud amounts. Observed precipitation over Galveston Bay and north and east of the Houston-Galveston region is better simulated by the locations of clouds in the “Sat” case. Figures 29a and 29b show the total accumulated precipitation for the hour ending at 2100 UTC 24 August 2000 for the “Base” and “Sat” cases. Qualitative comparison of images in Figs. 28 and 29 suggest that the “Sat” case modeled precipitation far better than the “Base” case did. This demonstrates the necessity of using realistic SSTs in meteorological modeling.

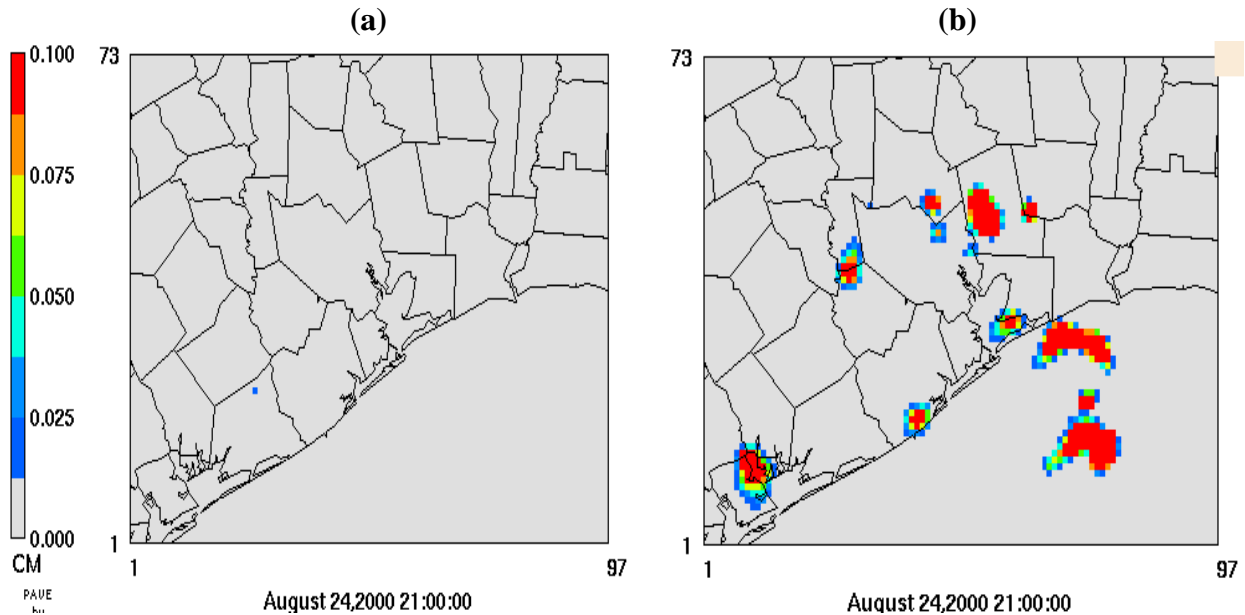


(a)

Figure 28a. Radar imagery of reflectivity showing intensity of precipitation at 2100 UTC 24 August 2000, obtained from a study by Neilson-Gammon (2002).



Figures 28b, 28c. Modeled shortwave radiation reaching the surface (W/m^2) at 2100 UTC 24 August 2000 for the (b) "Base" and (c) "Sat" cases.



Figures 29. Modeled total precipitation (cm/h) for an hour ending at 2100 UTC 24 August 2000 for the (a) “Base” and (b) “Sat” cases.

Using realistic SSTs also significantly affects the modeling of the land-sea breeze; this is clearly evident in the moisture distribution near the surface and aloft. Figures 30a and 30b show the model’s lowest-level moisture and its vector flux on August 25 for the “Base” and “Sat” cases, indicating dramatic effects on the precipitation events present at that time.

Next we intercompare and discuss some of the prognostic analysis results using surface measurements. Figure 31a shows the temporal variation in the averaged 2-m AGL temperature from the measurements (“Obs”) and from the “Base” and “Sat” cases. During the daytime, the maxima are well simulated in “Sat” compared to “Base”, while during the nighttime mixed results are seen for the minima when intercompared with “Obs”. However, analysis of RMSEs (Figure 31b) indicates that daytime simulations with “Sat” are better (lower RMSEs), while during the nighttime the RMSEs in “Base” are relatively lower compared to “Sat”. Analysis of temporal variation of near-surface water vapor mixing ratio and its RMSEs (Figures 32a and 32b) indicate again somewhat similar results, without any clear indication of which case is the better. Analyses of vertical soundings for temperature, dew point temperature, and horizontal wind vectors (Figures 33a and 33b) also indicate that the “Base” and “Sat” cases do equally well when compared to observations. Finally, we consider the 24-h accumulated precipitation ending at 1200 UTC for 24 August and 28 August (Figures 34a and 34b, respectively). In the “Sat” case it appears that the accumulated precipitation is higher in magnitude and is in closer agreement with “Obs”, particularly over the Houston Bay area. With the exception of locally produced thunderstorms in “Base” and “Sat”, these results are comparable to each other.

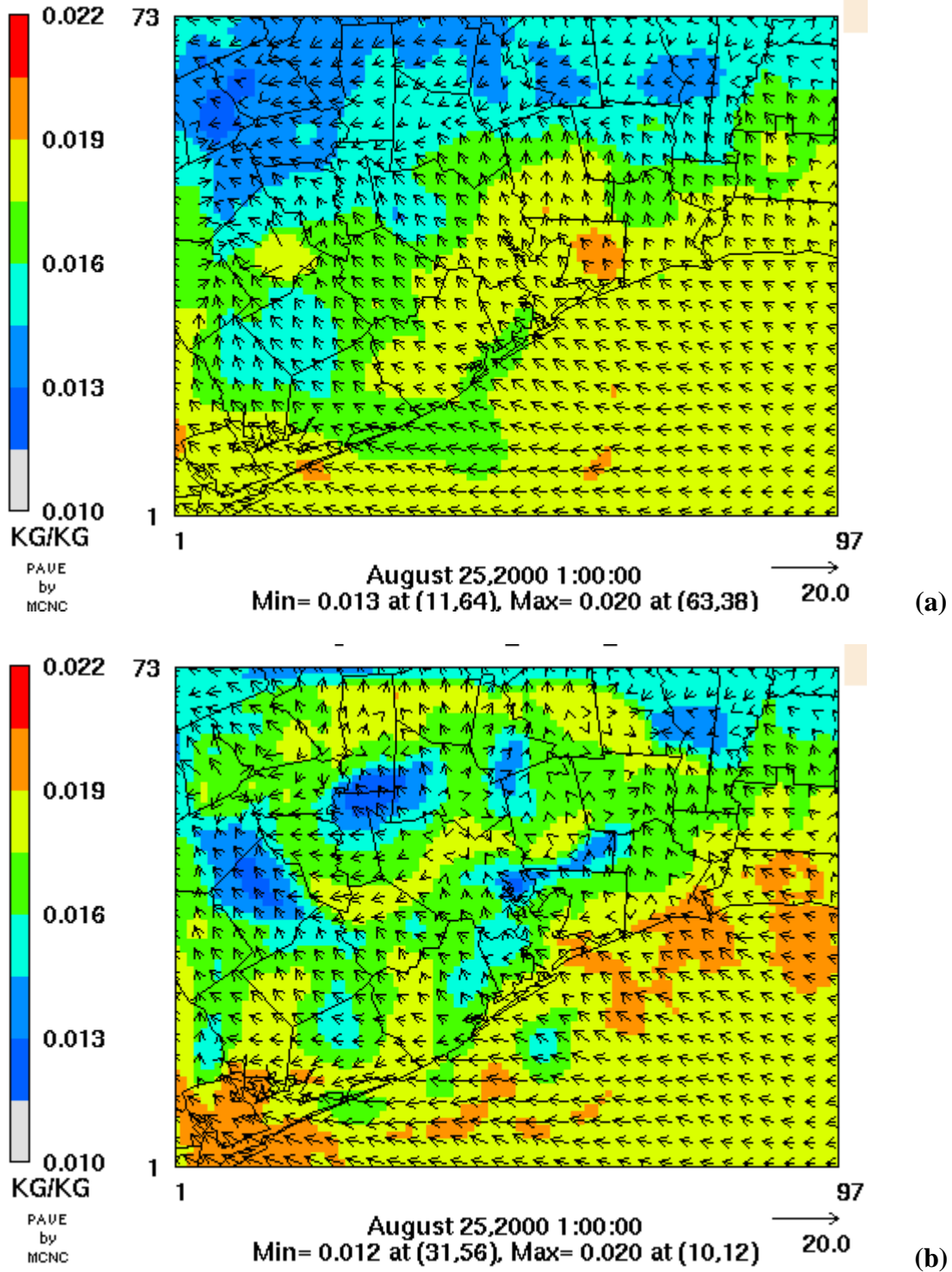


Figure 30. Horizontal distribution of water vapor mixing ratio (kg/kg) and its vector fluxes (m/s kg/kg) at 0100 UTC 25 August 2000 for the (a) “Base” and (b) “Sat” cases.

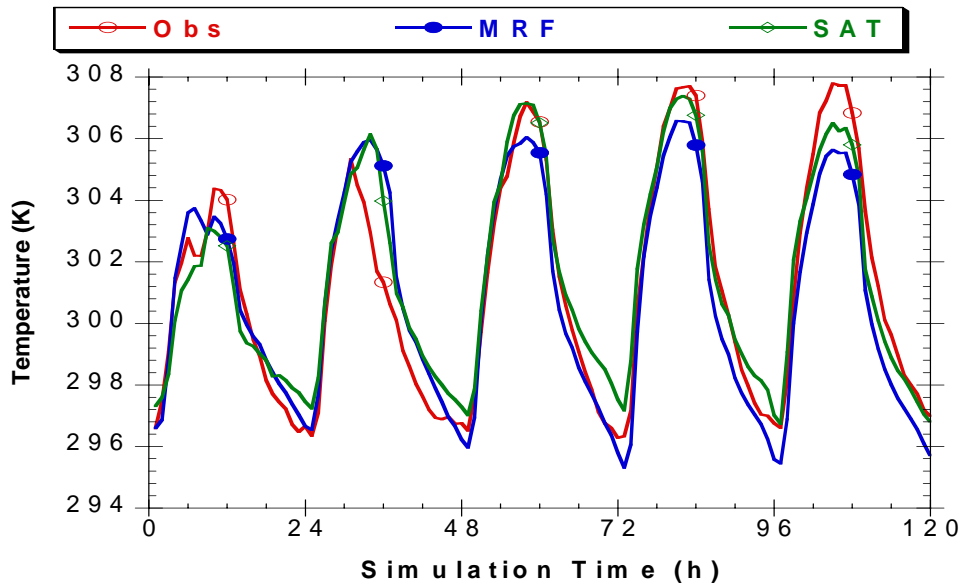


Figure 31a. Temporal variation of near-surface air temperature averaged over all of the measurements and corresponding modeled values, starting at 1200 UTC 23 August 2000 for the “Base” and “Sat” cases for the 4-km grids.

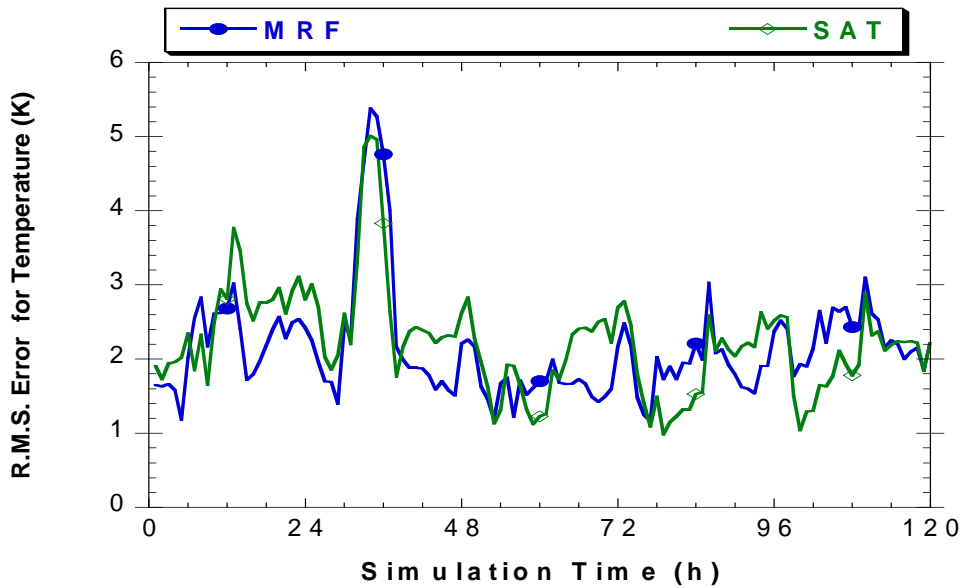


Figure 31b. Temporal variation of near-surface air temperature RMSEs for the “Base” and “Sat” cases using the 4-km grids starting at 1200 UTC 23 August 2000 .

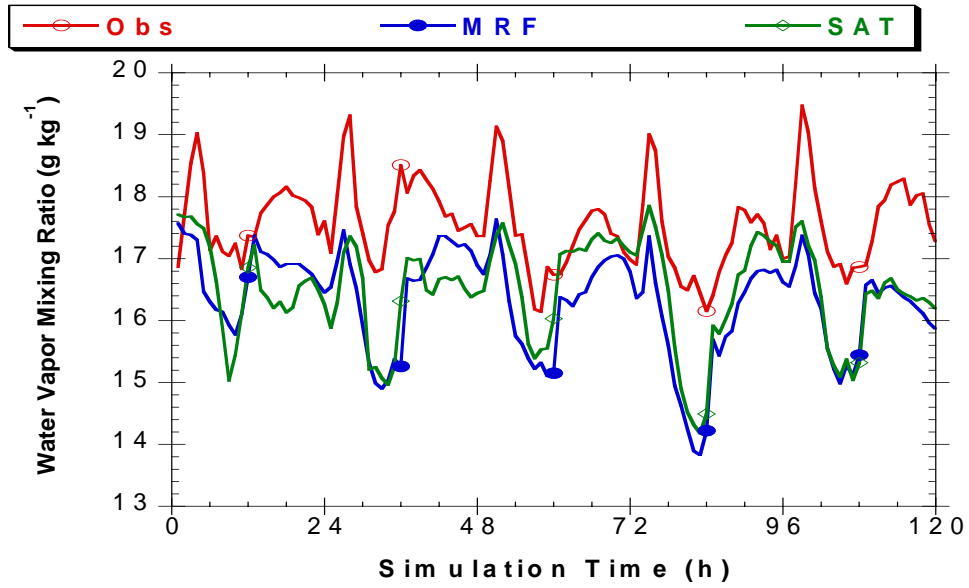


Figure 32a. Temporal variation of averaged near-surface water vapor mixing ratio for the “Base” and “Base” cases, starting at 1200 UTC 23 August 2000.

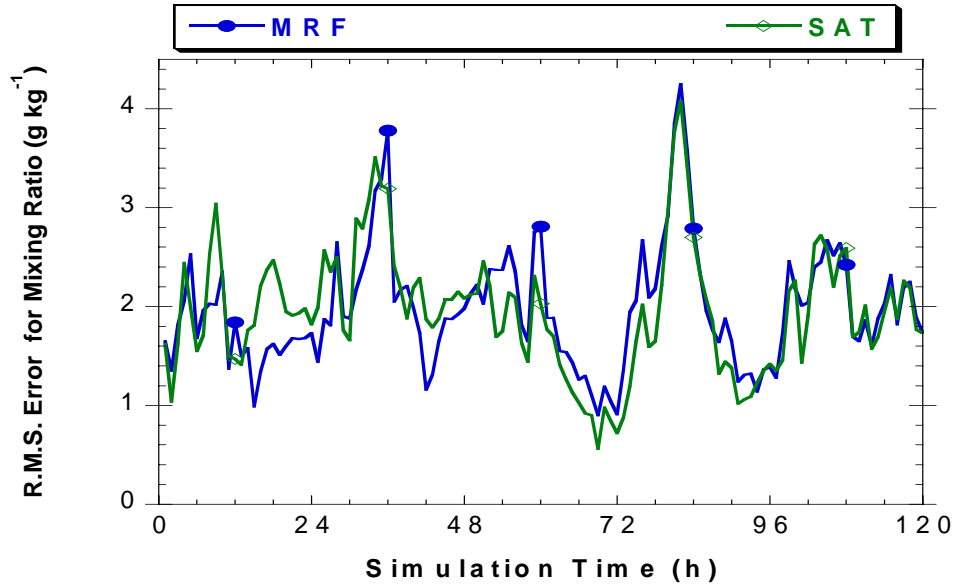


Figure 32b. Temporal variation of near-surface air mixing ratio RMSEs for the “Base” and “Sat” cases using the 4-km grids starting at 1200 UTC 23 August 2000.

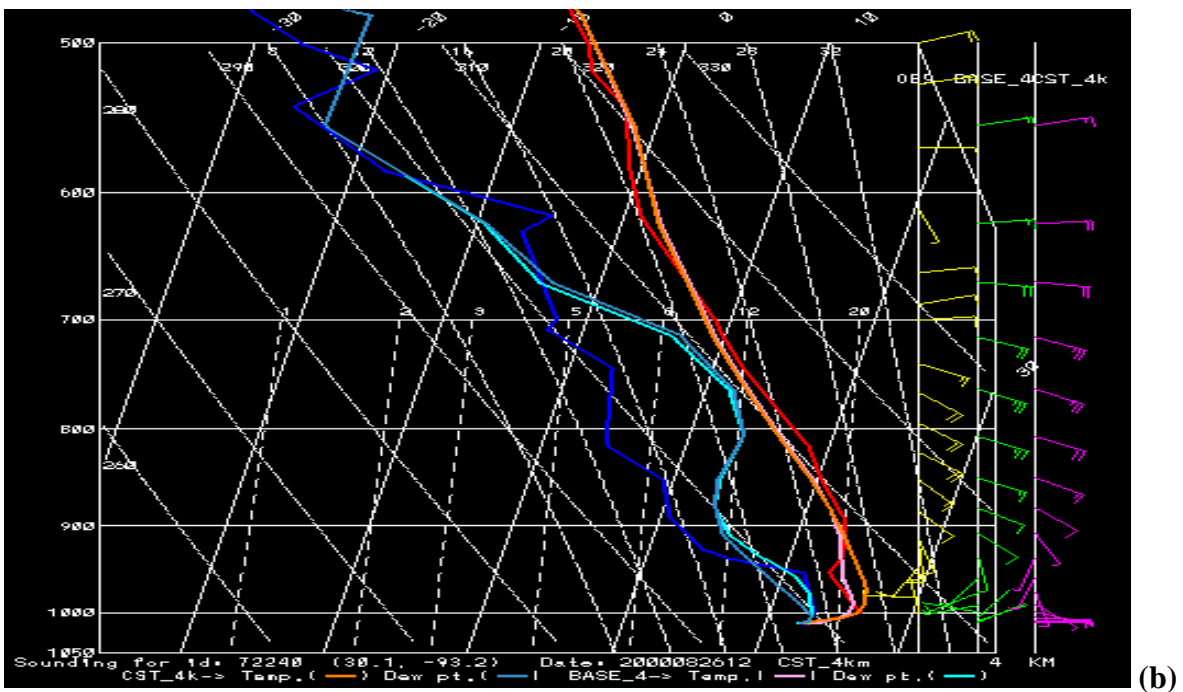
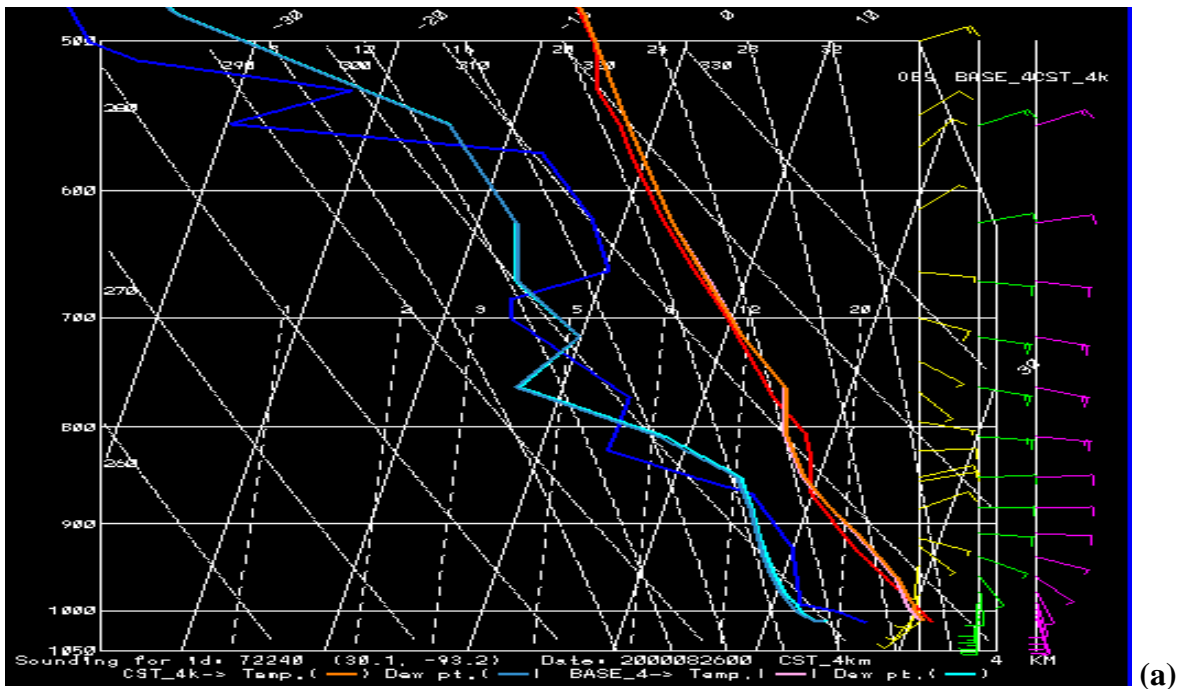


Figure 33. Vertical variation of Temperature, dew point temperature, and horizontal wind vectors for “Obs”, “Base”, and “Sat” at (a) 0000 UTC and (b) 1200 UTC 26 August 2000 for a coastal location in southwest Louisiana.

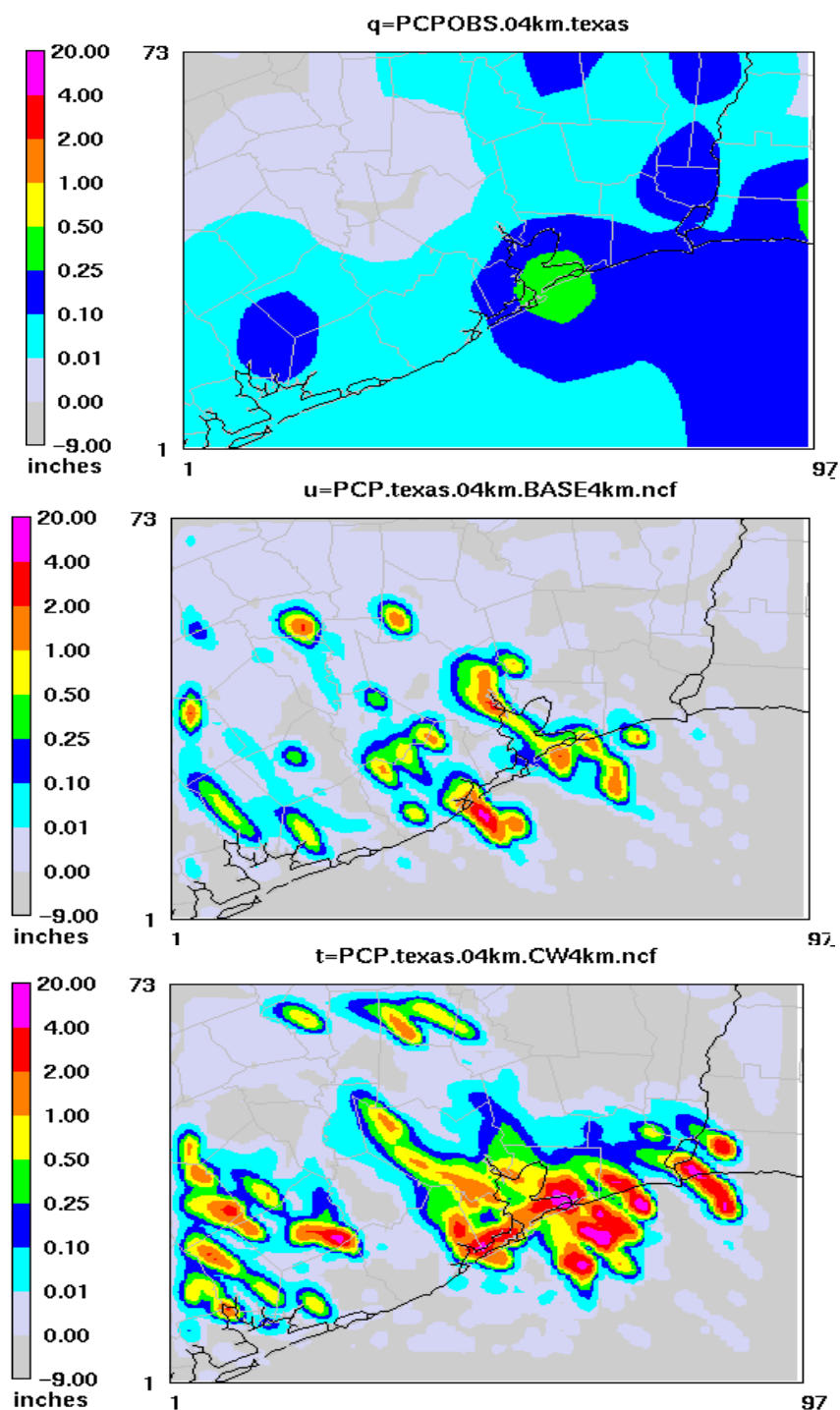


Figure 34a. Accumulated precipitation for the “Obs”, “Base” and “Sat” cases, ending at 1200 UTC 24 August 2000 for the 4-km grids.

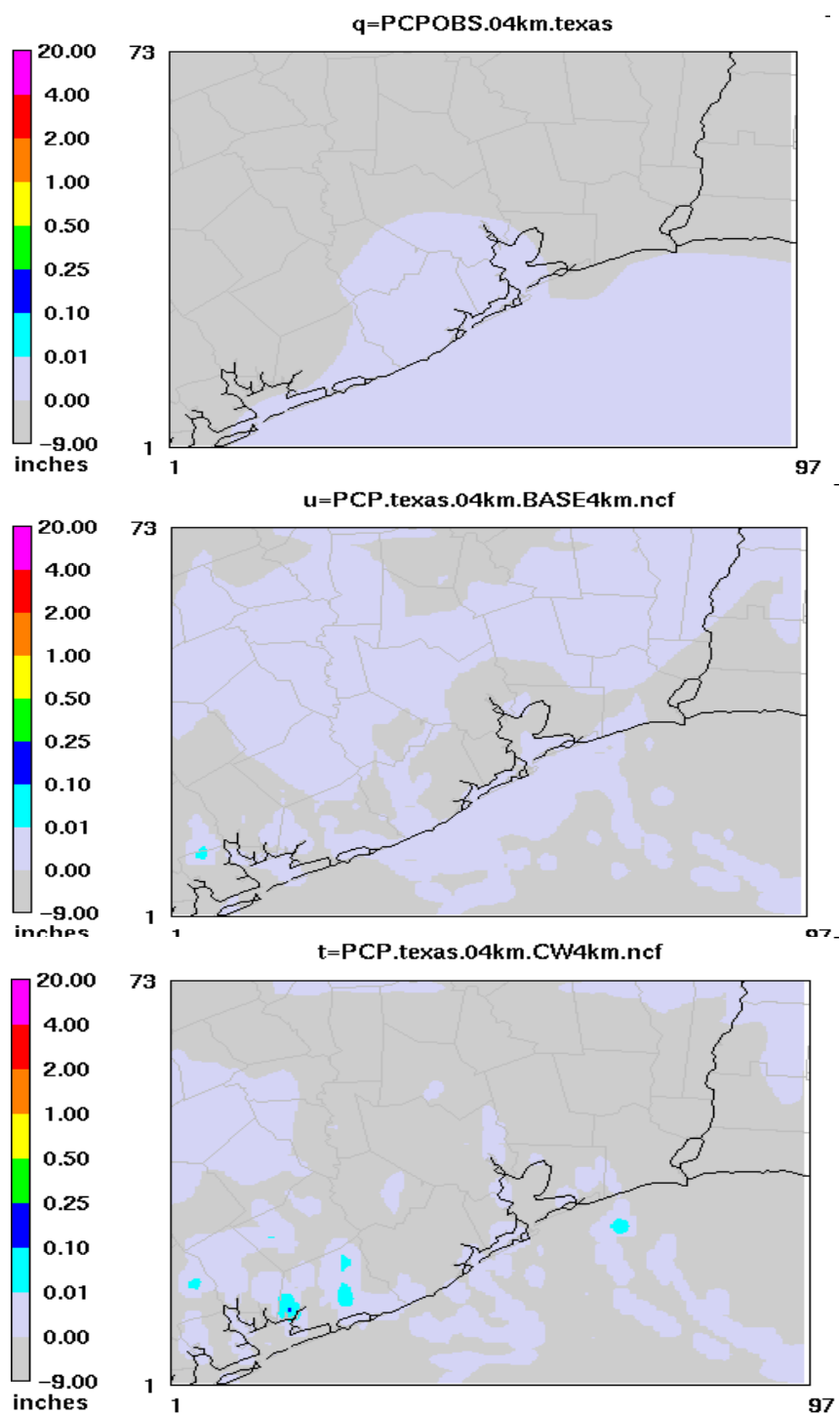


Figure 34b. Accumulated precipitation for the “Obs”, “Base” and “Sat” cases, ending at 1200 UTC 28 August 2000 for the 4-km grids.

One of the main hindrances in analyzing 4-km grid simulations is the lack of statistically significant numbers of measurements that would allow a stronger conclusion regarding which case is performing better compared to the other. The diagnostic analysis indicated the presence of larger differences between the “Base” and “Sat” cases. Considering all of these results, we believe that, in general, the “Sat” case seemed to perform better than the “Base” case, while noting the point that differences between the simulations are very small for the parameters for which measurements are available.

2.4 Task 6: Enhance Representation of Cloud Processes in the MAQSIP-VGR

Although Task 6, “Enhance Representation of Cloud Processes in the MAQSIP-VGR” is not next numerically according to the project task list given on page 1, we discuss it before addressing Tasks 4 and 5 because we feel that order of discussion enables easier comprehension of the report by the reader. Task 6 relates to model development activities, which have also been the topic of Tasks 2 and 3, rather than to the details of the case studies, which are the subject of Tasks 4, 5, 7, and 8.

There are four primary processes by which clouds modify atmospheric chemical composition and distribution:

- (1) subgrid-scale vertical turbulent redistribution of mass;
- (2) aqueous chemical effects, including dissolution, dissociation, and kinetic reactions;
- (3) rainout and wet removal due to precipitation; and
- (4) modification of solar actinic flux and hence the rate of photolytic reactions.

The original representation of cloud effects in the MAQSIP-VGR accounted only for attenuation of photolysis rates due to the presence of clouds and was based on the cloud fields specified by the driving meteorological fields. We used a 1-D model to test the extension of model representation of cloud processes to include the other effects discussed above by adapting the mesoscale and urban-scale cloud modules available in the regular grid version of the MAQSIP model. This included representation of shallow convection, deep convection, resolved-scale clouds, and subgrid-scale layer clouds (McHenry and Binkowski, 1996; McHenry et al., 1996).

We analyzed the results of a 1-D cloud model to examine the effect of the fine-resolution configuration of the variable-grid model on the cloud processes, which in turn affect pollutant formation and deposition.

The testing of this cloud scheme implementation for the MAQSIP-VGR involved a series of 1-D column model tests in which an initially specified vertical pollutant mixing ratio distribution was subjected to cloud processes (mixing, scavenging, and deposition). In these tests we created input data files for the 1-D model by extracting (from prior 3-D data sets) vertical profiles of relevant meteorological data for a single grid cell at which precipitation occurred. The 1-D column model was run such that all physical and chemical processes except clouds were switched off. A variety of tests were conducted that constituted consistency checking of the code. Pollutant vertical profiles were examined before and after they were subjected to these cloud processes to determine the correctness of the implementation. The tests included

- (1) verification that an initially specified “well-mixed” pollutant field was retained after it was subjected to cloud mixing in the absence of any scavenging and wet deposition;
- (2) verification that the column total mass of a pollutant did not change with time after it was subjected to cloud mixing; and
- (3) verification that vertical profiles of water-soluble pollutants were modified only in “cloudy” layers, when cloud mixing was shut off.

Figure 35 shows example analyses of the consistency checking simulations. Figure 35a presents variations in vertical distributions of O₃ for a case in which only cloud mixing is considered. The changes in vertical profiles are consistent with the existence of cloudy layers during the simulation. We also found that for a species with an initially specified uniform mixing ratio, the “well-mixed” pollutant profile was conserved through the 24 hours of the simulation (not shown). Figure 35b presents the variation in total column O₃ mass relative to the initial mass through the 24 hours of the simulation. The changes in total column mass for this time period were negligible.

We implemented this cloud mixing scheme into the MAQSIP-VGR. We extended the representation of cloud effects in the model by developing and adapting modules to represent the effects of deep convection and resolved-scale clouds on simulated pollutant distributions. Modules for these cloud processes used in the regular-grid version of the MAQSIP were adapted for inclusion in the MAQSIP-VGR. The convective cloud parameterization is based on the diagnostic cloud module used previously in the Regional Acid Deposition Model (Dennis et al., 1993; Chang et al., 1987; Walcek and Taylor, 1986); these clouds can be either precipitating or nonprecipitating. The module determines whether precipitating or nonprecipitating clouds exist over a grid cell based on input precipitation data derived from the MM5 convective cloud module. Based on the Community Multiscale Air Quality (CMAQ) (Byun and Ching, 1999) model implementation of this scheme, we used only convective precipitation amounts from the MM5 to drive the precipitating cloud module; nonconvective amounts were used in the resolved cloud module (Roselle and Binkowski, 1999). Details on the convective cloud parameterization can be found in the references cited above.

The resolvable-scale cloud scheme was used at all grid resolutions in order to model the scavenging (and aqueous-phase chemistry, in future versions) of pollutant species in the nonconvective layer and resolved clouds. The implementation assumed the presence of resolvable-scale clouds when condensed water exceeds 0.05 g/kg in a given model grid cell, which represents about one-tenth of the amount needed for autoconversion to precipitation. Scavenging was carried out for all condensate concentrations exceeding this value, and wet removal was computed for times when precipitation fell. Wet removal was modulated by rainout below cloud using an approach similar to that for deep convection.

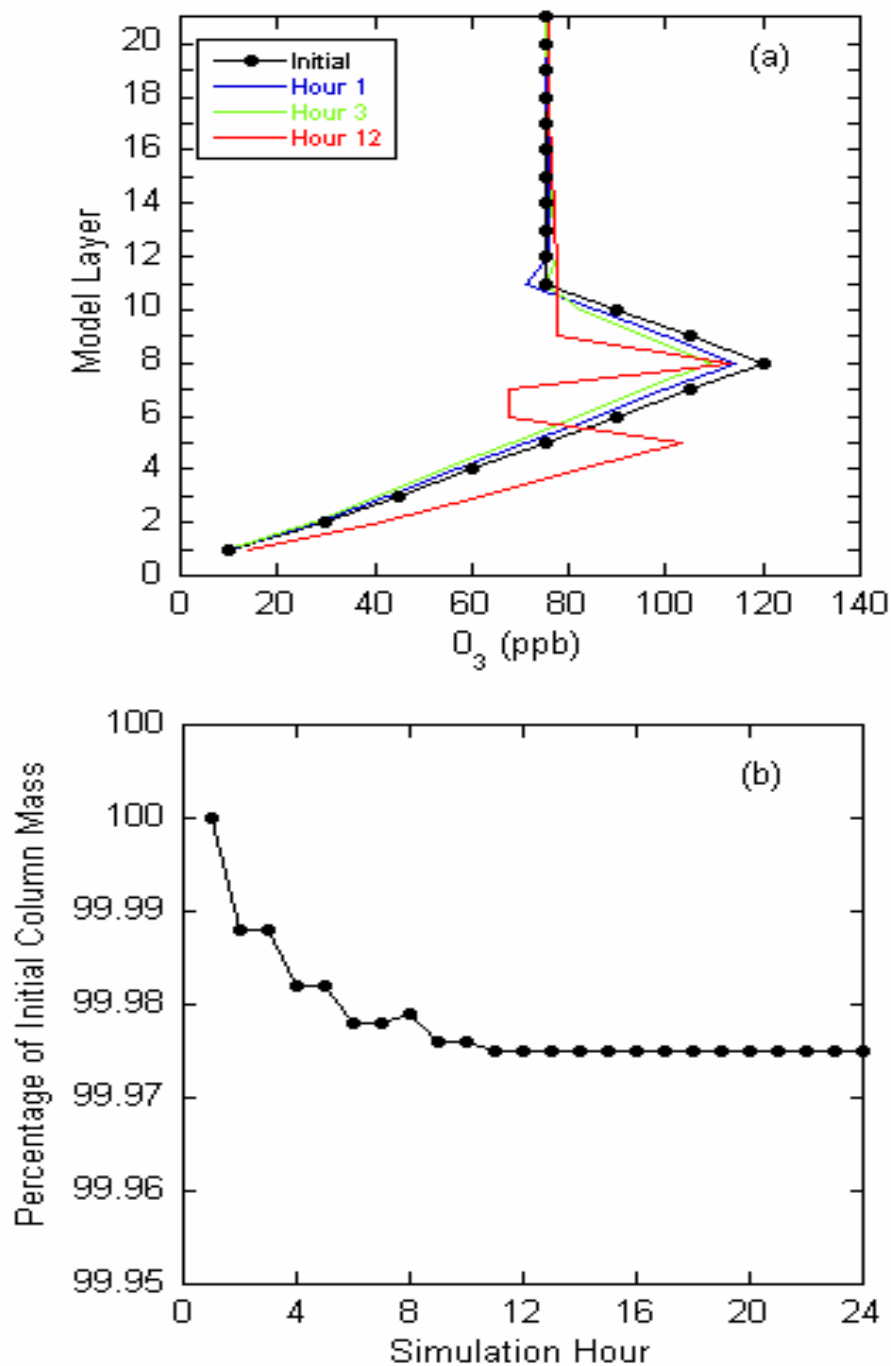


Figure 35. Example results from testing the 1-D cloud module for a case in which an initially specified concentration profile was subjected to cloud mixing. (a) Variation in O_3 vertical profiles at different times during the simulation; (b) change in column total O_3 mass relative to the initial mass.

2.5 Task 4: Simulate Mesoscale Circulations Using the MM5

The objective of this task was to prepare the meteorological inputs for the MAQSIP-VGR. To do this, we created a regional modeling domain covering parts of the central and eastern United States, with a stretch from a 4-km-resolution domain over the Houston-Galveston region to a 36-km grid resolution at the boundaries of the regional domain (the stretch is discussed further in Section 2.7). Figure 36 shows the 36-km grid (regular grid) map of the regional modeling domain (Figure 36a) and the overlay of the variable grid on the 36-km grid covering the same domain (Figure 36b)

The analyses described above (Tasks 2, 3, and 6) documented the rigorous development and evaluation activities of the MM5 and MAQSIP-VGR. We reconfigured the MM5 using the combination of schemes/methods that produced the best representation of atmospheric circulations in various domains. The configured MM5 (with recommended schemes) was then used to prepare the meteorological inputs for the MAQSIP-VGR (and SMOKE-VGR). This included two steps. In the first we ran the MM5 on a regular grid (36 km), while in the second we used the 36-km meteorological simulations to prepare the variable-grid-resolution meteorology. Meteorological parameters were interpolated to the variable grid locations corresponding to the two cases being analyzed: the Houston-Galveston and the southern Louisiana cases, discussed earlier in this report.

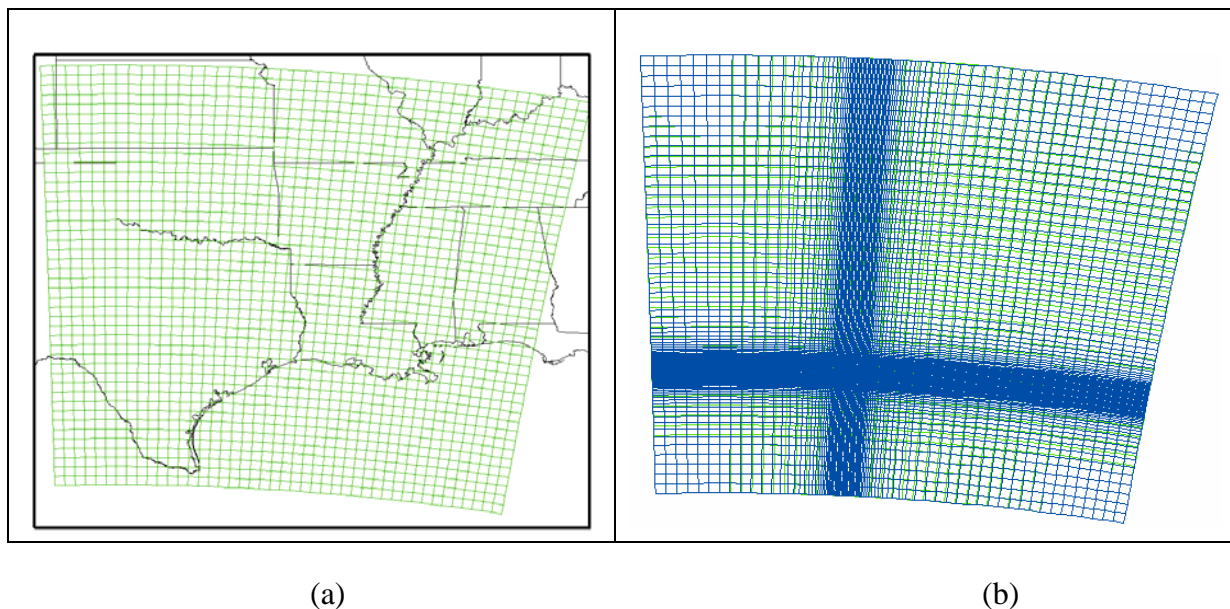


Figure 36. The modeling domain for the August 2000 episode simulations (a) the 36-km grid resolution and (b) variable grid resolution overlaying the 36-km grid resolution; the Houston-Galveston 4-km domain is at the core of the blue shades.

Following the completion and analysis of the meteorological simulations for the 10-day summer episode (August 23 through September 2, 2000) over the regional modeling domain that included the Houston-Galveston and the southern Louisiana Gulf domains, we then prepared the meteorological variable-grid inputs for the same domain and episode.

Figure 37 shows a flow diagram of the variable-grid modeling components. MM5 simulations using a uniform grid provide the file MMOUT, which includes the meteorological simulations for specific episodes. The meteorological outputs are processed through the Meteorology-Chemistry Interface Processor (MCIP) for the same uniform grids. The variable-grid horizontal grid structure is introduced through the grid definition file (“S-Grid” in Figure 37), which provides grid information used to allocate all data onto the variable grid, to process emissions through the SMOKE-VGR, and to process chemistry through the MAQSIP-VGR. Figure 38 shows the S-Grid (variable grid meteorological inputs) for surface air temperature for the Houston Galveston case on August 24, 2000.

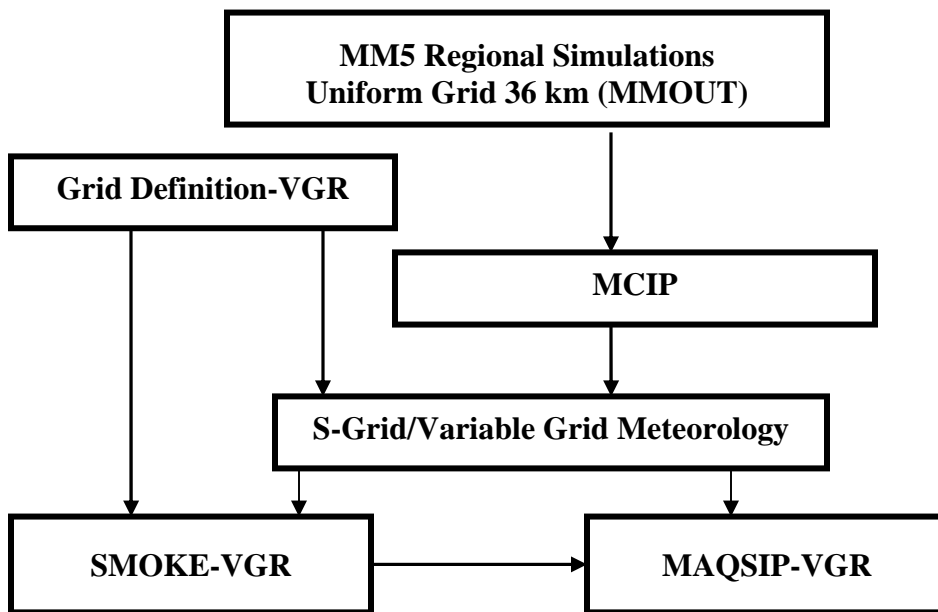


Figure 37. Flow diagram of the variable-grid modeling components.

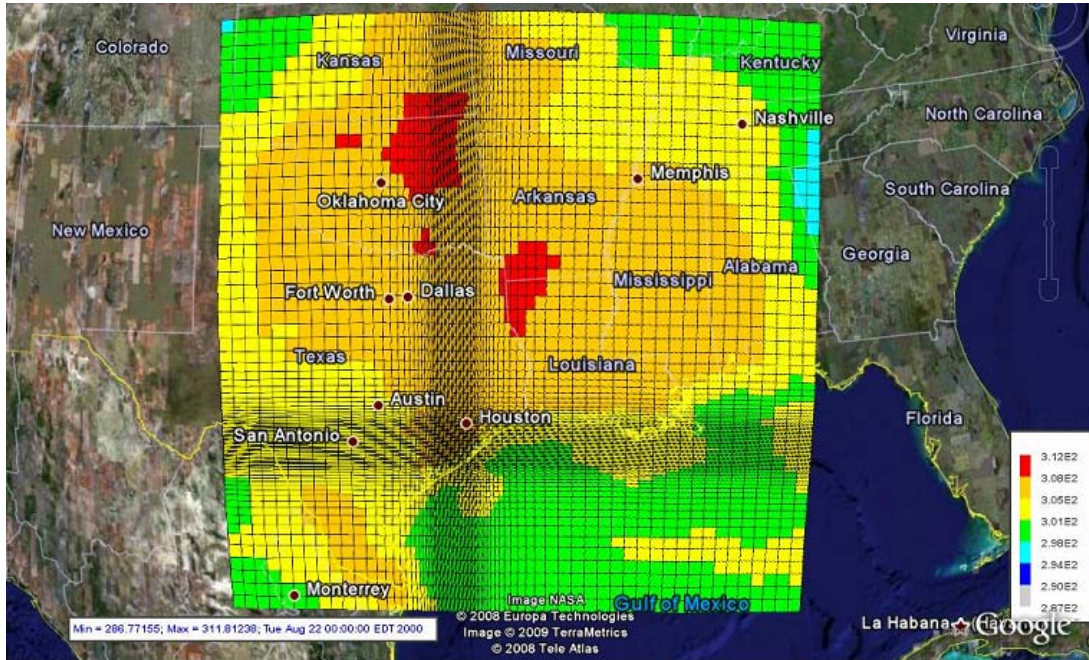


Figure 38. Variable grid surface air temperature simulated by the MM5 model for August 24, 2000 at 0000 EDT

2.6 Task 5: Develop Emission Estimates

The latest emissions inventories available from EPA were used to create input emissions for the Houston and southern Louisiana case studies. The inventories were processed through the SMOKE-VGR system (described below) to create emissions inputs for the MAQSIP-VGR. The processed emissions were quality assured for correctness and accuracy, using various QA tools we have developed over the years; for example, we compared “before” and “after” emissions totals against inventory data, and we examined temporal profiles to check their correctness.

We created SMOKE-VGR, a variable-grid emissions processor, by adapting various components of SMOKE to accommodate the varying horizontal resolution of the MAQSIP-VGR grids. The work involved in developing SMOKE-VGR is discussed below.

For *point-source* processing, SMOKE needs to assign each inventory source to a grid cell. Sources have latitude and longitude coordinates, so with a regular grid, SMOKE can simply calculate the appropriate grid cell based on the grid definition (grid starting point, grid projection, grid cell size, and number of rows and columns). For the variable grid, the grid definition is provided in the GRIDDOT2D file, which contains latitude-longitude coordinates for all the corners of every grid cell. For each source, SMOKE-VGR loops through the variable grid cells and uses these coordinates to place the point source into the appropriate cell.

Point-source processing also uses meteorology data to compute plume rise information for the point sources. The plume rise information is used to distribute the emissions into the various

model layers. Since the structure of the variable grid matches a regular grid in that the number of rows and columns does not change throughout the grid, changes to SMOKE to handle variable grid meteorology data were minimal.

Area- and nonroad-source processing starts with county-level emissions data. SMOKE uses spatial surrogates to assign fractions of the county-level data to grid cells. Different spatial surrogates (such as population or housing) are used for different source types. Since the surrogates are reported only by grid row and column, the details of the variable grid are hidden from SMOKE. As with the meteorology data, minimal changes were needed to support the variable grid: a special header was used on the surrogates file to indicate that the data are for a variable grid.

Mobile sources can be handled in two different ways in SMOKE. In one processing option, the inventory contains vehicle miles traveled (VMT) data for different road types within each county. These data are then fed to the MOBILE6 emissions model along with meteorological information (such as temperature and relative humidity) to calculate actual emissions. A second approach is to provide inventories that already contain the emissions data (calculated outside of SMOKE); this approach is much simpler and follows the same processing path as area and nonroad sources. In SMOKE-VGR, we followed the second path (starting with precalculated emissions data).

Another area in which SMOKE-VGR uses variable-grid land use data that are generated outside the model is *biogenic emissions* processing. For biogenic emissions, SMOKE starts with gridded land-use data that report the fractions of different land use types in each grid cell. SMOKE then uses emissions factors for each land use type to calculate emissions. Future plans involve enhancing SMOKE-VGR to handle gridded land use data for a variable grid and to take into account the varying grid cell sizes when normalizing land use to use with the emission factors.

Once we developed SMOKE-VGR, we tested it using sample data to confirm that the processing was working correctly. We first processed the sample data with SMOKE-VGR using a regular grid and compared the results to the sample results provided with SMOKE. We then reprocessed the same data with SMOKE as variable-grid data (e.g., changing the headers on the spatial surrogates, providing the GRIDDOT2D file for the regular grid) to test the variable-grid handling. The results generated matched the regular grid results.

To model emissions for the southern U.S. region for the August 2000 episode, we used data from EPA's Emissions Modeling Clearinghouse (EMCH). The emissions inventories we used were 2001 data used by EPA for their Clean Air Interstate Rule (CAIR) modeling. These inventories contained data for the following sectors:

- a. Integrated Planning Model (IPM) sector: Point-source facilities that were matched to facilities in the NEEDS 2003 database
- b. Non-IPM sector: All point sources not in either the IPM sector nor in the "point fugitive dust" sector
- c. Point fugitive dust sector: Point sources with source category codes (SCCs) in the list at http://www.epa.gov/ttn/chief/emch/invent/fugitive_dust_sccs.xls

- d. Fire sector: Wildfires, prescribed burning fires, agricultural fires, and open burning (area sources)
- e. Agricultural sector: 2002 NH₃ emissions from livestock and fertilizer application
- f. Area fugitive dust sector: Stationary area sources with SCCs in the list at http://www.epa.gov/ttn/chief/emch/invent/fugitive_dust_sccs.xls
- g. “Other” area sector: Nonpoint (stationary area) sources not in the fire, agricultural, or area fugitive dust sectors and refueling emissions
- h. Nonroad: Nonroad mobile sources from the NONROAD 2004 model via the National Mobile Inventory Model (NMIM) and from commercial marine, airport, and locomotive sources
- i. On-road: On-road mobile sources from the MOBILE6 model via NMIM (not including refueling emissions)

Most of the ancillary SMOKE files were also from EPA’s CAIR modeling platform. These included speciation profiles, temporal profiles, and country, state, and county codes. Spatial surrogate data are discussed in the next section.

2.7 Tasks 7 and 8: Perform Simulations and Evaluation of the MAQSIP-VGR over the Houston-Galveston Domain and Northeast Gulf (southern Louisiana Gulf) Domain

We completed preparation of the meteorological inputs for the August 2000 episode (23 August through 2 September, 2000) over the regional modeling domain (the regular grid at 36-km horizontal resolution). As noted earlier, the regional modeling domain covered parts of the central and eastern U.S. and included the Houston-Galveston and the southern Louisiana Gulf domains. The variable-grid modeling domain applied a stretch factor from a 4-km-resolution domain over each of the two smaller domains to 36-km grid resolution at the boundaries of the regional modeling domain. Both the regular-grid and variable-grid modeling domains had the same horizontal coverage (Figure 36). They differed only on the horizontal grid resolution.

We used the variable-grid meteorology data (described earlier) as input into the SMOKE-VGR to prepare variable-grid emissions over the modeling domain, zooming into the Houston-Galveston domain and the southern Louisiana domains. We created scripts to process the nine different inventory sectors for the first five days of the episode on both the regular grid and the variable grid. After finishing the individual sectors, we created merged, 3-D output files that contain summed data for all sectors. These ten output files (five for the regular grid and five for the variable grid) each contained 25 time steps and the following modeling species (all units are moles/h except where indicated):

Higher aldehyde (ALD2), carbon monoxide (CO), ethene (ETH), formaldehyde (FORM), isoprene (ISOP), ammonia (NH₃), nitric oxide (NO), nitrogen dioxide (NO₂), NR, alkenes (OLE), alkanes (PAR), elemental carbon (PEC (g/h)), particulate matter coarse (PMC (g/h)),

particulate matter fine (PMFINE (g/h)), nitrate (PNO3 (g/h)), POA (g/h), sulfate (PSO4 (g/h)), sulfur dioxide (SO2), sulfuric acid (SULF), toluene (TOL), xylene (XYL)

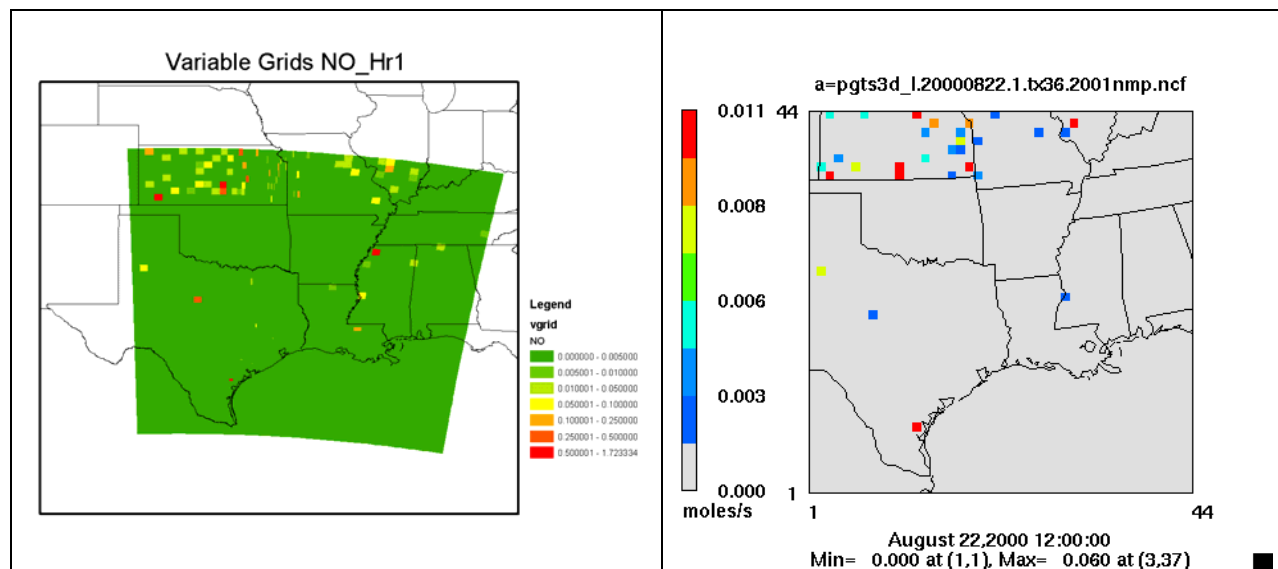
We performed quality assurance on the emissions data. Using SMOKE's reporting program, we created reports at various stages of the regular-grid processing. We used these reports to compare emissions totals in different combinations to ensure that the processed emissions matched the original totals in the inventory. To compare the variable-grid and regular-grid processing, we used reports generated by SMOKE's merging program. These reports contained emissions for each species broken out by state and county. We confirmed that the emissions totals for each sector and day were consistent between the regular grid and the variable grid.

Figures 39 and 40 show examples of the calculated SMOKE-VGR variable-grid emissions and SMOKE regular-grid emissions for one source category (IPM point sources). The inventory values for this category were based on the use of the Integrated Planning Model (IPM) to develop the state and unit-level emissions from the electricity-generating unit (EGU) sector.

Comparison between the SMOKE-VGR NO emissions (Figure 39a) and the SMOKE 36-km (regular grid) NO emissions (Figure 39b) shows good consistency between the locations of the sources on the regular grid versus variable grid. The inventory had 73 different EGU sources that matched IPM facilities in Kansas (mostly municipal plants), compared to Oklahoma, which had only 7, and Texas, which had only 51. Figure 39 also illustrates the benefits of the variable grid in its ability to more precisely locate the emissions.

Figures 40a and 40b are similar to Figure 39a but are for the emissions of CO and primary sulfate, respectively.

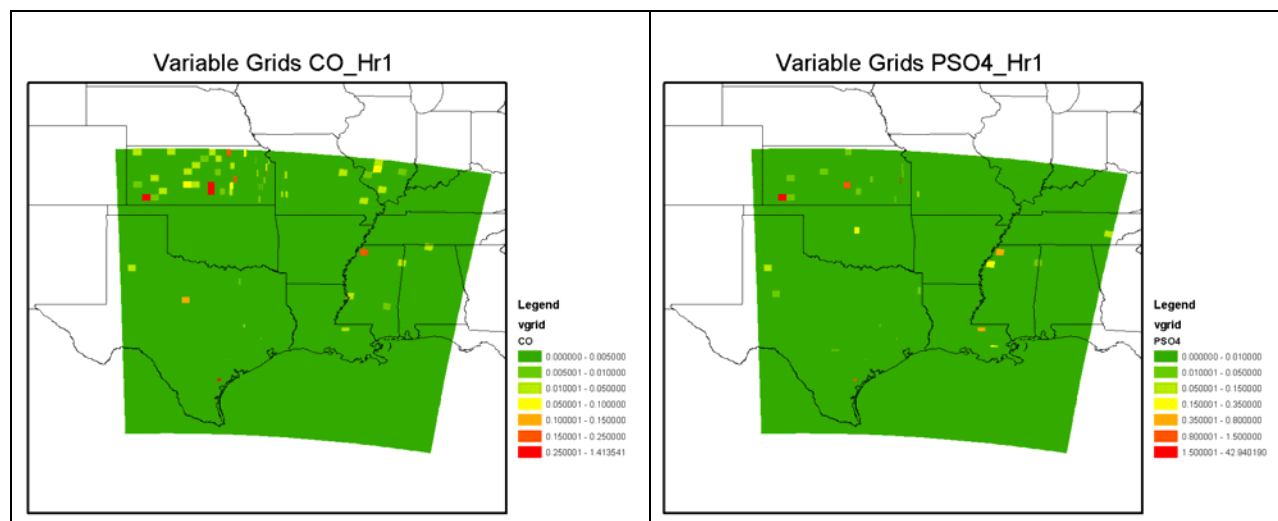
Figure 41 shows the CO emissions during 23 August 2000 over the variable-grid domain of the study and for a zoomed-in domain covering the Houston area. Figure 42 shows the PM-coarse emissions over the variable-grid domain for the same date. We used the variable-grid meteorology data as input into the SMOKE-VGR to prepare variable-grid emissions over the modeling domain zooming into the Houston-Galveston and southern Louisiana Gulf domains.



(a)

(b)

Figure 39. Emissions of point-source NO: (a) SMOKE-VGR one-hour variable-grid emissions; and (b) SMOKE 24-hour emissions (regular 36-km grid resolution)



(a)

(b)

Figure 40. SMOKE-VGR one-hour variable-grid point source emissions for (a) CO and (b) primary sulfate

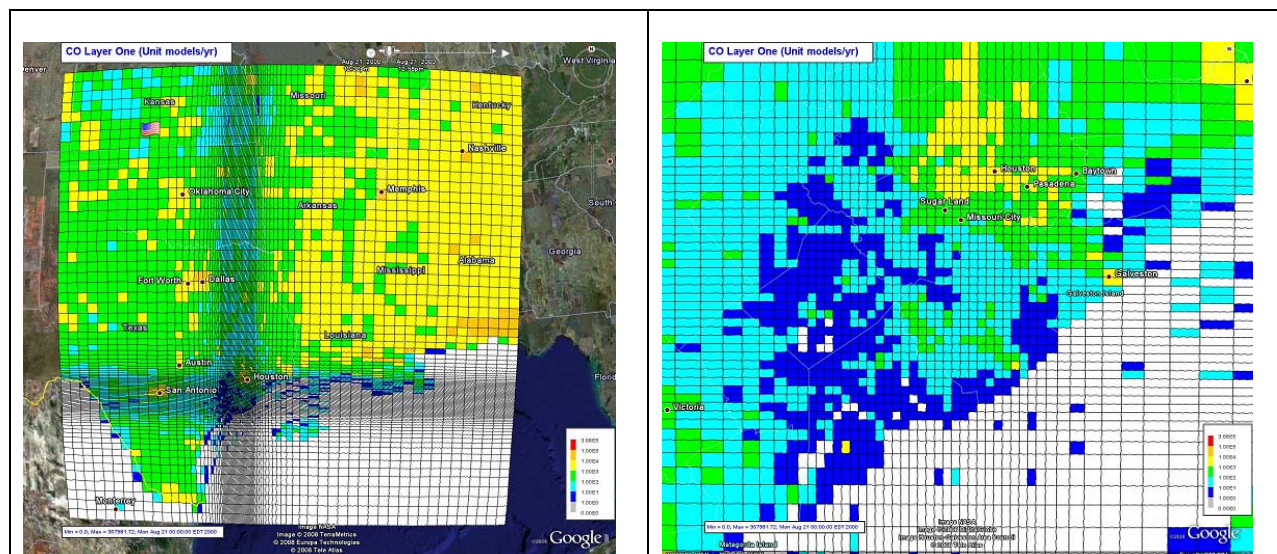


Figure 41. CO emissions (mol/yr) during 23 August 2000, for (a) the full domain and (b) the zoomed-in Houston area domain. Google Earth was used to create the variable-grid mesh on the domain.

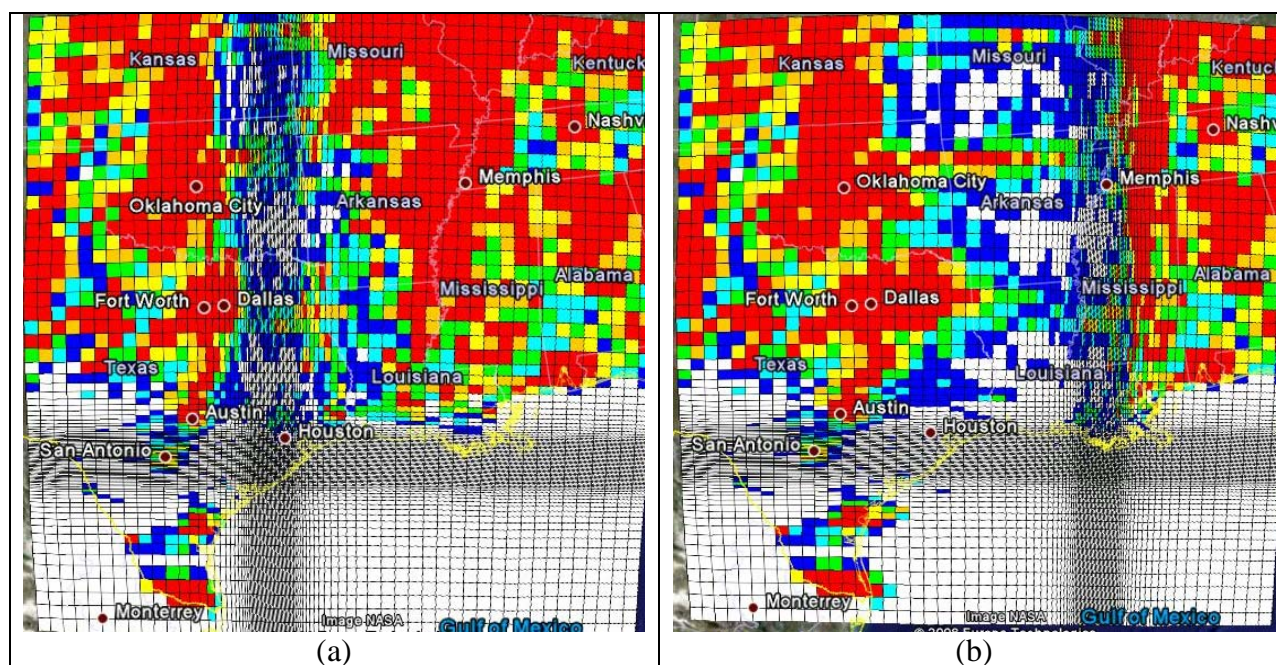


Figure 42. PM-coarse emissions during 23 August 2000, for full domain with (a) zoomed-in Houston-Galveston area domain and (b) zoomed in southern Louisiana domain.

Currently, we are running the MAQSIP-VGR for both the Houston-Galveston and the southern Louisiana case studies for ozone. Results are being compared to available measurements from the EPA Air Quality System (AQS) database (<http://www.epa.gov/air/data/index.html>).

2.8 Additional Tasks

The U.S. EPA has been following the progress of this project and has shown great interest in the approach and results. We have started to install and test the variable-grid technique in the latest version of the CMAQ modeling system, version 4.7, to create CMAQ-VGR. We are also making adjustments to the most recent version of the Meteorology-Chemistry Interface Processor (MCIP) that are needed to provide interpolated meteorology data to SMOKE-VGR and CMAQ-VGR from MM5 and from the Weather Research and Forecasting (WRF) model for use with the variable-grid technique. Similar to what we did with the MAQSIP-VGR, the CMAQ-VGR modeling system will be applied to the Houston-Galveston domain as a test-bed case study.

After completing these additional tasks, the CMAQ-VGR modeling system will be posted on the CMAS web site (www.cmascenter.org) for community download and use.

3. Conclusions

Emissions near coastal areas are subject to complex physical, dynamic, and chemical atmospheric processes that are influenced by characteristics of the earth's surface, and complexities exist in resolving the land-water interface. The resulting mesoscale circulation and the associated land-sea breeze affect the fate of emitted pollutants and their secondary chemical derivatives, such as ozone and fine particulate matter. Modeling the thermodynamics of the mesoscale circulation associated with the land-sea breeze must accurately account for the land-sea surface temperature gradient. In addition, capturing this mesoscale circulation and the associated air quality patterns and their profiles requires fine horizontal grid resolution near coastal areas that have high-emission sources.

3.1 Summary of Results

The research project presented here tackled the above problem on a number of fronts.

(A) Development of a variable-grid air quality modeling system

We developed a variable-grid-resolution (VGR) air quality model based on the Multiscale Air Quality Simulation Platform (Mathur et al., 2005), referred to as the MAQSIP-VGR, to simulate a high-pollution episode during August 2000 in the Houston-Galveston and southern Louisiana areas. The horizontal grid resolution in the VGR model varies from 36 km at the outermost edges of the modeling domain to 4 km at the innermost portions of the domain. The grid system is devoid of discrete boundaries across different resolutions; consequently, it alleviates many of the shortcomings in the commonly used nesting approach, in particular the propagation of numerical noise at the boundary of the nested domain.

(B) Enhancement of the physical and dynamical processes relevant to fine-scale modeling and land-sea circulation

The Mesoscale Model Version 5 (MM5), which is the meteorological driver of the MAQSIP-VGR, utilizes derived satellite sea surface temperatures (SSTs) and surface data assimilation to capture the mesoscale circulation associated the land-sea breeze. Our results show that using realistic SST patterns based on remote sensing is critical to correctly modeling the land-sea breeze, in particular the inland intrusion of the reversed mesoscale circulation, which is critical for the simulation of air pollution over urban areas near coastal regions (e.g., the Houston-Galveston and southern Louisiana). Besides capturing the correct horizontal gradient between land and sea surface temperatures, it is important to use an adequate boundary layer scheme in order to quantify correctly the vertical profiles of various parameters. The boundary layer scheme should capture the dynamics of the marine boundary layer, which is not often considered in a typical simulation over land. Our results show the effect of using the satellite-derived SSTs on the horizontal and vertical extent of the pollution pattern, and the increase in hourly ozone concentrations associated with changes in atmospheric boundary layer characteristics resulting from the enhanced mesoscale circulation in the lower troposphere

Further, it is important that the modeling system incorporate all types of clouds (shallow and deep convection).

(C) Use of emissions for modeling the offshore/onshore evolution and transport of pollutants near coastal areas

We presented and discussed results of a modeling study using a variable-grid air quality modeling system that retains the aspects of the mesoscale circulation in terms of surface temperature gradients and fine-grid resolution.

It was clear that using available emissions measurements and inventories near coastal areas is critical in order for the modeling system to capture the sources of pollutions near those areas and also benefit from the fine-scale horizontal resolution over urban areas close to the sources. We developed the SMOKE-VGR, based on the Sparse Matrix Operator Kernel Emissions (SMOKE) system, in order to take advantages of those sources at various horizontal resolutions.

3.2 Innovative Features of the Research Program

- A variable-grid modeling approach was developed. The grid size changes gradually from the large grid size (36 km, in this example) to 4 km or 1 km (as needed) in a single model run, eliminating the need for multiple model runs. This is a continuous model formulation; it does not need the boundary conditions that are required when using nested models.
- For simulating air quality, the variable-grid modeling approach is applied to both the air quality model and the emissions model.

- Once this new, advanced variable-grid approach has been used for operational air quality modeling, It has the potential to augment or replace the current regular-grid and nesting modeling approaches.
- For the first time, a variable-grid emissions model was developed (based on EPA's SMOKE system).
- Detailed emission estimates for offshore sources (including commercial marine vessels) using the most up-to date activity data were developed.
- The variable-grid approach is very effective near coastal regions where onshore and offshore emissions are manipulated by the land-sea breeze. Simulating this breeze requires fine grid resolution (4 km or less) so it can be captured correctly.

4. Publications

The following presentations and publications were completed during the course of this research project:

1. A review of the project's tasks and results was presented during
DOE/PERF Air Program Review, August 22-23, 2007, Annapolis, MD. Hosted by Argonne National Laboratory. For a copy of this presentation, please see our revised project progress report covering 4/17/06 through 10/16/07.
2. An abstract and a presentation at the American Meteorological Society annual meeting in January 2008:
"Application of a Variable-Grid Air Quality Model to Simulate On-shore/Off-shore Emissions near Coastal Areas" – Hanna, A.F., K. Alapaty, R. Mathur, S. Arunachalam, A. Xiu, and U. Shankar
3. Draft of a journal article to document the methodology and results in a scientific journal.
4. A project web site has been prepared to display the results of the project (at this time it is password protected). Web site URL:

http://www.ie.unc.edu/cempd/projects/variable_grid/index.cfm

References

- Alapaty, K., N. Seaman, D. Niyogi, and A. Hanna, 2001a: Assimilating Surface Data to Improve the Accuracy of Atmospheric Boundary Layer Simulations. *J. Appl. Meteor.*, 40, 2068-2082.
- Alapaty, K., N. Seaman, D.S. Niyogi, M. Alapaty, G. Hunter, and D. Stauffer, 2001b: Evaluation of surface data assimilation technique using the MM5. The 11th Penn State/NCAR MM5 Users' Workshop, 25-27 June 2001, Boulder, Colorado.
- Alapaty, K., D.S. Niyogi, and M. Alapaty, 2001c: Adjusting soil temperature and moisture using surface observations: Initial results from a single column model. Ninth Conference on Mesoscale Processes, 30 July-2 August, 2001, Ft. Lauderdale, Florida.
- Byun, D.W. and J.K.S. Ching, Eds., 1999: *Science algorithms of the EPA Models-3 Community Multi-scale Air Quality (CMAQ) Modeling System*. EPA/600/R-99/030, Office of Research and Development, U.S. Environmental Protection Agency.
- Chang, J.S., R.A. Brost, I.S.A. Isaksen, S. Madronich, P. Middleton, W.R. Stockwell, and C.J. Walcek, 1987: A three-dimensional Eulerian acid deposition model: Physical concepts and formulation.. *J. Geophys. Res.*, 92, 14,681-14,700.
- Chen, F., and J. Dudhia, 2001: Coupling an advanced land-surface/hydrology model with the Penn State/NCAR MM5 modeling system. Part I: Model implementation and Sensitivity. *Mon. Wea. Rev.*, 129, 569-585.
- Dennis, R.L., J.N. McHenry, W.R. Barchet, F.S. Binkowski, and D.W. Byun, 1993: Correcting RADM's sulfate underprediction: Discovery and correction of model errors and testing the corrections through comparisons against field data. *Atmos. Environ.* 27A(6), 975-997.
- Grell, G.A., J. Dudhia, and D.R. Stauffer, 1994: *A description of the fifth-generation Penn State/NCAR Mesoscale Model (MM5)*. NCAR Technical Note NCAR/TN-398+STR.
- Hanna, A.F, K. Alapaty, R. Mathur, S. Arunachalam, A Xiu, and U. Shankar, 2008: Application of a variable grid air quality model to simulate onshore/offshore emissions near coastal areas, 88th American Meteorological Society Annual Meeting held January 20-24, 2008, New Orleans, Louisiana, Conference on Atmospheric Chemistry.
- Mathur, R., U. Shankar, A.F. Hanna, et al., 2005: The Multi-scale Air Quality Simulation Platform (MAQSIP): Initial applications, and performance for tropospheric ozone and particulate matter, *J. Geophys. Res.*, 110:D13308, <http://dx.doi.org/10.1029/2004JD004918>.
- McHenry, J.N., J.S. Kain, and J.E. P1eim, 1996: Development and Testing of a Kain-Fritsch Based Deep Convective Cloud Chemistry Scheme for Incorporation into Multiscale Air Quality Models, *Proceedings, 9th Joint Conference On Air Pollution Meteorology*, American Meteorological Society.

- McHenry, J.N., and F.S. Binkowski, 1996: Development and Testing of a Betts-Miller Based Shallow Convective Cloud Chemistry Scheme for Incorporation into Multiscale Air Quality Models, *Proceedings, 9th Joint Conference On Air Pollution Meteorology*, American Meteorological Society.
- Nielsen-Gammon, J.W., 2002: *Evaluation and Comparison of Preliminary Meteorological Modeling for the August 2000 Houston-Galveston Ozone Episode*. Technical report available from the Technical Analysis Division, Texas Natural Resource Conservation Commission.
- Roselle, S.J., and F.S. Binkowski, 1999: Chapter 11: Clouds and chemistry. *Science Algorithms of the EPA Models-3 Community Multiscale Air Quality (CMAQ) Modeling System*. U.S. EPA Report EPA/600/R-99/030, 10 pp.
- Walcek, C.J., and G.R. Taylor, 1986: A theoretical model for computing vertical distributions of acidity and sulfate production within cumulus clouds, *J. Atmos. Sci.*, 43, 339-355.

National Energy Technology Laboratory

626 Cochrans Mill Road
P.O. Box 10940
Pittsburgh, PA 15236-0940

3610 Collins Ferry Road
P.O. Box 880
Morgantown, WV 26507-0880

One West Third Street, Suite 1400
Tulsa, OK 74103-3519

1450 Queen Avenue SW
Albany, OR 97321-2198

2175 University Ave. South
Suite 201
Fairbanks, AK 99709

Visit the NETL website at:
www.netl.doe.gov

Customer Service:
1-800-553-7681

